Sant'Anna
Scuola Universitaria Superiore Pisa

Universidad
Politécnica
de Cartagena

cnit

etsit
escuela técnica superior de
ingeniería de telecomunicación

CONSORZIO NACIONALE INTERUNIVERSITARIO PER LE TELECOMUNICAZIONI

LABORATORIO NAZIONALE DI RETI E TECNOLOGIE FOTONICHE

FINAL PROJECT:

MEASURING THE ROTATIONAL DOPPLER SHIFT TO CHARACTERIZE THE ORBITAL-ANGULAR-MOMENTUM ON SPINNING OBJECTS

Author:
Pablo Lucas Cánovas

Supervised by:
Antonella Boggoni - Head of research area of CNIT
Mirco Scaffardi - Researcher
Muhammad Nouman Malik - PhD student

Dedicated to all the people who help me
in my way, family, friends and tutors.
Thank you.

Contents

Resumen **12**

1 Summary **15**

2 Introduction of Optical communications **17**
2.1 History of Optical communications 17
2.2 The physics of optical fibers 18
2.3 Size and materials in optical fibers 21
2.4 Losses of an optical signal 22
2.5 Propagation modes 29
2.6 Free-space optical communication 31

3 The Orbital Angular Momentum **33**
3.1 Energy and momentum of light 33
3.2 Generation of OAM 36
3.2.1 Cylindrical lenses 36
3.2.2 Spiral Phase Plates 38
3.2.3 Q-Plates 39
3.2.4 Diffractive optical elements 40

4 Setup **42**
4.1 Explanation 42
4.2 Devices and instrumentation we used 43
4.3 Software used 57
4.4 Assembling and aligning the setup 58

5 Characterization **66**
5.1 How to observe the rotational Doppler shift 66
5.2 Characterization of the OAM with P80 E28 surface 74
5.2.1 Setup with beam expander 74
5.2.2 Setup without beam expander 87
5.3 Characterization of the OAM with P40 E28 surface 96
5.3.1 Setup with beam expander 96
5.3.2 Setup without beam expander 106

6 Comparative results **115**
6.1 OAM power differencies between surfaces 115
6.2 Frequency differencies between surfaces 119
6.3 SNR between surfaces 121

7 Conclusions and future lines **123**

Bibliography **125**

Matlab codes **127**

Python codes **136**

Appendix **148**

List of Figures

2.1 Fiber optic cable . . . 19
2.2 Total internal reflection . . . 19
2.3 Acceptance cone . . . 20
2.4 Transmission windows . . . 22
2.5 Spectral attenuation of a silica optical fiber . . . 24
2.6 Silica fiber attenuation curve for scattering Rayleigh and IR-UV absortion 26
2.7 Macro-curvature of a fiber optic cable . . . 28
2.8 Micro-curvature of a fiber optic cable . . . 28
2.9 Single-mode fiber . . . 29
2.10 Multimode fiber . . . 30
2.11 Step index fiber . . . 30
2.12 Graded index fiber . . . 31

3.1 Electromagnetic spectrum . . . 33
3.2 Circular polarization depends on $\pm\hbar$ per photon . . . 34
3.3 Angular momentum of a particle . . . 35
3.4 Beam with helically phasefront carries an orbital angular momentum $l\hbar$ per photon . . . 35
3.5 Cylindrical lens mode converters $\pi/2 - converter$ and $\pi - converter$ . . . 36
3.6 A HG mode at 45° can be decomposed in different HG modes, once rephased, the combination of these modes results in a LG_{02} mode . . . 37
3.7 The combination of a Hermite–Gaussian mode HG_{01} with another one rephased, HG_{10}, produce a Laguerre–Gaussian mode LG_{01} with helically phase 37
3.8 Spiral Phase Plate (SPP) . . . 38
3.9 Spiral Phase Plate to convert Gaussian beam to OAM beam . . . 38
3.10 Optical effect of a q-plate depending on the input beam polarization . . . 39
3.11 A helical phase profile generate a corkscrew wave front with an input Gaussian beam . . . 40
3.12 A forked diffraction pattern generated with the combination of the desired phase distribution ($\ell = 3$) plus a linear phase ramp . . . 41

4.1 Main scheme of the setup . . . 43
4.2 OSICS Mainframe - Modular 8-channel mainframe . . . 44
4.3 OSICS TLS-AG - WDM tunable lasers . . . 44
4.4 IPG Erbium Fiber Amplifier model EAD-500-C . . . 45
4.5 3-Paddle Polarization Controller . . . 46

4.6 Collimator model F810APC-1550 . . . 47
4.7 Polarizer LPMIR100-MP2 . . . 47
4.8 Spatial Light Modulator PLUTO-2 . . . 48
4.9 Iris SM1D12D . . . 49
4.10 Beam expander . . . 49
4.11 Power Supply PL154 . . . 50
4.12 Rotating plate . . . 50
4.13 Imperial professional surfaces . . . 51
4.14 Photodiode DET20C/M InGaAs Biased Detector . . . 51
4.15 Oscilloscope LeCroy WaveRunner 64 Xi . . . 52
4.16 Camera Xenics XS-4440 XEN-000122 . . . 53
4.17 Atenuation lens . . . 53
4.18 Fiber optics cables - FC Connector . . . 54
4.19 Surface of the connectors . . . 54
4.20 BNC connectors . . . 55
4.21 Power meter PM16-122 . . . 55
4.22 Detector Card VRC2 . . . 56
4.23 Setup picture 1 . . . 58
4.24 Setup picture 2 . . . 59
4.25 Setup picture 3 . . . 60
4.26 Setup picture 4 . . . 61
4.27 Setup picture 5 . . . 62
4.28 Setup picture 6 . . . 63
4.29 Setup picture 7 . . . 64
4.30 The complete setup . . . 65

5.1 Typical power spectrum of the intensity fluctuations . . . 67
5.2 Observed modulation frequency plotted as a function of rotation rate . . . 68
5.3 $l = 10$ fork phase pattern . . . 69
5.4 $l = 20$ fork phase pattern . . . 69
5.5 $l = 30$ fork phase pattern . . . 70
5.6 $l = 40$ fork phase pattern . . . 70
5.7 $l = 50$ fork phase pattern . . . 71
5.8 OAM of order $l = 10$ . . . 71
5.9 OAM of order $l = 20$ . . . 72
5.10 OAM of order $l = 30$ . . . 72
5.11 OAM of order $l = 40$ . . . 73
5.12 OAM of order $l = 50$ . . . 73
5.13 P80 E28 surface . . . 74
5.14 Setup with beam expanders . . . 75
5.15 Regulator for disc displacement . . . 76
5.16 OAM power for different displacements with beam expander (P80 E28 surface) . . . 79
5.17 Angular velocity in function of frequency modulation with beam expander (P80 E28 surface) . . . 82

5.18 Angular velocity in function of OAM power with beam expander (P80 E28 surface) . . . 82
5.19 Noise level spectrum . . . 85
5.20 Noise level spectrum + OAM power . . . 85
5.21 SNR with beam expander (P80 E28 surface) . . . 86
5.22 Setup without beam expanders . . . 87
5.23 OAM power for different displacements without beam expander (P80 E28 surface) . . . 90
5.24 Angular velocity in function of frequency modulation without beam expander (P80 E28 surface) . . . 93
5.25 Angular velocity in function of OAM power without beam expander (P80 E28 surface) . . . 93
5.26 SNR without beam expander (P80 E28 surface) . . . 95
5.27 P40 E28 surface . . . 96
5.28 Setup with beam expanders . . . 97
5.29 OAM power for different displacements with beam expander (P40 E28 surface) . . . 100
5.30 Angular velocity in function of frequency modulation with beam expander (P40 E28 surface) . . . 103
5.31 Angular velocity in function of OAM power with beam expander (P40 E28 surface) . . . 103
5.32 SNR with beam expander (P40 E28 surface) . . . 105
5.33 Setup without beam expanders . . . 106
5.34 OAM power for different displacements without beam expander (P40 E28 surface) . . . 109
5.35 Angular velocity in function of frequency modulation without beam expander (P40 E28 surface) . . . 112
5.36 Angular velocity in function of OAM power without beam expander (P40 E28 surface) . . . 112
5.37 SNR without beam expander (P40 E28 surface) . . . 114

6.1 OAM power in both surfaces with beam expanders . . . 116
6.2 Power difference between surfaces with beam expanders . . . 116
6.3 OAM power in both surfaces withou beam expanders . . . 117
6.4 Power difference between surfaces without beam expanders . . . 118
6.5 Modulation frequency in both surfaces with beam expanders . . . 119
6.6 Frequency difference between surfaces with beam expanders . . . 120
6.7 Modulation frequency in both surfaces without beam expanders . . . 120
6.8 Frequency difference between surfaces without beam expanders . . . 121
6.9 SNR in both surfaces with beam expanders . . . 121
6.10 SNR in both surfaces without beam expanders . . . 122

List of Tables

2.1 Wavelength bands in second and third transmission windows 22

5.1 Comparison between orders and radios for an OAM 74
5.2 Frequency modulation depending on OAM order 76
5.3 OAM peak power in function of the disc displacement with beam expander (P80 E28 surface) 78
5.4 Angular speed for different voltages 80
5.5 Theoretical frequency modulation and frequency modulation peak for different OAM orders and $V = 8.1\ V$ 81
5.6 Theoretical frequency modulation and frequency modulation peak for different OAM orders and $V = 9\ V$ 81
5.7 Theoretical frequency modulation and frequency modulation peak for different OAM orders and $V = 10\ V$ 81
5.8 Theoretical frequency modulation and frequency modulation peak for different OAM orders and $V = 11\ V$ 81
5.9 SNR for $l = 10$ with beam expander (P80 E28 surface) 83
5.10 SNR for $l = 20$ with beam expander (P80 E28 surface) 83
5.11 SNR for $l = 30$ with beam expander (P80 E28 surface) 84
5.12 SNR for $l = 40$ with beam expander (P80 E28 surface) 84
5.13 SNR for $l = 50$ with beam expander (P80 E28 surface) 84
5.14 Frequency modulation depending on OAM order 88
5.15 OAM peak power in function of the disc displacement $l = 10$ 88
5.16 OAM peak power in function of the disc displacement $l = 20$ 89
5.17 OAM peak power in function of the disc displacement $l = 30$ 89
5.18 Angular speed for different voltages 91
5.19 Theoretical frequency modulation and frequency modulation peak for different OAM orders and $V = 8.1\ V$ 92
5.20 Theoretical frequency modulation and frequency modulation peak for different OAM orders and $V = 9\ V$ 92
5.21 Theoretical frequency modulation and frequency modulation peak for different OAM orders and $V = 10\ V$ 92
5.22 Theoretical frequency modulation and frequency modulation peak for different OAM orders and $V = 11\ V$ 92
5.23 SNR for $l = 10$ without beam expander (P80 E28 surface) 94
5.24 SNR for $l = 20$ without beam expander (P80 E28 surface) 94
5.25 SNR for $l = 30$ without beam expander (P80 E28 surface) 94

5.26 SNR for $l = 40$ without beam expander (P80 E28 surface) 95
5.27 SNR for $l = 50$ without beam expander (P80 E28 surface) 95
5.28 Frequency modulation depending on OAM order 98
5.29 OAM peak power in function of the disc displacement with beam expander (P40 E28 surface) 99
5.30 Angular speed for different voltages 101
5.31 Theoretical frequency modulation and frequency modulation peak for different OAM orders and $V = 8.1\ V$ 102
5.32 Theoretical frequency modulation and frequency modulation peak for different OAM orders and $V = 9\ V$ 102
5.33 Theoretical frequency modulation and frequency modulation peak for different OAM orders and $V = 10\ V$ 102
5.34 Theoretical frequency modulation and frequency modulation peak for different OAM orders and $V = 11\ V$ 102
5.35 SNR for $l = 10$ without beam expander (P40 E28 surface) 104
5.36 SNR for $l = 20$ without beam expander (P40 E28 surface) 104
5.37 SNR for $l = 30$ without beam expander (P40 E28 surface) 104
5.38 SNR for $l = 40$ without beam expander (P40 E28 surface) 105
5.39 SNR for $l = 50$ without beam expander (P40 E28 surface) 105
5.40 Frequency modulation depending on OAM order 107
5.41 OAM peak power in function of the disc displacement $l = 10$ 107
5.42 OAM peak power in function of the disc displacement $l = 20$ 108
5.43 OAM peak power in function of the disc displacement $l = 30$ 108
5.44 Angular speed for different voltages 110
5.45 Theoretical frequency modulation and frequency modulation peak for different OAM orders and $V = 8.1\ V$ 111
5.46 Theoretical frequency modulation and frequency modulation peak for different OAM orders and $V = 9\ V$ 111
5.47 Theoretical frequency modulation and frequency modulation peak for different OAM orders and $V = 10\ V$ 111
5.48 Theoretical frequency modulation and frequency modulation peak for different OAM orders and $V = 11\ V$ 111
5.49 SNR for $l = 10$ without beam expander (P40 E28 surface) 113
5.50 SNR for $l = 20$ without beam expander (P40 E28 surface) 113
5.51 SNR for $l = 30$ without beam expander (P40 E28 surface) 113
5.52 SNR for $l = 40$ without beam expander (P40 E28 surface) 114
5.53 SNR for $l = 50$ without beam expander (P40 E28 surface) 114

6.1 $-3\ dB$ bandwidth 118

Resumen

El efecto Doppler es un fenómeno muy conocido y usado tanto en ciencia como en ingeniería para medir la velocidad y localización de un objeto en movimiento gracias al cambio que se produce en la frecuencia cuando existe un movimiento relativo entre un emisor y un receptor. Este fenómeno es usado desde para calcular la velocidad de galaxias lejanas, hasta para multar a un vehículo que supera una velocidad permitida.

El efecto Doppler clásico es sensible solo a la velocidad del objetivo a lo largo de la línea de visión entre el emisor y el receptor (velocidad longitudinal), ya que cualquier velocidad transversal no genera desplazamiento de frecuencia. No podemos medir la velocidad transversal con este modelo, debemos usar un método de trazado de rayos.

Una manera de medir esta velocidad transversal es usando haces de luz estructurados. La luz es una onda electromagnética que no solo lleva asociada una energía, sino también un momento, equivalente a un objeto que se encuentra en movimiento. Menos conocido es que la luz también porta consigo un momento angular, que es propio de los objetos con movimiento rotacional. Un haz de luz puede rotar sobre su propio eje de propagación

Para un haz de luz, existen dos tipos diferentes de rotación; la primera asociada a la rotación dinámica de los campos eléctrico y magnético sobre la dirección de propagación, la segunda va asociada a la rotación dinámica de los rayos de luz alrededor del principal eje del haz. Estas dos clases de rotación están asociadas a dos clases de momento angular, llamados SAM (Spin Angular Momentum) y OAM (Orbital Angular Momentum).

El SAM está asociado a la polarización, en particular a la polarización circular. El OAM está asociada con la distribución del campo espacial, y en particular con la forma helicoidal del frente de onda.

El momento angular orbital es una propiedad de luz que describe el patrón de fase helicoidal del frente de onda. Dicho con otras palabras, el grado de rizos del haz.

En este trabajo vamos a recopilar los pasos llevados a cabo para generar este OAM en un laboratorio, hablaremos sobre lo que es un OAM en profundidad, como generarlo, como interacciona con la materia, como medirlo... y llevaremos a cabo una serie de caracterizaciones en función de diferentes parámetros para intentar estudiar su comportamiento. Mostraremos los resultados obtenidos y discutiremos sobre posibles maneras de

mejorar la detección de este fenómeno, además de una comparación entre los resultados obtenidos. Hablaremos también sobre sus futuras implementaciones en diferentes ambitos y sobre todo en el gran potencial que tiene en el campo de las telecomunicaciones.

El objetivo principal de este trabajo ha sido la implementación y caracterización de un sistema LIDAR para el cálculo de la velocidad angular de objetos en rotación. Diferentes análisis de simulaciones han sido llevados a cabo para confirmar la validación de los resultados experimentales.

En este trabajo se ha relatado el estudio del momento angular orbital de la luz bajo ciertos parámetros modificables de un montaje de laboratorio. Durante el montaje pude presenciar las dificultades que conlleva realizar experimentos con laser en espacio libre. Existen muchas condiciones externas que pueden alterar las resultados como las vibraciones producidas por dispositivos externos, condiciones lumínicas del entorno, el margen de error existente a la hora de alinear la setup o la aleatoriedad con la que pueden impactar los haces reflejados a un fotoreceptor.

Las caracterizaciones realizadas se han centrado en como se comporta en términos de potencia y frecuencia este OAM cuando variábamos ciertos elementos del montaje de laboratorio como han sido la superficie con la cual el haz se reflejaba, es decir, un supuesto receptor en rotación. También variamos los órdenes del OAM de forma que cambiase el patrón de luz y el tamaño, así como la energía que lleva. Incluso se nos ocurrió hacer uso o no ciertos elementos de la setup como los beam expanders. El uso de elementos como el modular espacial de luz fueron cruciales para la realización del estudio ya que nos permitió superponer dos OAM distintos para obtener la modulación en frecuencia buscada.

Dado este enfoque, consideramos el principal objetivo de este trabajo establecer una base para un estudio más en profundidad del OAM donde se pudiera ahondar en las propiedades de este fenómeno, enfocado en este trabajo a la detección de objetivos en rotación. Varios desafíos técnicos fueron encontrados, algunos fueron resueltos, otros no. Sin embargo, se reflexionó sobre nuevos enfoques para el proyecto como son medidas de la vorticidad de flujo con haces de luz.

En general, termino este trabajo con satisfacción. Este proyecto puede considerarse un buen punto de partida sobre el análisis de ciertas características del OAM bajo unas condiciones determinadas y espero que pueda ser de utilidad para quien necesite saber un poco más o esté interesado en el estudio de la luz y sus aplicaciones.

En cuanto a líneas futuras, el experimento puede ser mejorado para obtener medidas con mayor precisión si se estudia el montaje realizado y se pone solución a algunos de los problemas descritos durante la realización de este trabajo. A falta de tiempo para realizar más experimentos, se propuso un enfoque para usar el OAM y realizar medidas

de vorticidad sobre fluidos. Según pudimos leer en muchas publicaciones científicas, los resultados obtenidos son muy interesantes a la hora de realizar mediciones sobre el OAM. Por otro lado, el hecho de poder detectar la velocidad angular de un objetivo con un sistema más eficiente abre muchas puertas al desarrollo de un sistema LIDAR que pudiera competir y ser más eficiente en determinadas circunstancias que con un sistema radar convencional.

Chapter 1

Summary

The Doppler effect is a well-known phenomenon and used both in science and engineering to measure the speed and location of an object in motion thanks to the change that occurs in the frequency when there is a relative movement between a transmitter and a receiver. This phenomenon is used to calculate the speed of distant galaxies, even to fine a vehicle that exceeds a permitted speed.

The classic Doppler effect is sensitive to the speed of the target along the line of sight between the emitter and the receiver (longitudinal speed), since any transverse speed does not generate frequency shift. We can not measure the transverse velocity with this model, we must use a ray tracing method.

One way to measure this transverse velocity is by using structured light beams [1]. Light is an electromagnetic wave that is not only associated with an energy, but also a moment, equivalent to an object that is in motion. Less known is that light also carries with it an angular momentum, which is typical of objects with rotational movement. A beam of light can rotate on its own axis of propagation.

For a beam of light, there are two different types of rotation; the first associated with the dynamic rotation of the electric and magnetic fields over the direction of propagation [2], the second one is associated with the dynamic rotation of the light rays around the main axis of the beam [1]. These two classes of rotation are associated with two kinds of angular momentum, called SAM (Spin Angular Momentum) and OAM (Orbital Angular Momentum) [3].

The SAM is associated with polarization, particularly circular polarization. The OAM is associated with the spatial field distribution, in particular with the helical shape of the wavefront. [4]. The OAM is a property of light that describes the helical phase pattern of the wavefront. In other words, the degree of curls that the beam has. [4]

In this work we will collect the steps taken to generate this OAM in a laboratory, we will talk about what is an OAM in depth, how to generate it, how it interacts with

the subject, how to measure it... We will carry out a series of characterizations based on of different parameters to try to study their behavior. We will show the results obtained and discuss possible ways to improve the detection of this phenomenon and we will perform a comparison of all the results. We will also talk about its future implementations in different areas and especially in the great potential it has in the field of telecommunications.

Chapter 2

Introduction of Optical communications

The purpose of this chapter is to narrate the history of optical communications from the first communications system created by the human being to the most modern free space propagation systems. It will be covered from the physics that occurs within an optical fiber, the reason of its geometry, the materials that compose it, the phenomena that help or difficult its propagation and in general the evolution that has suffered along the history.

2.1 History of Optical communications

The first optical communication systems date back to the year 1970, when the French inventor Claude Chappe invented the optical semaphore telegraph. Later, Alexander Graham Bell patented what would be the first wireless telephone, which he would call a photophone [5]. However, this project never materialized due to the previous appearance of the phone, much more practical. Some time later, in 1920, the English John Logie Baird and the American Clarence W. had the idea of using hollow tube matrices or transparent rods to transmit television and facsimile images.

In 1954, the British Harold H. Hopkins and the Dutchman Abraham Van Heel wrote papers on unclad fibers and clad fibers respectively. Van Heel made a great innovation, thanks to the coating with a transparent clad of a lower refractive index, he managed to protect the surface from external distortion and reduce interference between fibers [6]. By the end of the decade, fibers clad with glass or plastic achieved an attenuation of approximately 1 decibel (dB) per meter. In 1961, Elias Snitzer of American Optical published a theoretical model of a fiber with a core so small that it could carry light with only one waveguide mode. The model had medicinal acceptance to look inside patients, but the losses were still considerable, around 1 dB per meter. The device had no place at the moment in communications, where distances were much longer and required maximum losses around $10 \sim 20$ dB per kilometer.

Later, in 1964, Dr.Charles K. Kao illustrated the need to create a purer glass to

reduce light losses, which was standardized of $10 \sim 20$ dB per kilometer. In the summer of 1970, a group of researchers experimented with fused silica, a very pure material with a low refractive index. Corning Glass researchers, Robert Maurer, Donald Keck and Peter Schultz, invented the fiber optic cable or "optical waveguide fibers", capable of carrying much more information than copper cable. The light was sent with a pattern, which could be decoded thousands of kilometers away from the emitter [7]. The team developed a fiber with titanium core with which they could transport information with losses of 17 dB per kilometer, thus solving the problem of Dr.Kao.

During the following years (1972) multimode germanium-doped fibers were invented with losses of 4 dB per kilometer and with a greater resistance than in the case of the titanium-doped fiber. In 1973 a manufacturing process based on chemical vapor deposition was developed that made the definitive leap to the commercial manufacture of fiber optic cables.

During the year 1977, the first telephone call was made through a fiber optic system in Long Beach, California, by General Telephone and Electronics. That same year, Bell repeated the same feat with an optical telephone communications system in Chicago, covering a distance of 2.4 kilometers. [8]

We can conclude by saying that in the long term the development of this technology was a success, since fiber optic communications support the 80% of long distance data traffic worldwide.

2.2 The physics of optical fibers

An optical fiber is composed of a core and a cladding (see figure 2.1), both have different refractive indexes. We can assign n_1 as the refractive index of the core and n_2 as the refractive index of the cladding. When we speak of refractive index, we refer to the speed that light can reach when it propagates through a material, reaching in a vacuum the maximum speed of 299.792.458 m/s.

The refractive index can be calculated as:

$$Refractive\ index\ of\ the\ medium = \frac{Speed\ of\ light\ in\ a\ vacuum}{Speed\ of\ light\ in\ the\ medium}$$

In order for the light transmitted by the core of the fiber to be confined within, the refractive index of the core must be greater than that of the cladding.

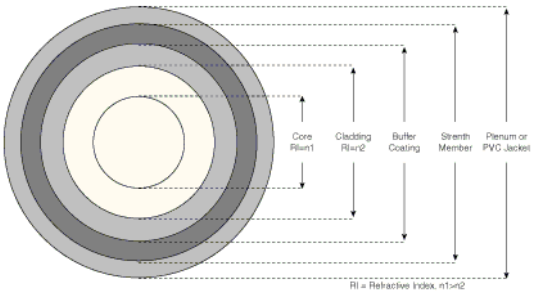

Figure 2.1: Fiber optic cable [5]

When we talk about transmission of light through optical fibers, this occurs thanks to the total internal reflection. When a beam of light injected by the end of a fiber strikes the core-to-cladding interface at an angle greater than the critical relative to the normal axis, the beam is reflected back to the core (see figure 2.2). The beam, once reflected, keep the same angle of reflection when it collides again, so it is redirected back to the core.

The other possible case is that the angle with which it impacts at the core-to-cladding interface is less than the critical angle, this will cause reflection and refraction phenomena, which results in a loss of energy in the form of attenuation of the light beam until it disappears completely after a certain distance.

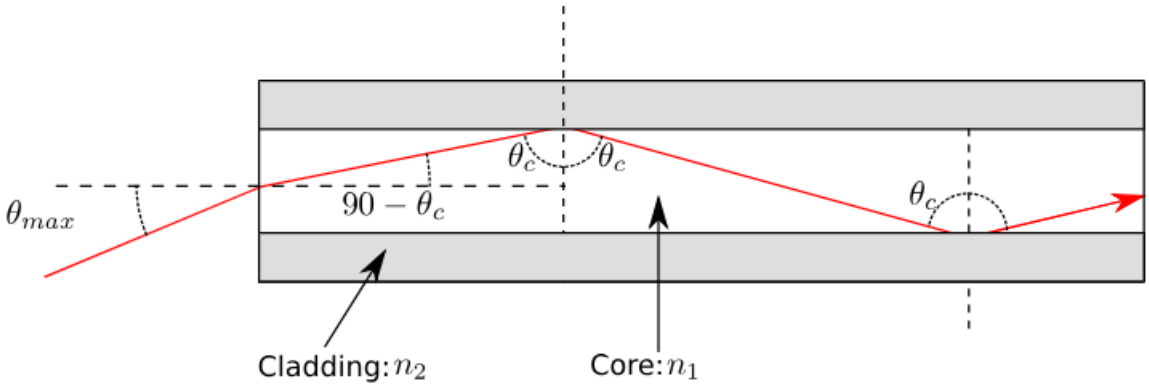

Figure 2.2: Total internal reflection

The formula that defines the critical angle is the following:

$$\theta_c = \arcsin \frac{n_1}{n_2}$$

It is important to know the angle of incidence of light in the fiber, this angle is known as the acceptance angle. If a beam hits with an angle greater than the acceptance angle, the angle of the transmitted beam will be less than the critical, which will cause a loss of energy due to reflections. We can define the maximum acceptance angle as:

$$\theta_{max} = \arcsin[\tfrac{n_1}{n_0} \sin \theta_c]$$

Where n_0 is the refractive index of the air.

The optical fiber also has a numerical aperture (NA), which is expressed by the following equation:

$$NA = \sqrt{n_1^2 - n_2^2}$$

The considerations we have had so far are for a two-dimensional plane of the fiber, but a fiber is a cylinder so we will have to carry out a three-dimensional study to clarify some of the aspects discussed above. If we rotate the acceptance angle on the fiber axis we will obtain the acceptance cone (see figure 2.3). The size of the cone depends on the difference in the refractive index between the core and the coating. As we have said before, any beam that falls with a greater angle inside the acceptance cone will be attenuated in each reflection until it disappears.

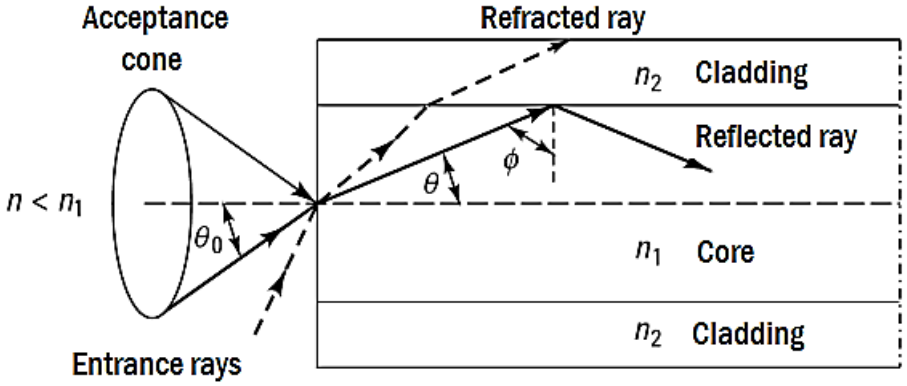

Figure 2.3: Acceptance cone

On the other hand, the efficiency of the cable gives us information about the amount of light that we can attach to the core through the acceptance cone. We must be careful with the amount of light that we connect, because the greater the amount of light, the higher the bit error rate (BER), since more light reaches the receiver. The attenuation depends on the efficiency of the cable, being inversely proportional to each other. Another aspect to consider is the chromatic dispersion, the less it occurs, the higher the rate of speed with which the data is transmitted.

The unit of measurement for the power in optical communications is the Watio, but because the scales in which we work are very small it is not comfortable to work with a linear scale so the measurements are expressed in logarithmic scale as decibels (dB). The conversion is made with respect to 1 mW so that 1 mW corresponds to 0 dBm.

$$Power(dBm) = 10 \log_{10}(\tfrac{Power(mW)}{1mW})$$

2.3 Size and materials in optical fibers

Normally the measurements of an optical fiber cable are given as the diameter of the core followed by the diameter of the cladding. These parameters change with the type of cable and its use, the ranges for the diameter of the core are between 8 μm to 100 μm. On the other hand, the ranges for the cladding diameter are between 250 μm and 900 μm. [9]

The larger the diameter of the core, the more light capacity will be able to transport the fiber, but this can lead to a problem of saturation in the receiver. The most common materials used for the manufacture of fiber optic cables are:

- **Glass**: This type of material offers the least attenuation. Both the core and the coating are made of glass. When we speak of glass, we refer to a pure and ultra transparent glass in which impurities have been added during the manufacturing process to obtain the appropriate refractive index to allow light to travel through it. Another type of residual impurities can remain in the cable during the manufacturing process, worsening the final result in terms of attenuation parameters.

- **Plastic**: This material presents the worst attenuation characteristics. Both the core and the coating are made of plastic, making it larger in size. The core is made of polymethyl methacrylate (PMMA) coated with a fluropolymer. This type of cables work well when the distances to be saved are not very large, since the attenuation would not affect so much. Another drawback is that, because it is made of plastic, it can not be exposed to climatic conditions where temperatures are high. On the other hand, the plastic offers great resistance to the radius of curvature and external hits.

- **Plastic-clad silica (PCS)**: This type of cable is located halfway between plastic and glass. It contains a glass core and a plastic coating with a lower refractive index. This type of cable is not widely used due to several defects derived from the plastic coating. However, improvements have been made over the years.

What differentiates one type from another is the attenuation that it generates. The attenuation is mainly caused by two phenomena: absorption and scattering. The absorption is produced by the interaction of light particles (photons) with the particles that make up the core of the fiber. The scattering is due to the rays that pass from being propagated by the core to the coating. There are transmission windows for the different wavelengths to which light propagates so that the effects of attenuation are minimized (see figure 2.4).

The first transmission window is located at 850 nm, the second window at 1310 nm and the last one at 1550 nm. The first transmission window is no longer used as it was the first to be used when this technology was first used and offers worse performance than

the other two [10]. The attenuation suffered in the first window is 2 dB/km while in the others it is 0.5 dB/km and 0.12 dB/km respectively.

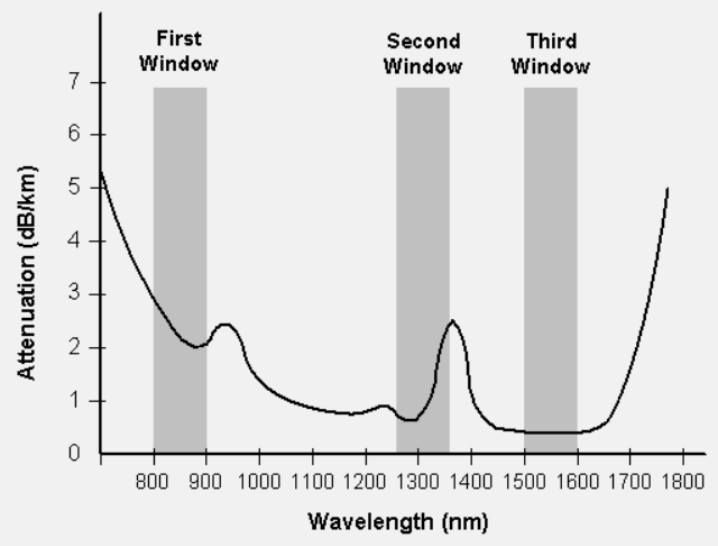

Figure 2.4: Transmission windows

The second and third transmission windows are subdivided into the following wavelength bands:

Band	Description	Wavelength range
O band	original	1260–1360 nm
E band	extended	1360–1460 nm
S band	short wavelengths	1460–1530 nm
C band	conventional ("erbium window")	1530–1565 nm
L band	long wavelengths	1565–1625 nm
U band	ultralong wavelengths	1625–1675 nm

Table 2.1: Wavelength bands in second and third transmission windows [10]

The third transmission window is the one with the least attenuation, but it is not the most used one. Other factors that negatively influence the transmission of information such as dispersion must be taken into account.

2.4 Losses of an optical signal

When an electromagnetic wave propagates through a material, this wave is subject to the physical properties of that material. The atomic composition and the arrangement of atoms in the material gives rise to different phenomena that determine the values that

take some of their physical parameters. The main mechanisms associated with losses through an optical fiber are those derived from absorption, dispersion and radiation that escapes to the outside. The absorption comes from the material with which the fiber is made, while the other two derive both from the material and from the imperfections that may exist after the manufacture of the fiber.

The losses, of whatever type, are expressed in decibels. To do this given a certain structure, we must measure the optical power at the entrance of the fiber, P_{in}, and on the output, P_{out}, after a certain distance L. The expression of the attenuation remains as:

$$\alpha_{dB} = 10 \log_{10} \frac{P_{in}}{P_{out}}$$

- **Absorption**: As we said before, the absorption is mainly caused by the material and the impurities that the fiber has. More specifically, by the atomic and molecular structure of the components.

  Atoms can absorb electromagnetic radiation when an electron jumps from a certain electronic level to an upper one that is empty. These jumps give rise to an absorption of energy, which involves losses. Most of these jumps occur in the range of frequencies between ultraviolet and visible light and can be described fairly accurately by the empirical equation of Urbach

  $$\alpha_{dB} = Ce^{E/E_0}(dB/km)$$

  where C and E_0 are empirical constants and E is the energy of the photon.

  If we move in the spectrum towards the infrared region, there appears an absorption derived from the possible vibrations of the bonds between the atoms that constitute the material, in this case the molecules of S_iO_2. The interaction between the links and an electromagnetic field at a given frequency results in an absorption and therefore losses [11]. For this case we also have an equation that approximates these losses, for the case of $GeO_2 - SiO_2$

  $$\alpha_{IR} = 7,81 \cdot 10^{11} e^{(-\frac{48,48}{\lambda})}(dB/km)$$

  These two classes of absorptions are those that will occur in any type of fiber regardless of the material used, they are called **intrinsic absorption losses**. Depending on the precision of the manufacturing process, more or less impurities will appear in the fiber, and therefore, higher or lower absorptions. The objective of further improving optical communication technologies was to achieve losses that were below the existing transmission media. The improvement in the production systems

caused that many of the absorption peaks in the fibers of the first years were eliminated, improving the parameters of the attenuation curves as a function of λ in the optical fibers.

On the other hand, the ions of some of the transition materials such as iron, chromium, cobalt, copper, as well as OH ions form the main impurities that are causing the **extrinsic losses by absorption**. When these transition metals are present in proportions of 0,001 to 0,01 parts per million (ppm), they give rise to losses between $1 \sim 10\ dB/km$. As for the OH ions, the situation gets worse when we have concentrations equivalent to 0,003 ppm giving losses of the order of 20 dB/km. The main peak of absorption by OH ions is found for a wavelength of $2,7\ \mu m$, the harmonics of this tone are found at 725 nm, 950 nm and 1400 nm. At these points the main absorptions take place and the zones located between these points (see figure 2.5) were those designated to be the first, second and third transmission windows.

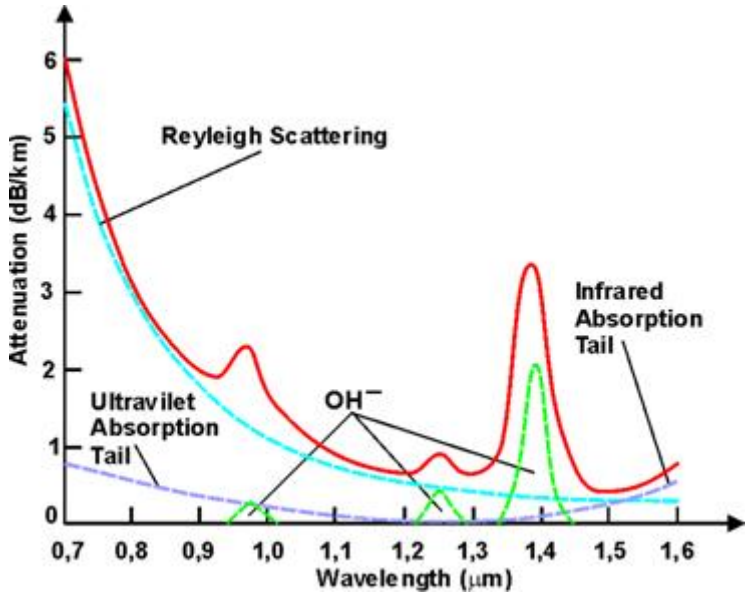

Figure 2.5: Spectral attenuation of a silica optical fiber

Thanks to the current manufacturing processes, the level of OH ions has been reduced, reaching less than 0,001 ppm. We have spoken that the main material that the fibers constitute is SiO_2, but there are not many occasions in which only this material is used. It is normally doped with other elements to obtain the desired refractive index and, therefore, modify the behavior of the fiber. Among those found are the GeO_2, the P_2O_5 and the B_2O_3. [11]

- **Dispersion**: The material of the fiber is not the only thing that leads to losses. Impurities of a microscopic nature influence the losses that can exist through the

fiber, these small particles can scatter the light causing them to be reflected in a different direction than the incidence. These losses vary with the wavelength and the size of the irregularity.

- **Intermodal dispersion**: It is produced in multimode fibers. Some rays reach the end of the guide before others, that is, they travel different distances reaching the end at different times. This causes that the reconstruction of the beam transmitted in reception does not occur in a single moment, giving rise to a broadening of the pulse.

- **Intramodal or chromatic dispersion**: It is produced in single-mode fibers, although the pulse emitted by the laser is sinusoidal, its behavior in frequency is not a perfect delta, but it has a certain spectral width. It will be formed by different frequency components that propagate at different speeds resulting in a widening of the pulse. This effect is accentuated if the signal transmitted by the laser is modulated. In multimode fibers this phenomenon also occurs but is negligible.

- **Scattering Rayleigh**: This type of dispersion occurs when non-uniformities of the material, such as density, dielectric constant or refractive index, have dimensions less than $0,1\mu m$. These variations with respect to the uniformity can be grouped in two terms: those that depend on the fluctuation of the density of the material and those that depend on the composition. Both appear due to the manufacturing processes and are difficult to eliminate in their entirety. For the case of fluctuations in density we have an expression to approximate the losses

  $$\alpha_R = \frac{8\pi^3}{3\lambda^4}(n^2-1)^2 K T_f \beta_T \text{ dB/km}$$

  where K is the Boltzmann constant, T_f is a fictitious temperature, β_T is the isothermal compressibility of the material and n is the refractive index of the material. In the previous equation there is an attenuation dependency with l/λ^4, therefore, the longer the wavelength, the less influence these losses will have. With this new contribution and the previous ones in the ultraviolet and infrared range we can define an attenuation curve.

  This type of dispersion causes the radiation to leave towards all the directions of the space, we could say almost omnidirectional. This can be used for fiber characterization measurements, but it can be problematic when it is transmitted bi-directionally.

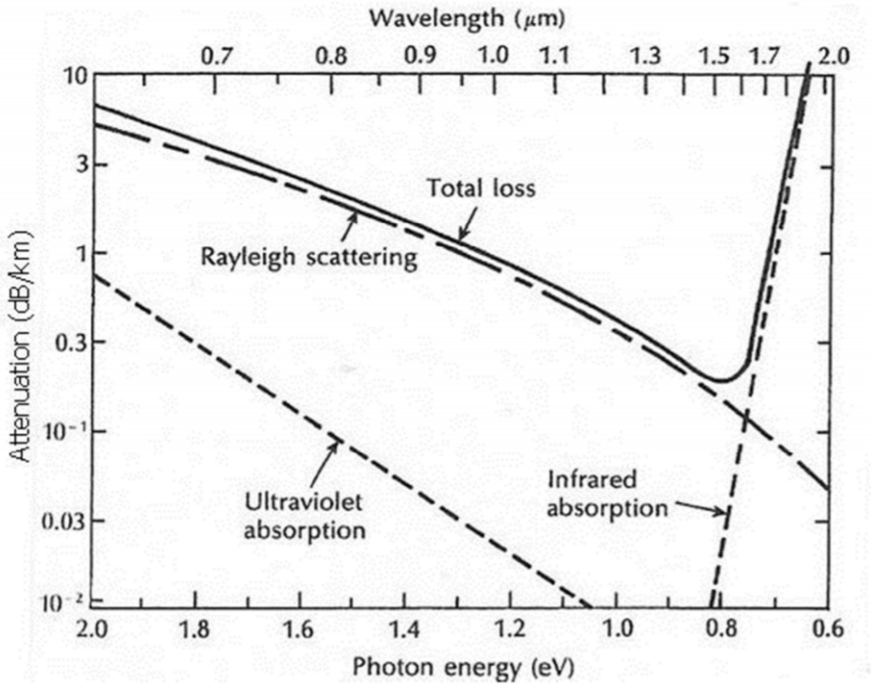

Figure 2.6: Silica fiber attenuation curve for scattering Rayleigh and IR-UV absortion

- **Scattering Mie**: This type of dispersion occurs in inhomogeneities that are of a magnitude equivalent to or greater than the wavelength that is propagating. It can come from small alterations in the fiber, from the geometry or from the difference of refractive indexes of the core and the cover. Other imperfections that cause this phenomenon are small bubbles or mechanical stresses in the material. The good news is that all these sources of losses can be eliminated with a careful manufacturing process.

- **Other types of dispersion**: The two types of dispersion that we have explained previously can be included within *linear dispersions*. This is because the magnitude with which they affect the losses within the fiber do not depend on the intensity level of the incident light. Therefore, there is another type of *non linear dispersions* where the intensity of the incident radiation does influence how losses affect it. The two most important phenomena are the **dispersion of Brillouin** and the **dispersion of Raman**. When the power transmitted by the fibers is not very high, these dispersion phenomena are not very significant in the most basic communications. On the other hand, in those communications where a very high number of channels are transmitted and the power is high this type of phenomena can significantly alter the transmission.

  * **Stimulated Brillouin Scattering**: This type of dispersion is due to the acoustic properties of the interaction of the photon with the medium [12]. When photons propagate through the fiber they interact with the silica molecules of the material and also between photons. From these shocks,

dispersion effects are generated in the reverse direction to the propagation direction. Brillouin scattering generates a wave called the Stokes wave due to energy dispersion. This wave amplifies the higher wavelengths, this gain is the basis of the so-called Brillouin amplification.

* **Stimulated Raman Scattering**: The photons, as they pass through the fiber, interact with the silica molecules and with other photons causing the dispersion effect called Raman scattering. This dispersion of the radiation occurs in both directions in the fiber, which translates into a dispersion of the energy towards a random direction.

  This type of dispersion means that the lower wavelengths increase the amplitude of the higher wavelengths, causing the high ones to suppress the low ones. By decreasing the power at the entrance we can reduce the effects. Despite this, the Raman scatter generates a wave called the Stokes wave due to the scattering of energy. This wave amplifies the higher wavelengths, this gain is the basis of the so-called Raman amplification.

- **Losses due to curvatures**: As you can guess, it has been assumed in all the previous cases that the geometry along the fiber had a linear distribution, but reality is far from all this. When a fiber installation is made, the operators have to deal with all kinds of obstacles that must be overcome to get the fiber from a transmitter to a receiver. This implies that there are sections in which the fiber will necessarily undergo a curvature, with greater or lesser radius, which will alter the properties of the signal that is transmitted by it. This type of curvature is called **macro-curvatures** (see figure 2.7) and gives rise to certain losses.

  Those whose radius is greater than the dimensions of the fiber core are considered macro-curves. We also have the following problem, suppose that only the fundamental mode is propagating along the fiber core. Due to a curvature of this type part of the beam will begin to propagate through the cover as it will strike at an angle greater than the critical at the core-to-cladding interface. Due to the curvature, the distance traveled by a beam through the upper cladding will be greater than that traveled by a beam that moves through the core. In the same way, the distance a beam travels through the lower cover will be less than the core. This means that, for the energy pattern to remain in reception, the beam on the upper deck would have to travel at a faster rate than the light itself and vice versa on the lower deck, this being clearly impossible. As a consequence, the radiation that is transmitted by the fiber loses some of its intensity.

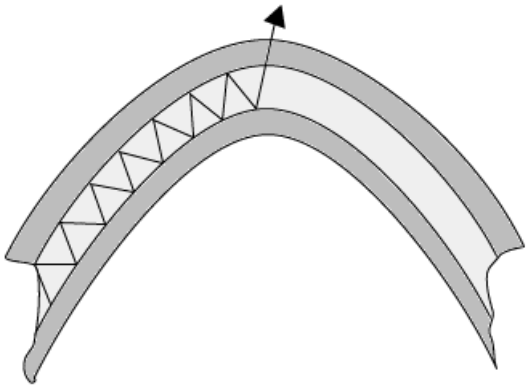

Figure 2.7: Macro-curvature of a fiber optic cable

The losses that occur due to this type of curvature depend very closely on the radius of curvature of the fiber and the number of modes that are propagating. The greater the way it spreads, the less confined it will be in the core and the more tendency it will have to lose energy to the outside.

On the other hand, we have another type of curvatures generated during the manufacturing process of the fiber. Glass fibers are not installed as such once they are manufactured, they are arranged together and reinforced with covers of other materials to give strength to the whole. During this process in which stretches of fiber are joined it is impossible to achieve a completely linear union between both, which results in certain curvatures called **micro-curvatures** (see figure 2.8), and that they carry associated losses called micro-curvature losses.

These tiny curvatures are periodic small-scale fluctuations in the walls of the fiber. This causes the rays, when bouncing on these deformations, to change their angle of incidence making it greater or lesser than the critical one. This gives rise to situations where we will lose energy when part of the beam happens to spread through the cladding or other situations in which the beams will be redirected and become lower modes than they were originally. The most effective way to minimize these losses is to cover the optical fiber with a suitable coating in a way that protects the fiber and is able to absorb the possible deformations that occur in the cables.

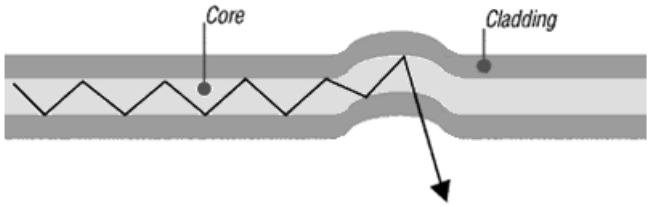

Figure 2.8: Micro-curvature of a fiber optic cable

2.5 Propagation modes

It is well known that optical fibers have two modes of propagation: single mode and multimode. Both have their own characteristics in terms of the amount of information they can carry and how they are affected by the phenomena of attenuation and temporal dispersion. As a general rule, single mode fiber optic cables have better characteristics than multimode cables. Different beams with variations in light intensity propagate through an optical fiber, this occurs along the length of the cable. This variation of the intensity allows us to classify the light rays into propagation modes, and can be ordered from a lower to a higher order. The number of modes that propagate depends on the size of the cable and the refractive indexes of the core and the coating. Apart from single-mode and multimode fibers, there are step index fiber and fibers of graded index fibers.

- **Single mode fiber**: In this type of fibers the diameter of the core is very thin compared to the cladding. Therefore, when we introduce a beam of light at the beginning of the fiber, only one ray (a single mode) corresponding to the lowest order or so-called fundamental mode will propagate (see figure 2.9). In order for only the fundamental mode to propagate, the wavelength must be above a certain specific wavelength called the cut-off wavelength. Because of this, there is hardly any loss of energy since there are no higher order modes propagating. The attenuation is very low and the beam is only affected by the chromatic dispersion. The minimum chromatic dispersion is in the second transmission window, this is the reason why the most used window is not the one that produces less attenuation.

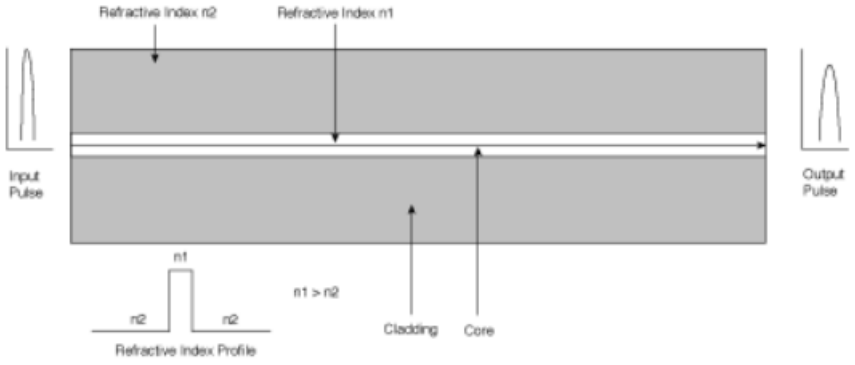

Figure 2.9: Single-mode fiber [5]

- **Multimode fiber**: In this type of fibers the diameter of the core is large compared to the coating. Therefore, when we introduce a beam of light at the end of the fiber, several rays (some modes) will propagate (see figure 2.10). In this case the fundamental mode continues to propagate through the center of the fiber, but is accompanied by higher order modes that propagate bouncing inside the core with the coating. Temporal dispersion and attenuation are more notable in this type of fibers, the rebound of the beams in the core-to-cladding interface favors the loss of

energy and that the beams travel the distance of the fiber in different ways reaching the receiver at different times. This causes the pulse at the exit of the fiber to be attenuated and widened. Although this type of fiber offers worse performance than single-mode fiber, it is widely used in facilities due to its lower cost and acceptable results in sections of several kilometers away.

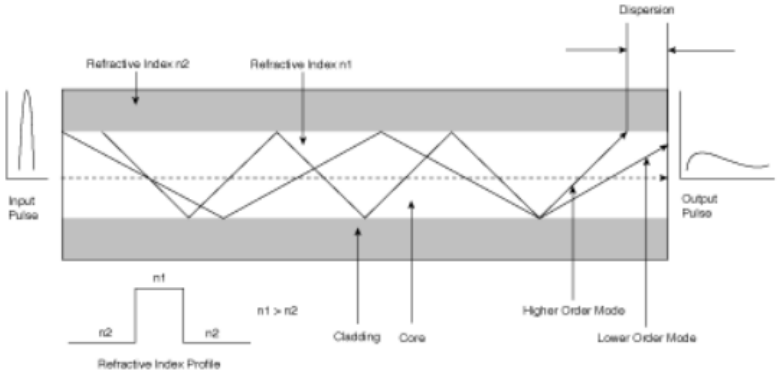

Figure 2.10: Multimode fiber [5]

- **Step index fiber**: This type of fibers have a double cladding (see figure 2.11), this makes it has a great resistance to macrocurvatures. It also has two points of zero dispersion and a low dispersion in a wide range of wavelengths. Each cladding has a higher refractive index than the core, the inner has lower refractive index than the outher cladding.

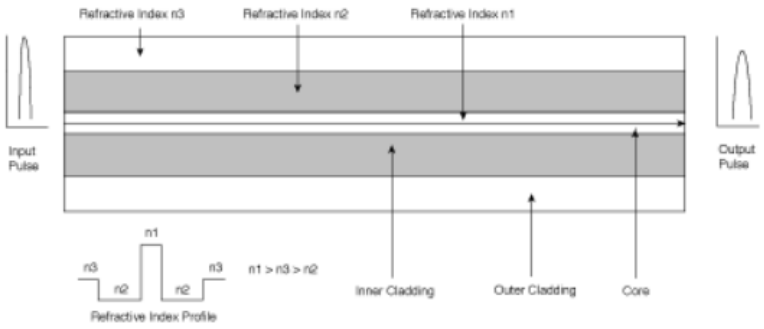

Figure 2.11: Step index fiber [5]

- **Graded index fiber**: This type of fibers has a higher refractive index in the core and decreases progressively as we approach the cladding, hence its name, since there is no sharp jump between refractive indexes. We can consider the core and coating as one piece. In this way, the fundamental mode is slowed down, since the refractive

index in the center of the core is maximum, and higher order modes can arrive with less delay than those of lower order (see figure 2.12), thus avoiding intermodal dispersion. Because of this, higher-order modes that do not propagate through the center of the core trace a kind of ellipse.

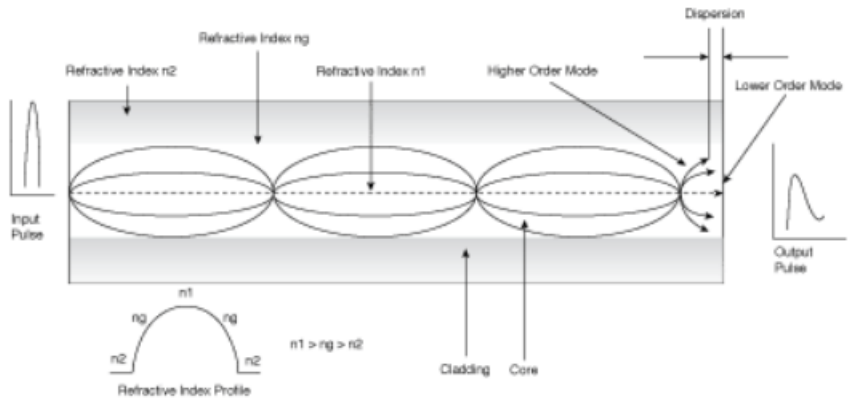

Figure 2.12: Graded index fiber [5]

2.6 Free-space optical communication

It is convenient to finish the introduction to optical communications with this section where we will deal with the most relevant aspects of free space communications since the project carried out in the laboratory only uses a small fiber optic section to conduct the light from the laser source and going through an optical amplifier until the setup of the experiment, where the beam will enter free space and it will be much more difficult to control its handling through lenses and elements where it will be reflected.

When we refer to optical communications in free space we speak of a line-of-sight (LOS) technology that transmits a beam of modulated light, either visible light or outside this area of the spectrum, for communications through the atmosphere. As in conventional optical communications, the source that generates this beam can come from an LED or a laser source. The main difference between fiber communications with respect to free space communications is the absence of a guided medium such as optical cable. As expected, a high-sensitivity optical receiver that receives the signal is necessary. [13]

This type of links has certain advantages, we could think that by spreading a signal through the air we are being interfered with (or interfering) by other radio signals around us, but it is not, the links have immunity to this type of interference. Being a link that propagates in a space direction makes it difficult to intercept, which means an increase in terms of security for the information transmitted through it. On the other hand, when we

talk about speeds, these are very similar to those achieved in optical fibers. This supposes a reduction of the cost due to the infrastructure that is not necessary.

On the other hand, it also has drawbacks that make it a less attractive option due to the atmospheric conditions that the location where we want to build the link can present. Some of the meteorological phenomena that can most affect this type of communication are:

- Fog
- Beam dispersion
- Atmospheric absorption
- Beam dispersion
- Rain
- Snow
- Interference from background light sources (including the sun)
- Pollution

All these factors affect the signals that arrive at reception by attenuating them and increasing the bit error rate (BER). Some of these phenomena are exponentially like atmospheric attenuation or fog, causing the total range of the link to decrease to only several kilometers

Chapter 3

The Orbital Angular Momentum

In this chapter we will explain the phenomenon that causes light to behave with a helical wavefront known as the Orbital Angular Moment. The objective is not to extend in mathematical terms but to know the phenomenon and the way to implement it in a laser beam. We will see that there are many different methods to generate this spatial structure beam and that it has surprising properties.

3.1 Energy and momentum of light

Light is part of the electromagnetic radiation that can be observed by the human eye, also called visible light. Its wavelength is located between 380 nm, limiting the part of the spectrum corresponding to the ultraviolet and 780 nm, which limits the infrared. In physics, light makes not only reference to the visible part of the spectrum, but to the set of electromagnetic radiations (see figure 3.1) that form it including gamma rays, X-rays, ultraviolet light, infrared light, microwaves and radio waves.

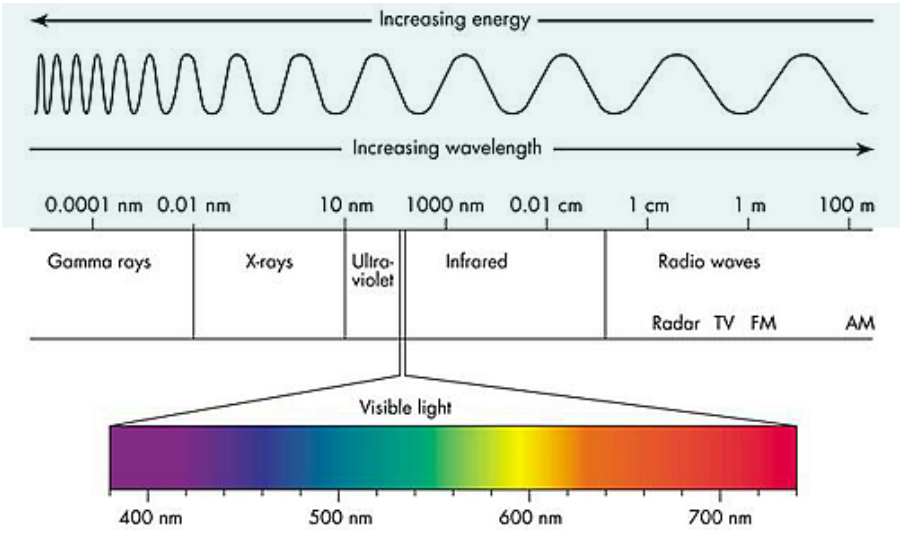

Figure 3.1: Electromagnetic spectrum

The particle responsible for all electromagnetic phenomena is the photon. Photons have a wave-corpuscle duality by which they can exhibit typical wave or particle behavior depending on the circumstances in which they are measured. The photons have electric charge and zero mass, in addition to a constant speed c. By possessing null mass and constant velocity its energy can be defined with its frequency and the Planck constant:

$$E = h \cdot \nu$$

Where E is the energy, h is the Planck constant and ν is the wave frequency of the light.

If the light contains a particle, it must have associated a moment like any other particle, and it is. In addition to energy, photons are associated with a linear moment and a polarization. The light contains a linear moment equivalent to $p = \hbar k$ per photon. [4]. Where p is the linear moment, $\hbar = \frac{h}{2\pi}$ constitutes the reduced Planck constant and $k = \frac{2\pi}{\lambda}$ is the wave vector.

Therefore, light also carries an angular momentum that can be divided into two types; a spin part (SAM) and an orbital part (OAM). The first referred to polarization (circular) whose value for a photon can be $\pm\hbar$, which refers to the angular momentum of rotation (spin) of each of the photons of the light beam [14]. The sign $\oplus$ indicates left-handed polarization, while the sign $\ominus$ indicates right-handed polarization (see figure 3.2). The second one is associated to the spatial field distribution whose value for a photon is known as $l\hbar$ where l is an integer value that can be positive or negative.

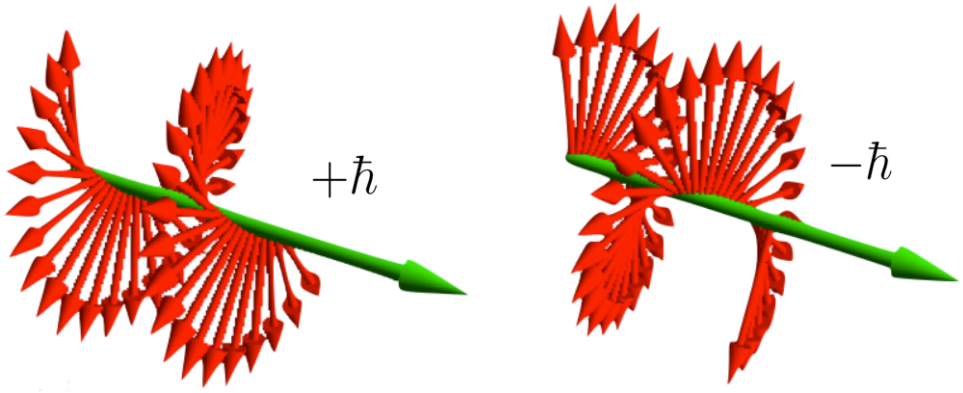

Figure 3.2: Circular polarization depends on $\pm\hbar$ per photon

The relationship between linear and angular momentum is given by $\mathbf{L} = \mathbf{r} \times \mathbf{p}$ (see figure 3.3), where $\mathbf{L}$ is the angular momentum of a particle with respect to the point, $\mathbf{r}$ is the position of the particle with respect to the origin and $\mathbf{p}$ is the linear moment that equals to $\mathbf{p} = m\mathbf{v}$ [4].

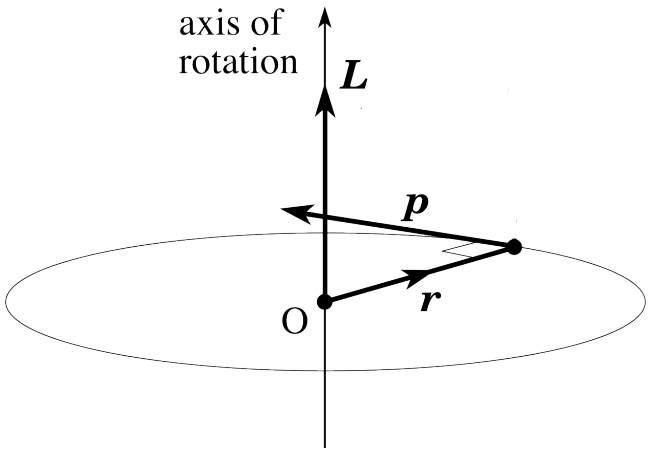

Figure 3.3: Angular momentum of a particle

Beams of light that carry a helical phase front dependent on $exp(i\ell\phi)$, where ϕ is the angular coordinate and l was define before is an integer value (positive or negative), carries with it an orbital angular momentum (OAM). If we contemplate an angular momentum component propagating on the axis z, by definition, there must be a linear moment component propagating on the axes x and y [4].

As shown in the figure 3.4 the number of intertwined helices is determined by the value and sign of the integer l. These l intertwined helices have an azimuthal dependence determined by $exp(i\ell\phi)$, this allows the beam to carry an angular momentum in the direction of propagation [15]. For $l = 0$ we see that the wave is flat, there is no orbital angular momentum.

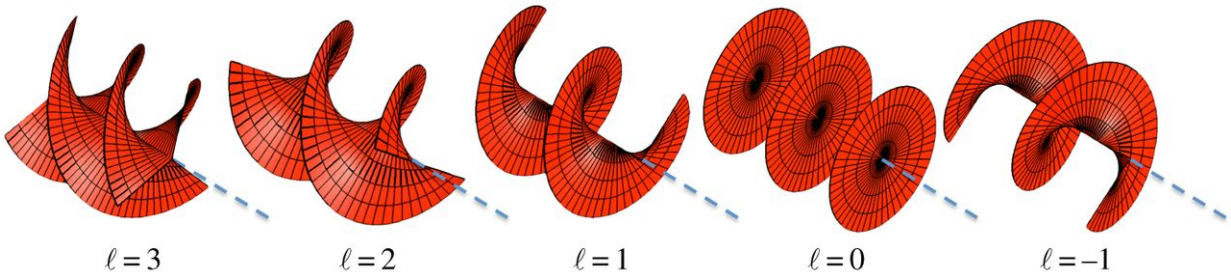

Figure 3.4: Beam with helically phasefront carries an orbital angular momentum $l\hbar$ per photon [16]

3.2 Generation of OAM

A Laguerre-Gaussian beam LG_p^l describe a set of propagation modes where the equation for the radial electric field is proportional to the product of a Gaussian and an associated Laguerre polynomial L_p^l. Currently, there are different ways to generate a Laguerre-Gaussian beam with a defined orbital angular momentum, with the purpose of transferring data and/or integrating this technology into telecommunications systems. All these methods have in terms of efficiency, working speed and stability or have specific requirements for the input light state. We will explain the four most known and used ways to generate an orbital angular momentum. [17]

3.2.1 Cylindrical lenses

The pattern of light propagation characterized by the concentration of energy around the axis of propagation is called the Gaussian beam. Although there are different kinds of Gaussian beams, each of them corresponds to a distribution of intensity in a cross section, we consider only the simplest way that is the fundamental Gaussian beam. [16]

This fundamental Gaussian mode (TM_{00}) describes the expected output of most lasers. When using lenses to focus the beam, the dependence it had with the transverse phase is altered, resulting in a different Gaussian beam. It is possible to decompose a coherent paraxial beam using the orthogonal set of the so-called Hermite-Gaussian modes. [15]

In 1979 Vaughan and Willets observed the interferogram coming from a high power laser when it was reflected in a mirror with its same mirror image. They deduced that the Hermite-Gaussian modes can be combined to obtain a helical phase beam [4]. To generate an OAM we can convert Hermite-Gaussian modes in Laguerre-Gaussian modes using an astigmatic system with two lenses arranged at a certain distance to introduce a phase between the horizontal and vertical Hermite-Gaussian rays.

The cylindrical lens mode converters have two main forms: the $\pi/2 - converter$ and the $\pi - converter$ (see figure 3.5).

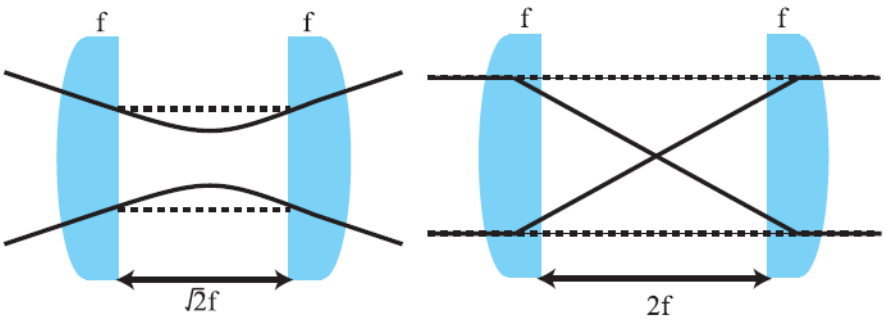

Figure 3.5: Cylindrical lens mode converters $\pi/2 - converter$ and $\pi - converter$ [4]

The $\pi/2 - converter$ transform a Hermite-Gussian incident beam of indices m, n, oriented at 45° to the cylindrical axis of the lens, into an LG mode with indices $\ell = m - n$ and $p = min(m, n)$ (see figure 3.6). So it works like a birefringent $\lambda/4$ plate.

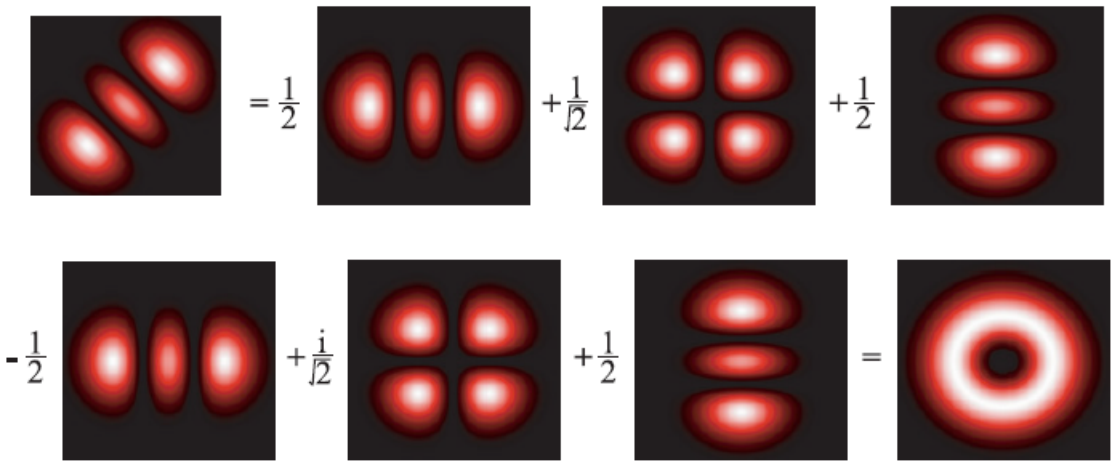

Figure 3.6: A HG mode at 45° can be decomposed in different HG modes, once re-phased, the combination of these modes results in a LG_{02} mode. [4]

The $\pi - converter$ transform the incident mode into its own mirror image and is equivalent to a Dove prism (see figure 3.7). So it works like a birefringent $\lambda/2$ plate.

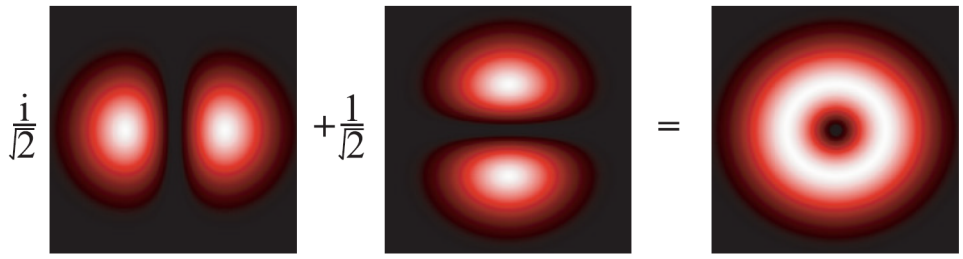

Figure 3.7: The combination of a Hermite–Gaussian mode HG_{01} with another one re-phased, HG_{10}, produce a Laguerre–Gaussian mode LG_{01} with helically phase [4]

3.2.2 Spiral Phase Plates

If we want to transform a plane wave to a wave with helical phase, perhaps a good method is use an optical element with helical surface. A spiral phase plate (SPP) converts a Gaussian input profile to an output one in the form of a "doughnut" whose energy is ring-shaped. [1]

The spiral phase plate is a structure that is composed of spiral steps or helical phase, which aims to control the phase of the transmitted beam (see figure 3.8).

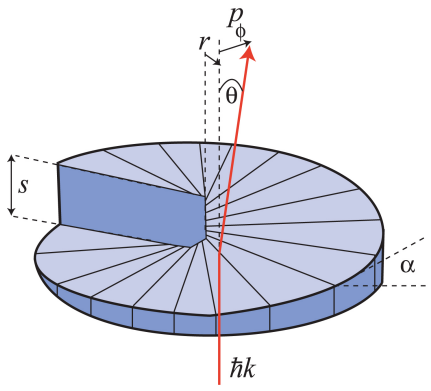

Figure 3.8: Spiral Phase Plate (SPP) [4]

The optical thickness of the component increases with the azimuth position according to $m\lambda\theta/2\pi(n-1)$, where n is the refractive index of the medium.

A spiral phase plate has a thickness which varies circumferally 'around' the plate, but is uniform radially. The plate is made of a dielectric material which is transparent. Hence a fundamental mode beam passing though the plate undergoes a phase-change which introduces a 'spiral' element into its phasefront. By choosing the appropriate plate geometry we can turn the beam phasefront into a "spiral staircase" pattern (see figure 3.9).

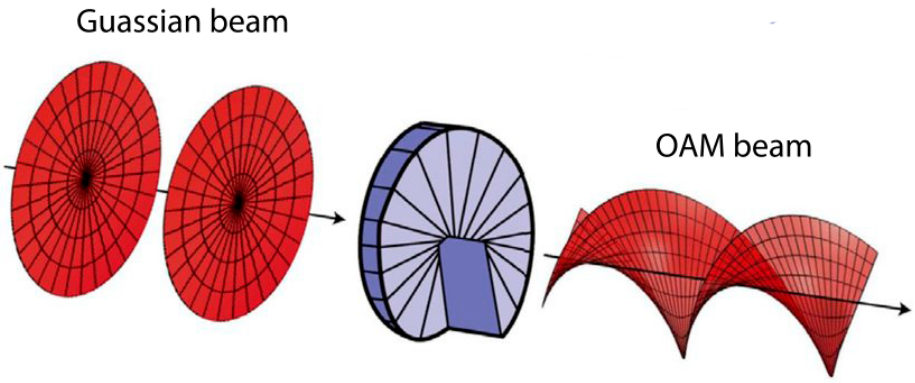

Figure 3.9: Spiral Phase Plate to convert Gaussian beam to OAM beam [4]

3.2.3 Q-Plates

A q-plate is a liquid crystal cell composed of a thin film of liquid crystal sandwiched between two pieces of glass and characterized by a unique pattern of molecular alignment, obtained from a process where the surfaces of the glass have been treated [15]. The pattern is defined mainly by a characteristic number, called topological charge and which characterizes the central singularity, which is usually denoted by the mathematical symbol q, from which the device took its name. In addition, the optical effect of the liquid crystal can be controlled electrically to have a partial effect on the plate. Since its creation in 2006, the q-plate has been useful in many applications of classical and quantum photonics. [4]

Under suitable conditions, the q-plates allow the exact conversion of the angular momentum SAM to the OAM form within the same beam of light (see figure 3.10). Classically, the q-plate has been used mainly to generate beams of light with OAM. In comparison with other methods to generate OAM (such as spiral phase plates and holographic elements), in practice, q-plates have certain advantages: they are thin optical elements that work in the transmission, with high efficiency of transmission and induction of deviation of light in the transmitted beam [8]; they are electrically controlled, as already explained; the OAM sign (that is, the direction of rotation) is controlled by the input polarization (the SAM sign) [15]. This last feature is very important for its use in communications, since the polarization can be changed quickly with electro-optical devices. [4]

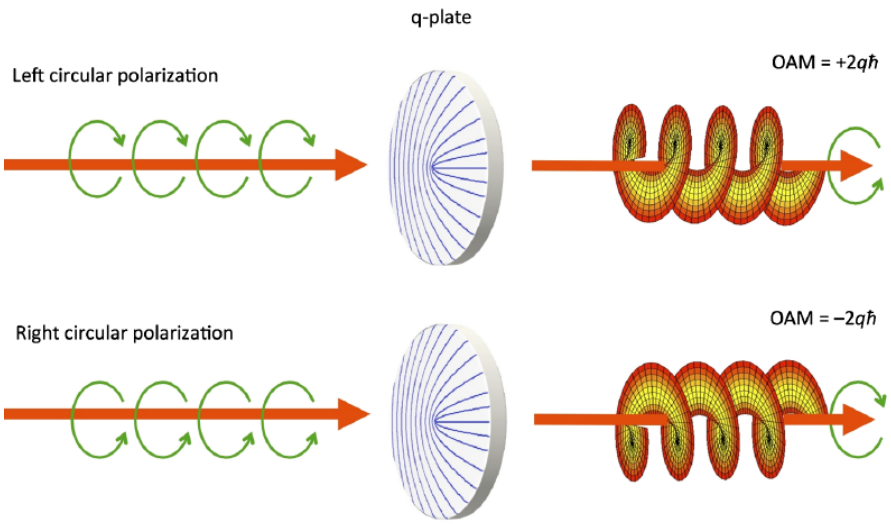

Figure 3.10: Optical effect of a q-plate depending on the input beam polarization [18]

3.2.4 Diffractive optical elements

The diffractive optical elements (DOEs), were designed for applications with high power lasers. They can be used as beam splitters of multiple points, in the conformation of the beam or to modify the profile of the beam, its use is immense in the field of photonic technologies. [17]

Given the need to generate more complex patterns, which otherwise would cost additional time, money and manufacturing, the optical diffractive elements (DOEs) are designed to mimic any refractive element according to our needs, although at a single wavelength . The device consists of a diffraction network that generates the first diffraction order of the desired beam (see figure 3.11). It can be said that it is like generating a hologram of the desired optical element, and thus, these elements are commonly referred to as "computer generated holograms". [16]

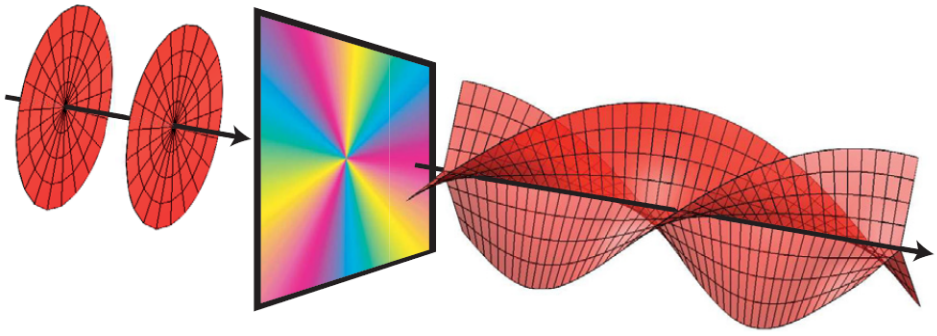

Figure 3.11: A helical phase profile generate a corkscrew wave front with an input Gaussian beam [4]

These holograms are generated by a device called Spatial Light Modulator (SLM), the main reason for using it is its commercial availability. A spatial light modulator is an object that imposes some form of modulation to the beam on which it is made to influence, this type of elements is usually manufactured with a liquid crystal in which its transparency can be controlled by a computer [2]. Changing your design is as simple as changing the image displayed by the computer that connects the device. An example where we can see an SLM working is in modern projectors, where you want to project the contents of a computer screen. Generally, an SLM modulates the intensity of the light beam or the phase [19]. However, it is possible to place several SLMs in series to modulate the intensity and phase simultaneously [4], the first of them to create the desired intensity distribution and the second to adjust the beam phase.

To produce helical beams, these holograms can take the form of bifurcated diffraction gratings [16]. In concept, a helical phase distribution applied to $exp(i\ell\phi)$ a Gaussian beam converts it into a desired helical beam. Combining this profile and a linear phase ramp,

a forked diffraction grating is obtained (see figure 3.12).

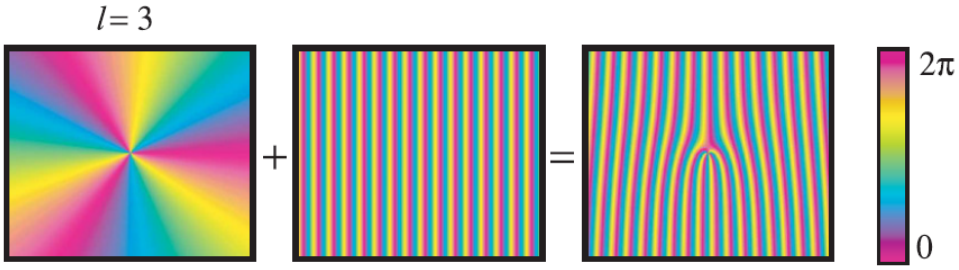

Figure 3.12: A forked diffraction pattern generated with the combination of the desired phase distribution ($\ell = 3$) plus a linear phase ramp [4]

Chapter 4

Setup

The objective of this chapter is to explain the process that was necessary to carry out the assembly of the experiment in the laboratory and the difficulties we had to face due to the complexity of working in free space. It will show the elements involved in the assembly of the experiment, as well as the purpose of its use, in addition to the software necessary to ensure a correct alignment or to load the phase masks that will help us generate an OAM.

4.1 Explanation

When we strike a beam of light on a rotating object, we observe that scattered light particles carry an OAM. This type of rotating Doppler shift is different from the known linear displacement, since it is independent of the optical frequency, which means that each spectral component of light is displaced by the same value [20]. This frequency shift is proportional to the order of the OAM with which we are working [21]. The purpose of carrying out this experiment is that the ability to observe this Doppler shift gives us the base to develop a rotational sensor for the remote detection of rotating objects.

The Doppler effect is a phenomenon in which the frequency undergoes a displacement due to the relative movement caused between a transmitter and a receiver. This frequency shift effect scales with the linear velocity with which the source approaches/moves away from the observer. Less well known than the linear displacement is the rotational, where the change in frequency is proportional to the rotation speed between the source and the observer and the orbital angular momentum (OAM) of the light, so that $\Delta\omega = \ell\Omega$, where Ω is the angular rotation frequency and the illuminated field carries an OAM of $\ell\hbar$ per photon. [22]

This rotating Doppler effect is manifested through a scattered laser beam of an object in rotation, even if the linear speed between emitter and receiver is zero [19]. Therefore, the dependence between the rotating Doppler shift and the orbital angular momentum of the light is very important and depends on the order of the angular momentum used to incise the beam of light on the surface of the object in rotation. [22]

In this work we will collect the steps taken to generate this OAM in a laboratory, how to generate it, how it interacts with the matter, how to measure it... We will carry out a series of characterizations in function of different parameters to try to study its behavioral. We will show the results obtained and discuss possible ways to improve the detection of this phenomenon. We will also talk about its future implementations in different areas and especially in the great potential it has in the field of telecommunications.

4.2 Devices and instrumentation we used

Next we will detail the devices and the instrumentation used to carry out the setup in the laboratory. The assembly that we must do is the following:

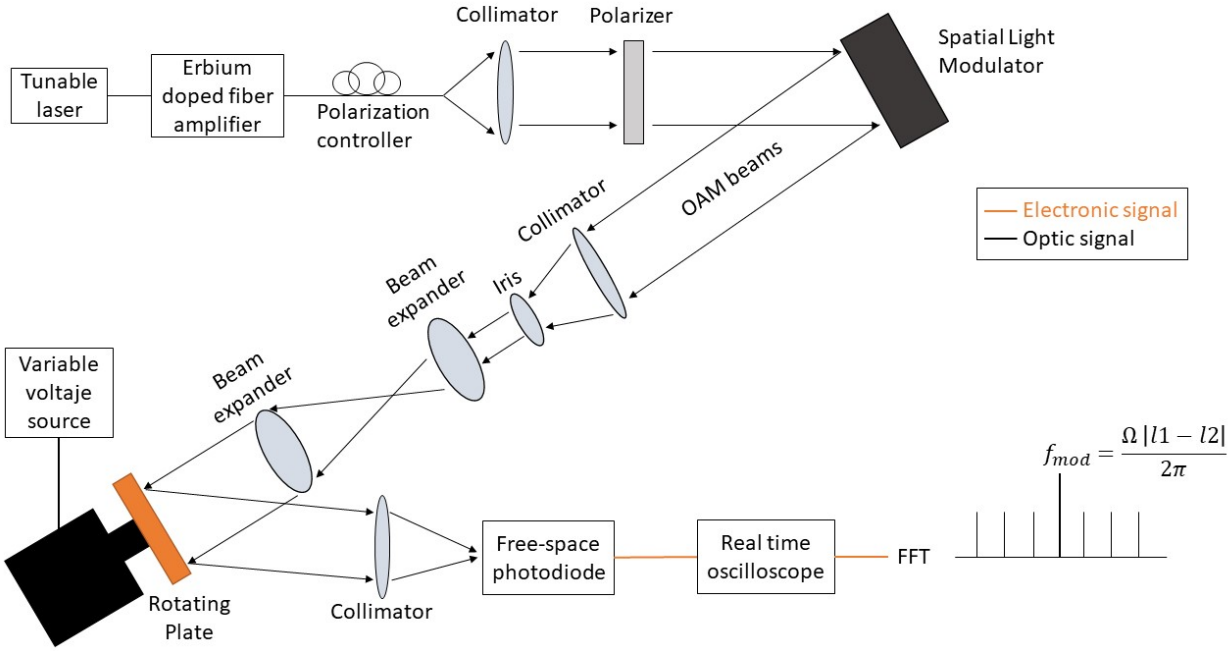

Figure 4.1: Main scheme of the setup

Tunable laser

OSICS Mainframe - Modular 8-channel mainframe: It consists of a multifunctional platform with a high selection of connectable modules, required for testing systems and fiber optic components. Up to 8 different modules can be mixed and combined to suply the needs of the applications that require it.

The front panel interface of the mainframe features a screen and a rotary button to easily navigate between the tabs of the module, as well as a quick configuration and control of the parameter values. The parameters are displayed in the main tab and are updated in real time.

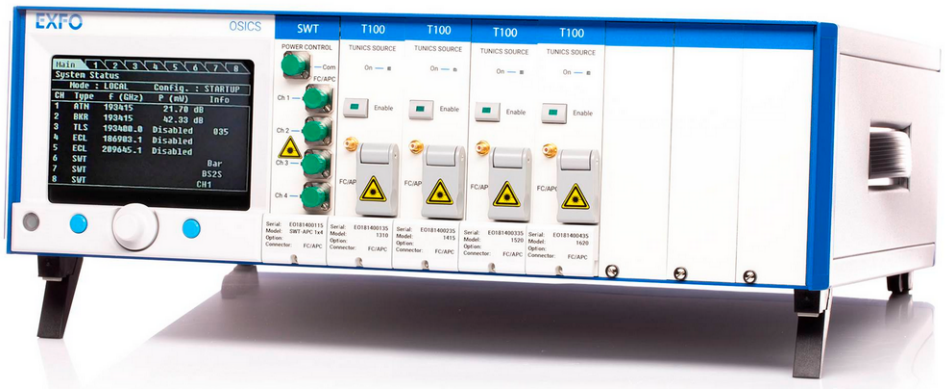

Figure 4.2: OSICS Mainframe - Modular 8-channel mainframe

The slot used to generate the beam is a TLS (Tunable Laser Source) ***OSICS TLS-AG - WDM tunable lasers***. It can be tuned to any wavelength in C-band. With more than 14 dBm (25 mW) of output power and wavelength stabilization.

Figure 4.3: OSICS TLS-AG - WDM tunable lasers

Erbium doped fiber amplifier

IPG Erbium Fiber Amplifier model EAD-500-C: IPG Photonics' EAD Series single-channel C-band ($1535 - 1570\ nm$) Erbium-doped Fiber Amplifiers are prepared to work in laboratory environments. It contains a front display showing the incoming power of the fiber, the output of the amplifier and the level of amplification that is applied.

The series of EAD amplifiers are used for research and development in fields such as telecommunications, photon switching, sensors and product testing. The input and output amplification is provided by a standard 1,5 meter SMF-28 fiber optic cable with input/output connectors. Normally, an amplifier has 40 dB of input and 30 dB of optical output isolation.

This element is very important since much of the assembly done in the laboratory is in free space so we will lose a lot of power due to the reflections and lenses used. We must consider the power we want to obtain at the output of the amplifier to avoid damage any component of the assembly, such as the photodiode or the infrared camera, but at the same time be able to watch something on the oscilloscope between the noise captured by the photodiode.

Figure 4.4: IPG Erbium Fiber Amplifier model EAD-500-C

Polarization controller

3-Paddle Polarization Controller: The fiber optic polarization controls use stress-induced birefringence produced by wrapping the fiber around two or three spools to create independent wave plates that will alter the polarization of light in a single-mode fiber. The axis of the movement of the vanes allows adjusting the polarization state of the arbitrary input. It allows to convert between linear, circular and elliptical polarization states, in addition to operating with the entire fiber bandwidth. It is suitable for FC/PC or FC/APC fibers.

The use of this element in the setup is to obtain the maximum possible power by manipulating the polarization of the light, the type of polarization at the output is not important, since later, with the use of the polarizer, we will obtain the necessary polarization to work with the SLM.

Figure 4.5: 3-Paddle Polarization Controller

Collimator

Collimator model F810APC-1550: The F810 series collimators are prealigned to collimate a laser beam that propagates from the tip of a fiber terminated in FC/PC, FC/APC or SMA. Because these collimators have no moving parts, they are compact and are not susceptible to misalignment. Due to chromatic aberration, the Effective Focal Length (EFL) of the lens depends on the wavelength. As a result, these collimators will only have optimal performance at the design wavelength.

Figure 4.6: Collimator model F810APC-1550

Polarizer

Polarizer LPMIR100-MP2: A polarizer is an optical filter that allows to pass a specific polarization, blocking the rest of the waves from other polarizations. It can convert an undefined beam or mixture of polarizations into a beam of a defined polarization. The most common types of polarizers are linear and circular. Polarizers are used in many optical techniques and instruments, and can be used with electromagnetic waves such as radio waves, microwaves and X-rays.

For our assembly, we need to isolate the vertical polarization of the others that carry the beam, this is because the HOLOEYEs SLM are based on vertical aligned nematic (VAN), parallel aligned nematic (PAN) or twisted nematic (TN), therefore we need to incide a vertically polarized beam.

Figure 4.7: Polarizer LPMIR100-MP2

Spatial Light Modulator

Spatial Light Modulator PLUTO-2: A spatial light modulator is a device used to modulate the amplitude, phase or polarization of light in space and time. The SLMs are based on translucent (LCD) or reflective (LCOS) liquid crystal microdisplays. As we have said before, HOLOEYEs SLMs can have a vertical (VAN), parallel (PAN) or twisted (TN) alignment.

The spatial light modulator PLUTO-2 consists of a controller unit with standard digital video interface (HDMI) and an LCOS microdisplay (liquid crystal on silicon) for phase with Full HD resolution (1920 x 1080). It is enough to load the desired pattern to modify the phase of the reflected beam on the display.

Figure 4.8: Spatial Light Modulator PLUTO-2

Iris

Iris SM1D12D: The main role played by the iris here is to prevent the harmonics generated in other directions because of the reflection of the laser beam in the SLM can not be incorporated by some reflection back to the assembly, altering the measures we must perform.

Figure 4.9: Iris SM1D12D

Beam expander

Beam expander: A laser beam expander is designed to increase the diameter of a collimated input beam to a larger collimated output beam. Between two beam expander there is a focal length and a focal point where the beams are concentrated.

Figure 4.10: Beam expander

Variable voltaje source

Power Supply PL154: The voltage source will feed the motor that will spin the plate on which we will make the beam to finally measure the Doppler shift that is generated. We must be careful with the vibrations that can appear when the voltage increases too much, we should avoid them since when working in free space the alignment is crucial.

Figure 4.11: Power Supply PL154

Rotating plate

It is just a surface to adhere to the engine to make it spin. The surface is totally smooth but we will put different rough surfaces on top so that there is the greatest number of scattered rays, which will be measured by the photodiode.

Figure 4.12: Rotating plate

The types of surface used were the P40 E28 Imperial professional 140/1706 and the P80 E28 Imperial professional 140/1708, from less to higher roughness respectively.

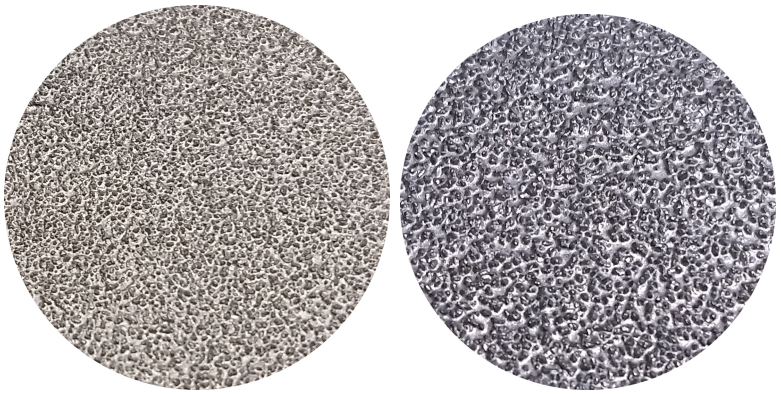

(a) P40 E28 surface (b) P80 E28 surface

Figure 4.13: Imperial professional surfaces

Free-space photodiode

Photodiode DET20C/M InGaAs Biased Detector: A photodiode is a device that converts light into electrical current, this current is generated when the photodiode absorbs photons. The material used in the manufacture of the photodiodes is important to define the properties of the same since the photons with sufficient energy will manage to excite the electrons and generate photocurrent.

Figure 4.14: Photodiode DET20C/M InGaAs Biased Detector

Real time oscilloscope

Oscilloscope LeCroy WaveRunner 64 Xi: The oscilloscope is used for visualization and representation of electrical signals for the photodiode. Represents electrical signals in the form of coordinates on the X and Y axis. Because we are going to work with ranges where the difference between samples will be of the order of hertz, we need a large number of samples to avoid losing crucial information, so the oscilloscope chosen has an acquisition rate of 10 giga-samples per second (GS/s). It also allows us to apply transformations mathematical transformations such as FFT (Fast Fourier Transform) that will be very useful when evaluating the final data.

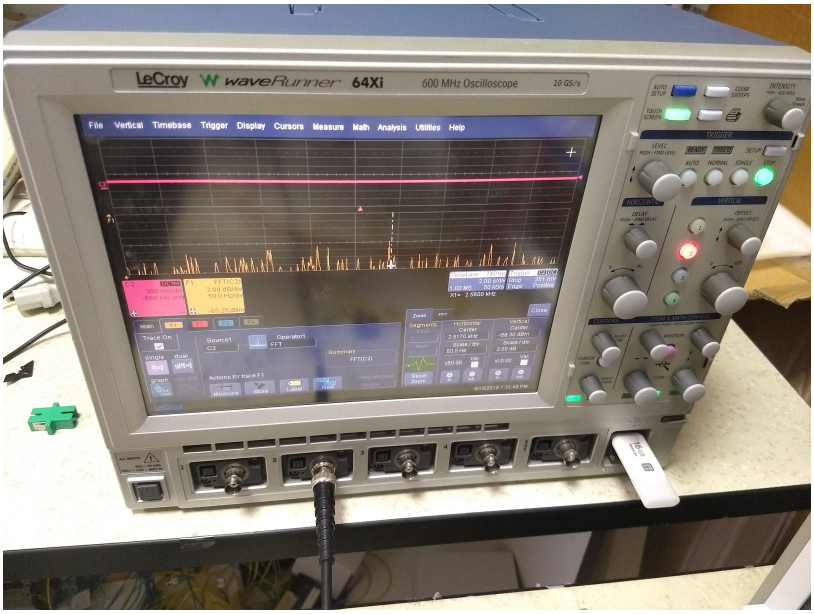

Figure 4.15: Oscilloscope LeCroy WaveRunner 64 Xi

Camera and components

Camera Xenics XS-4440 XEN-000122: This camera will help us in alignment tasks and to verify that the laser beam carries an OAM. We must be careful with the power with which the beam hits the camera because we could damage it, so it will be necessary to use attenuation lenses to reduce the luminosity with which the beam hits the camera.

Figure 4.16: Camera Xenics XS-4440 XEN-000122

As for the lenses used, these are some of the models: NENIR30A, NENIR20A, NENIR10A, NENIR03A.

(a) NENIR30A (b) NENIR20A (c) NENIR10A (d) NENIR03A

Figure 4.17: Atenuation lens

Connectors

Fiber optics cable: The 2 types of optical fibers used in the assembly were of the monomode type, with FLAT and APC polishing, whose connector model was FC. The insertion losses that both types present are around $0,2\ dB$ and $0,4\ dB$.

Figure 4.18: Fiber optics cables - FC Connector

Due to the flat surface coupling (FLAT), its properties make it uncritical in terms of loss of return, placing it around 40 dB. On the other hand, the angular polishing (APC) causes the reflections of the light transition not to return to the core of the fiber, which increases the return loss to values around 60 dB.

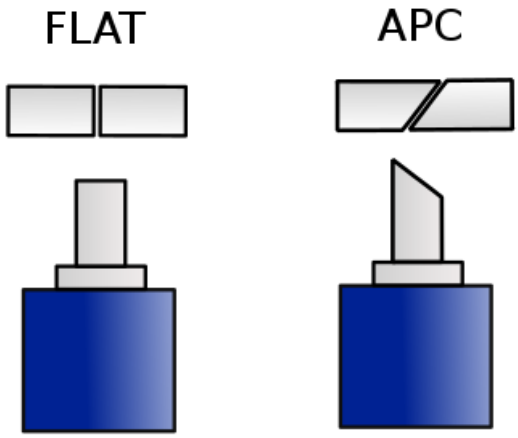

(a) FLAT polishing (b) APC polishing

Figure 4.19: Surface of the connectors

BNC connector: Used to transport the electrical signal of the photodiode to the oscilloscope. It is a cable commonly used to work with measuring equipment such as oscilloscopes.

Figure 4.20: BNC connectors

Other components used

Power meter PM16-122: It allows us to remotely measure the power of a beam through an interface on a computer via USB. It is capable of absorbing light at around $400 - 600\ nm$ and $800 - 1700\ nm$.

Figure 4.21: Power meter PM16-122

Detector Card VRC2: It is equipped with a photosensitive surface that allows to locate a beam of light in a simple way. Its function is only to help us with the alignment of the setup. It allows you to visualize a beam whose wavelength is between $400 - 640\ nm$ and $800 - 1700\ nm$.

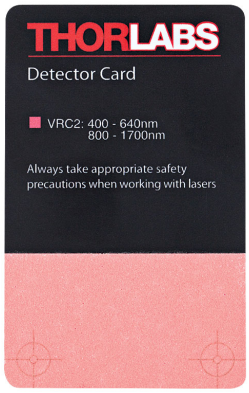

Figure 4.22: Detector Card VRC2

4.3 Software used

Software for camera

Xeneth: Thanks to this software we can control the infrared camera, its main function will be to help us observe if the beam reflected in the spatial light modulator carries an OAM and with alignment tasks of the setup, also, it can help us to control that no element of the setup is partially blocking the main beam, being disastrous for data collection. As we said before, we must be careful with the power of the beam that we are going to observe since the photosensitive surface could be damaged, for this we have at our disposal a set of attenuation lenses to protect the device.

Software for powermeter

Thorlabs optical power meter utility: The function of this application is simple, give us a measurement of the power carried by the beam at any point of the setup. It is especially useful for fixing the photodetector once the beams are dispersed by the rotating surface, allowing us to place it in the direction in which it is capable of capturing more energy. This is very important, since alignment is crucial to detect OAMs.

Software for SLM

HOLOEYE SLM Application Software 2.2.7 for the PLUTO: This software allows us to load the phase masks to the spatial light modulator so that, when the light beam is reflected on the display, it carries an orbital angular momentum. In our case we will load phase masks with a fork pattern, later we will explain why. Of course, there are other patterns that can be used as lines, spirals ... that can be generated on Matlab.

How can we generate phase masks of any order $l = \pm1, \pm2, \pm3, \pm4...$, to simplify we have established a range of values when creating masks to be able to study the behavior of the OAM, creating the patterns for the integers $l = 10,\ 20,\ 30,\ 40$ y 50. In this way we can study their behavior from the smallest OAM radius ($l = 10$) to the largest one ($l = 50$).

For our experiment, we want to measure the frequency modulation generated by the superposition of two OAM, the best option for these cases is to use the fork pattern phase mask. Therefore, the orders that the OAM will take will be $l = \pm10,\ \pm20,\ \pm30,\ \pm40$ and ±50.

4.4 Assembling and aligning the setup

In this section we will briefly explain the steps taken to assemble and correctly align the set-up, the problems that arose during the process and important considerations when working with the components and devices used.

The first thing we thought was that, when working in a setup in free space with a photodiode that can detect the light of the environment (to a certain point depending on the sensibility it has), we should try to assemble it in a space where the outside light and the light inside the laboratory will affect as little as possible. With this we wanted to provide the best possible conditions to carry out the experiment.

When we work with optical technologies we should not worry about the radiation in the form of heat generated by nearby equipment (laser source, optical amplifier, voltage source and oscilloscope), since the signal transmitted through a fiber cable has immunity to the external radiations of any kind.

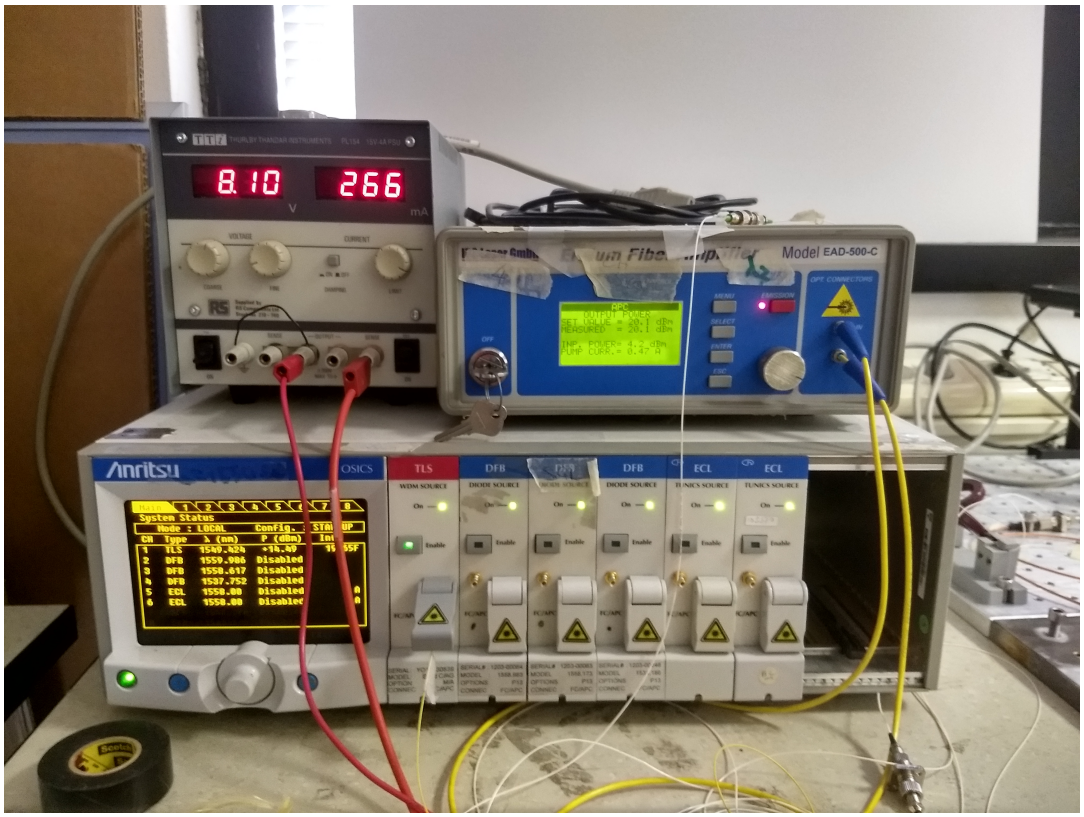

Figure 4.23: Setup picture 1

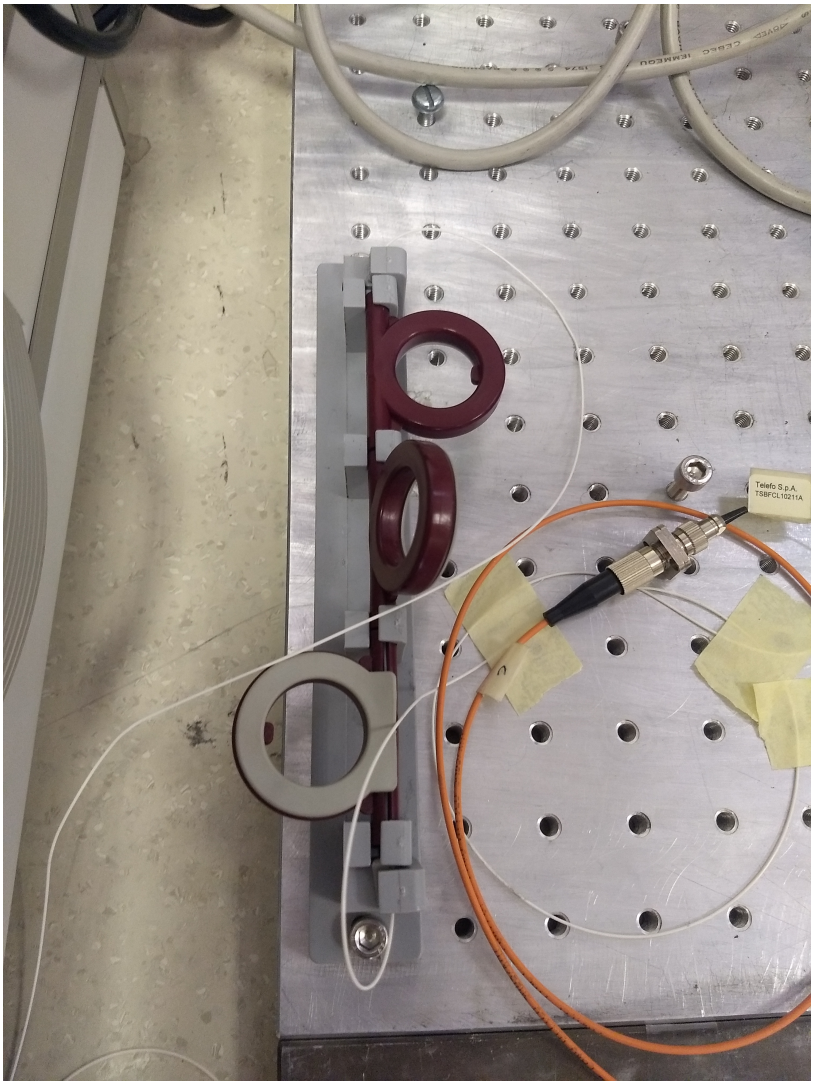

Figure 4.24: Setup picture 2

As for the part of fiber-guided optics that consists of the laser source section, followed by the optical amplifier, the polarization controller and finally the collimator, care must be taken to ensure that the radius of curvature of the fibers is not very sharp to avoid light leaks and therefore loss in power that is guided by the cable.

- The laser source was configured to generate a beam of $1549,42\ nm$ wavelength and $14,49\ dBm$ of power.
- The optical amplifier was used with 10 dB of amplification when we used the infrared camera to align the setup and with 20 dB of amplification to perform the characterization.
- The polarization controller was adjusted obtained as much energy as possible at the output of the collimator, regardless of the type of polarization, since later the polarizer will only let vertical polarization pass through.

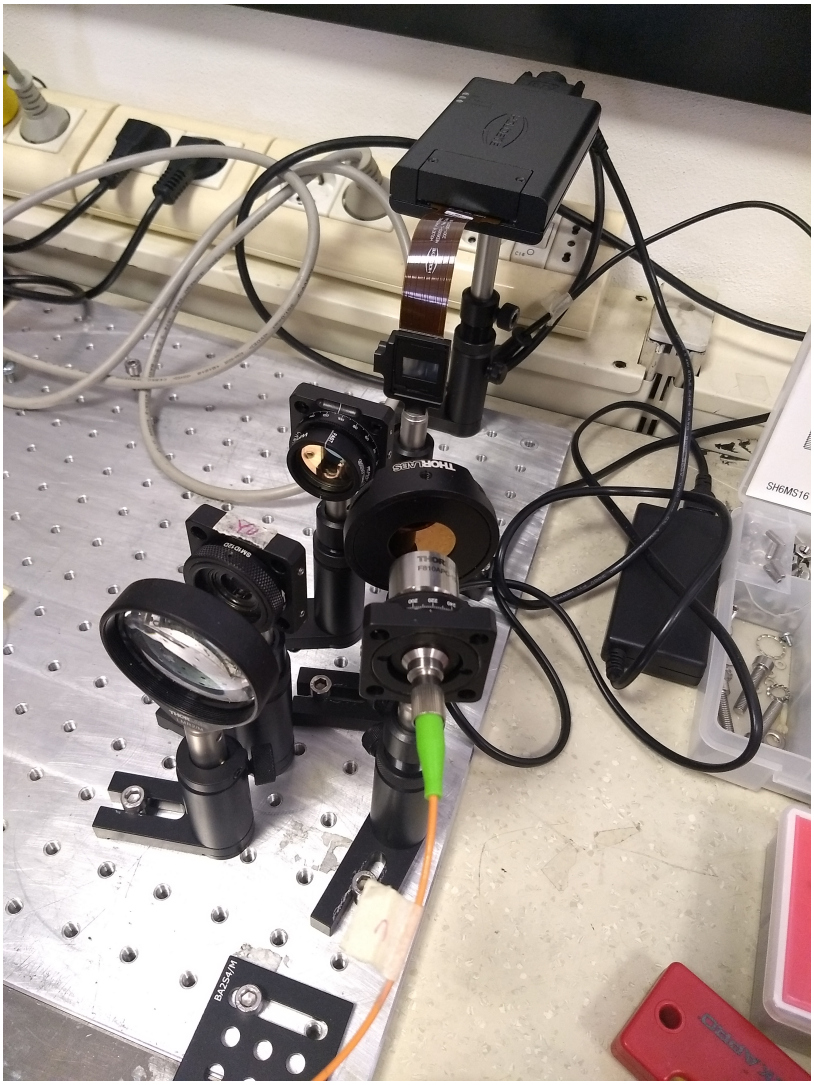

Figure 4.25: Setup picture 3

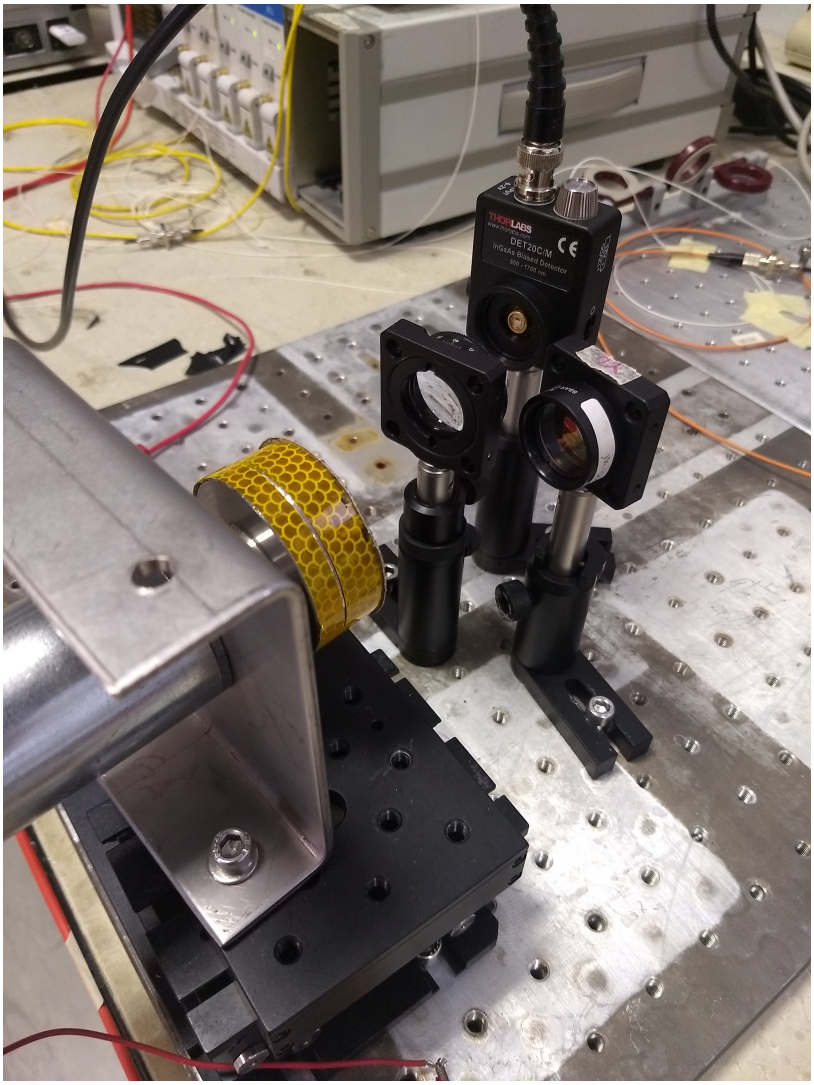

Figure 4.26: Setup picture 4

The setup has a motor to turn the plate with the rough surface to which we will make the beam impact. When the engine is put into operation, it will generate mechanical vibrations that will be transmitted throughout the mounting surface. These vibrations depend mainly on the amount of voltage supplied, so it will be taken into consideration when making the measurements. That there are vibrations in a setup of these characteristics is something that can affect in a very negative way the data collection where the alignment of the elements is crucial.

- As for the voltage source to power the motor, we use a range of voltages of $8.1\,V$, $9\,V$, $10\,V$ and $11\,V$.
- The motor is coupled to a platform that allows us to adjust it vertically and horizontally to adjust it to the optimum position so that the beam can strike perpendicularly in the center of the surface. In the same way, it will serve to misalign the beam with respect to the center and see how this affects the frequency modulation.

- The plates coupled to the engine have two types of rough surfaces, one with greater roughness than the other, to see how each affects the dispersion of light when we do the characterization.

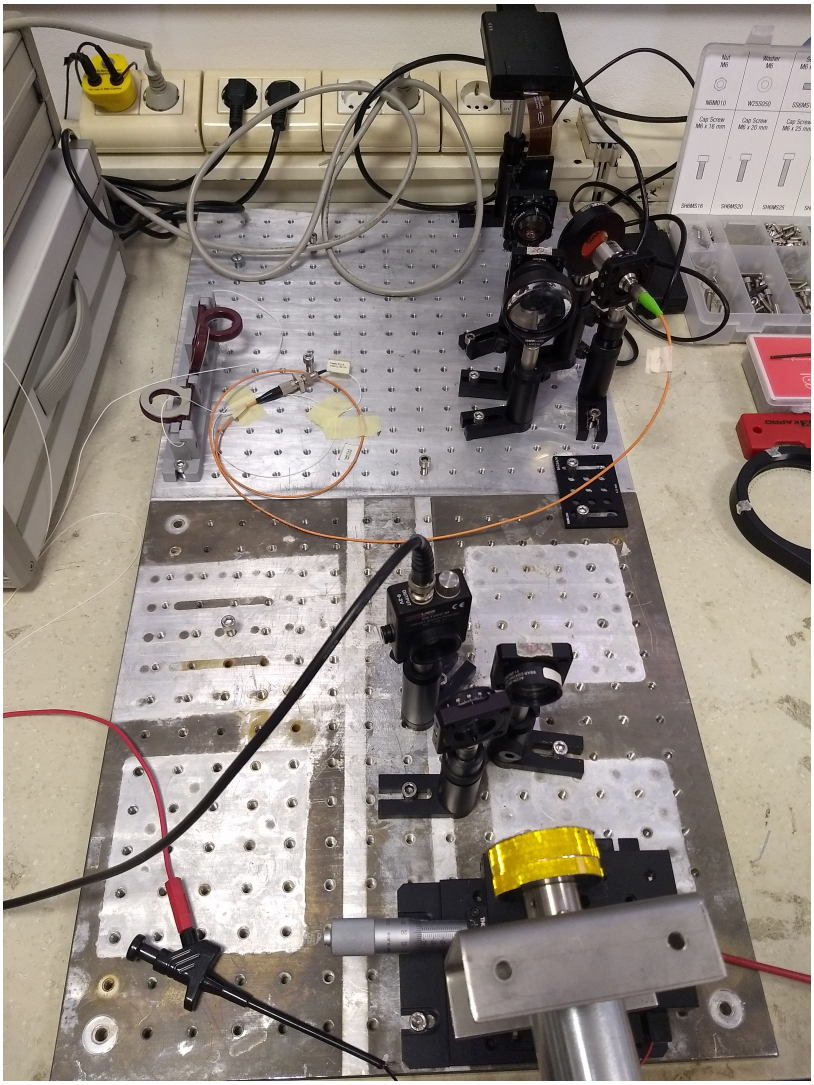

Figure 4.27: Setup picture 5

Regarding the optics in free space we highlight a couple of considerations to take into account. The SLM is the main element of our setup, it allows us to load patterns of phase masks to generate a beam that carries an OAM. As we said before, there are different phase masks that we can use, in our case we are looking for the superposition of two OAMs that generate a frequency modulation that we can detect with the photodiode, for this we use a fork phase pattern. In addition, the SLM has limitations regarding the maximum angle with which a beam of light can strike, when this angle of incidence exceeds $10 \sim 15°$ with respect to the perpendicular of the display the phase modulation is considerably reduced.

- The SLM is loaded with fork phase pattern of orders $l = \pm 10,\ \pm 20,\ \pm 30,\ \pm 40$ and ± 50.

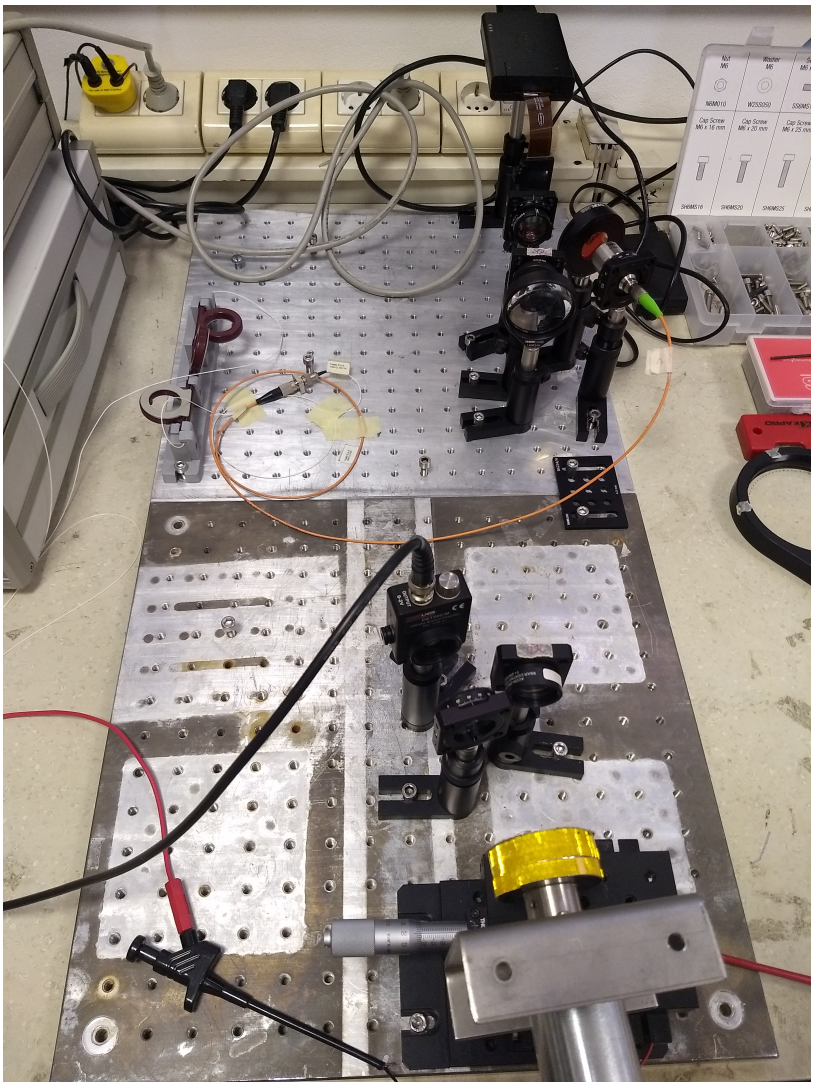

Figure 4.28: Setup picture 6

On the other hand, the placement of the lenses and the photodiode was thanks to the use of the powermeter and the infrared camera, which helped us to align the lenses along the beam's path. In this way, we got the path with less losses.

- The two beam expanders of the setup are separated by a focal distance of 26 *cm* and the focal point is located at 14 *cm* with respect to the first beam expander that is crossed by the beam.
- The beam expanders increase the diameter of the collimated beam, which will directly affect the diameter of the OAM. In the characterization we will check if this

increase in diameter corresponds to a redistribution of the energy along the generated ring.

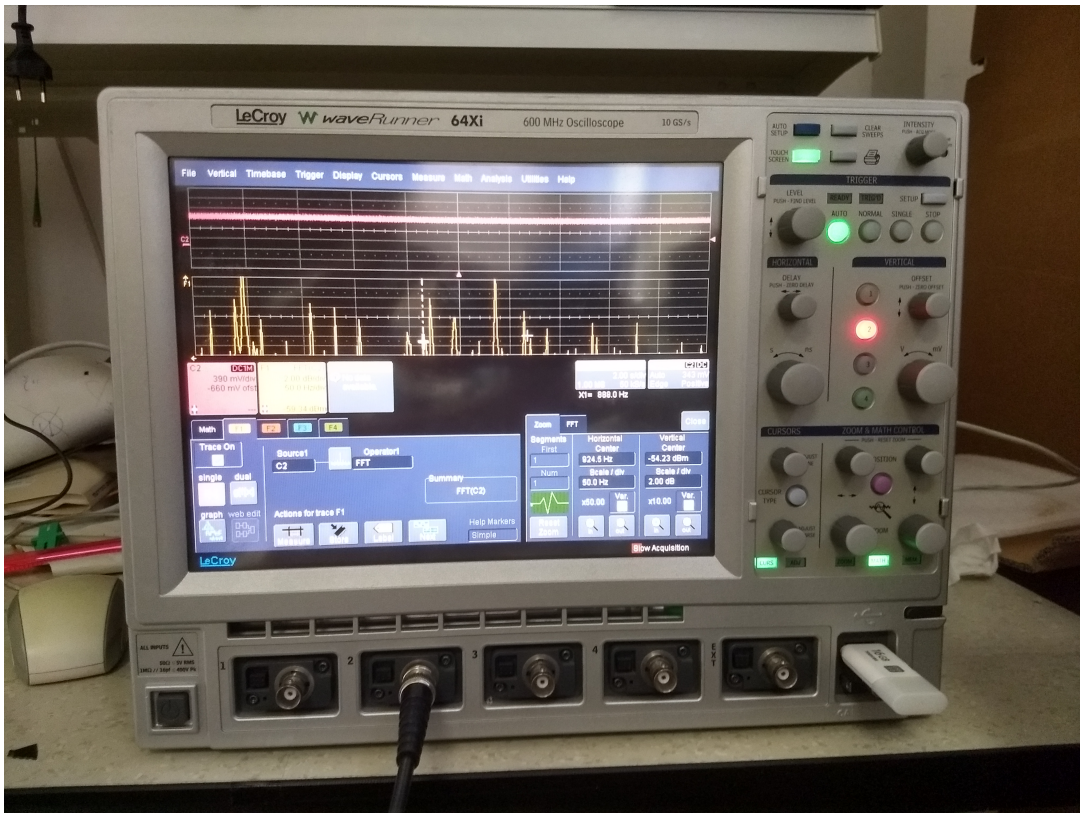

Figure 4.29: Setup picture 7

Finally, the only electrical stage is the union between the photodiode and the oscilloscope, the light absorbed by the photodiode is converted into electrical pulses in order to be interpreted by the oscilloscope.

- For the correct visualization of the information we will apply an FFT function to the incoming data and the scales of the display to 2 dB/div and 50 Hz/div. In addition, to seeing the energy that carries the modulation in frequency in mV/div with an offset of -645 mV.

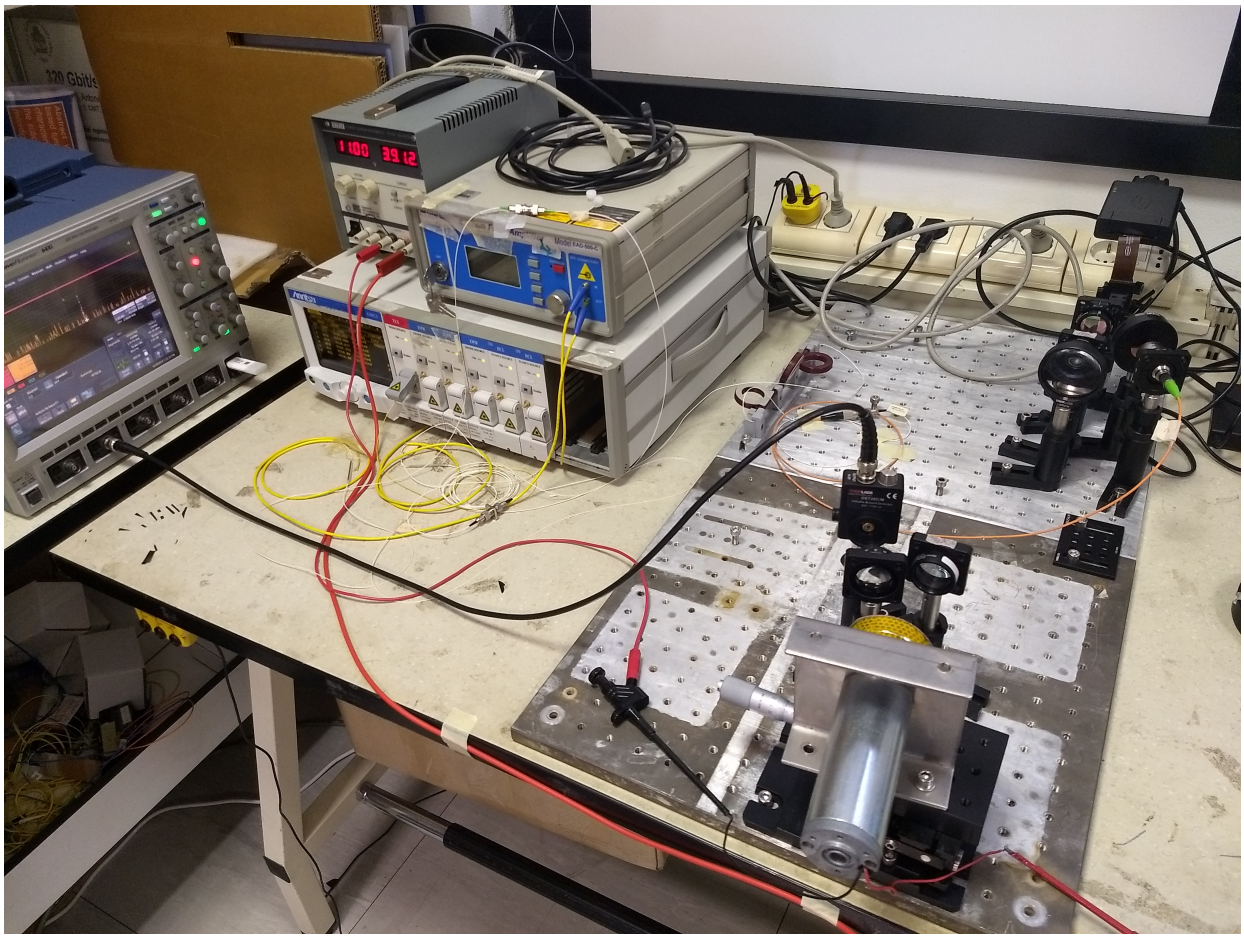

Figure 4.30: The complete setup

Chapter 5

Characterization

In this chapter we will expose the results obtained for each of the characterizations that we have carried out. Theoretical and practical results carried out in the laboratory will be compared. The analyzes carried out will cover the use of different surfaces on which we will reflect the beam, with the use (or not) of the beam expanders, displacement of the beam to misalign it, increase in the speed of the disk and other analyzes.

5.1 How to observe the rotational Doppler shift

We will observe the rotational Doppler shift generated by the superposition of two OAMs when they are scattered by a rotating object. We will see how the magnitude of this displacement is dependent on the order of the OAM that carries the beam of light. As we explained in the previous chapter, a laser source generates a beam at a given wavelength, the beam goes through an optical amplification and through a polarization controller until it exits through a coupled optical fiber. The output of this fiber passes through a collimator to disperse the beam and through a polarizer to keep only with vertical polarization, since the spatial light modulator works with this polarization. The reflected beam will have a helical wavefront and an order of OAM given by the phase mask that we load in the SLM. Then it will pass through another collimator to concentrate the beam and through an iris that will avoid the passage of the generated replicas that are dispersed in other directions by the SLM. Next, it passes through a beam expander and bounces off the axis of a rotating plate with a rough surface. The scattered light is then concentrated by a collimator and collected by a photodiode. The output of the photodiode is digitized and transmitted to an oscilloscope where an FFT is applied so that we can observe the frequency spectrum.

In the figure 5.1 we can see a typical power spectrum of the intensity fluctuations generated by the beam scattered on the surface in rotation. This example is obtained from the interaction of the OAM with orders $l = \pm 12$ on a surface with angular velocity $\Omega = 243\ rad\ s^{-1}$.

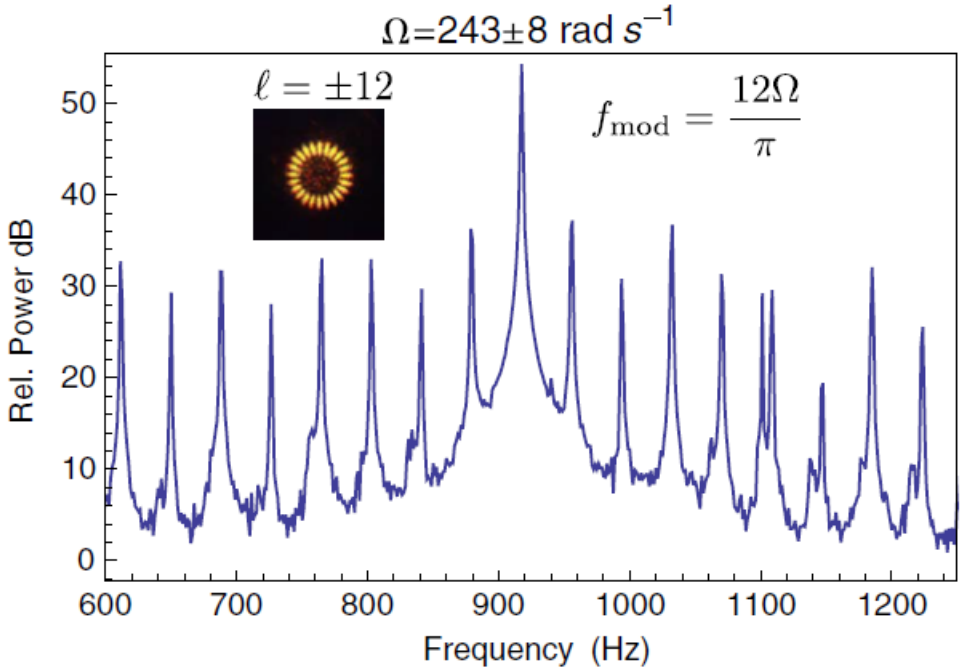

Figure 5.1: Typical power spectrum of the intensity fluctuations [19]

On the other hand we have in the figure 5.2 a graph showing the frequency modulation, where the peak with the most power of the whole spectrum is found, based on the speed of rotation of the surface for the superposition of different orders of the OAM modes, in this case, $l = \pm 8,\ \pm 10,\ \pm 12,\ \pm 14$. The speed with which the receiver rotates is directly linked to a frequency shift for the modulation frequency. The intensity of each section corresponds to a symmetrical petal pattern with $|l_1 - l_2|$. As an anticipation, the power spectrum reveals a peak in intensity modulation at an angular frequency $f_{mod} = \Omega|l_1 - l_2|/2\pi$. The peak located at this frequency must have a peak power greater than the rest of the spectrum. The appearance of other peaks is due to the modal impurities that are inherent in lateral or angular misalignment, or aberrations in the optical system [19].

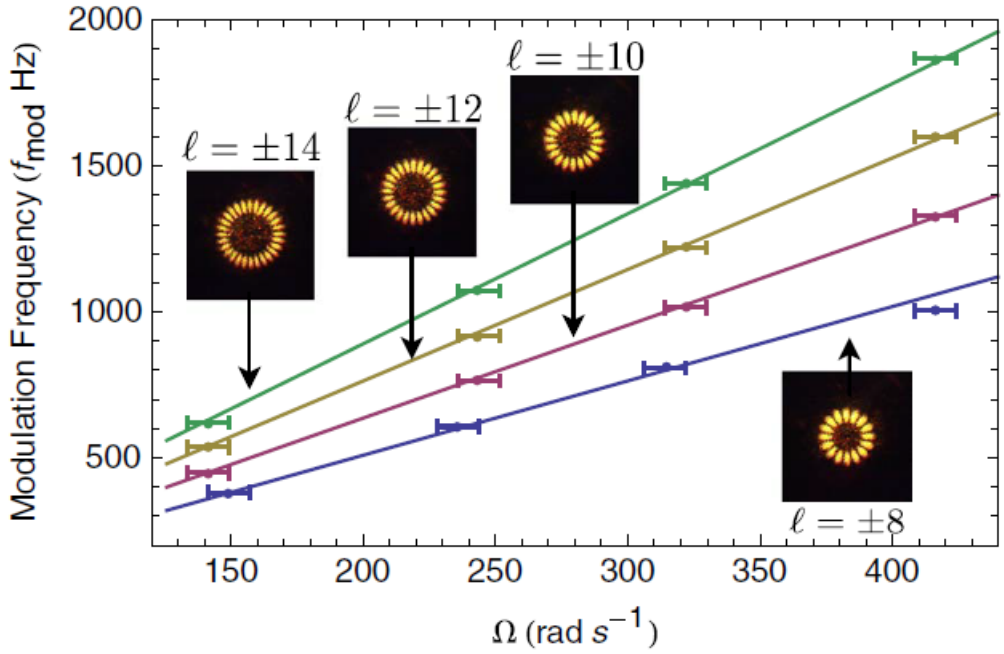

Figure 5.2: Observed modulation frequency plotted as a function of rotation rate [19]

Therefore, the modal superposition results in an observable frequency change, the observability of the rotational Doppler shift gives rise to its applicability for the remote detection of rotating objects.

Next, we will start the characterization of this rotational Doppler shift according to different setup parameters such as the roughness of the surface on which the beam hits, the speed with which the surface rotates, the misalignment of the axis with respect to the OAM, the OAM orders that we overlap or the modification of the own setup, adding and removing lenses. Before starting to expose results we will show the phase masks we have used in the SLM to generate the different OAM orders and with the infrared camera we will observe how they change the light pattern. At the same time, we will see that the size of the OAM is dependent on the order that we generate with the phase mask, the greater the order of the mask, the greater the radio of the OAM.

So, the phase masks we have used are fork type and are useful to generate an overlap of two OAMs, which we need for our tests since we want to measure the rotational Doppler shift. The particularity that this mask has is that, when striking a beam, the reflection is the superposition of the order of the phase mask plus another in the opposite direction, in this way we obtain a reflected order $\pm l$. As we said in the previous chapter, the SLM has been loaded with a frok phase pattern with orders $l = \pm 10,\ \pm 20,\ \pm 30,\ \pm 40$ and ± 50. Figures 5.3-5.7 show the fork phase masks used in the SLM.

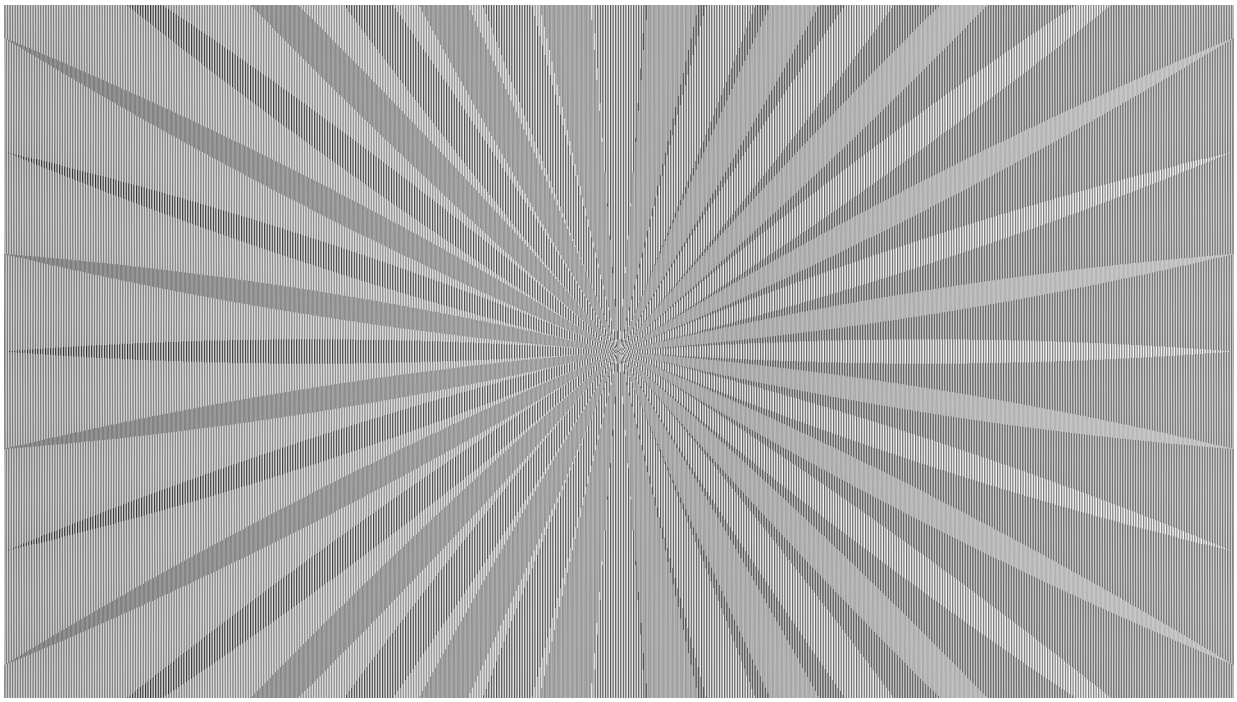

Figure 5.3: $l = 10$ fork phase pattern.

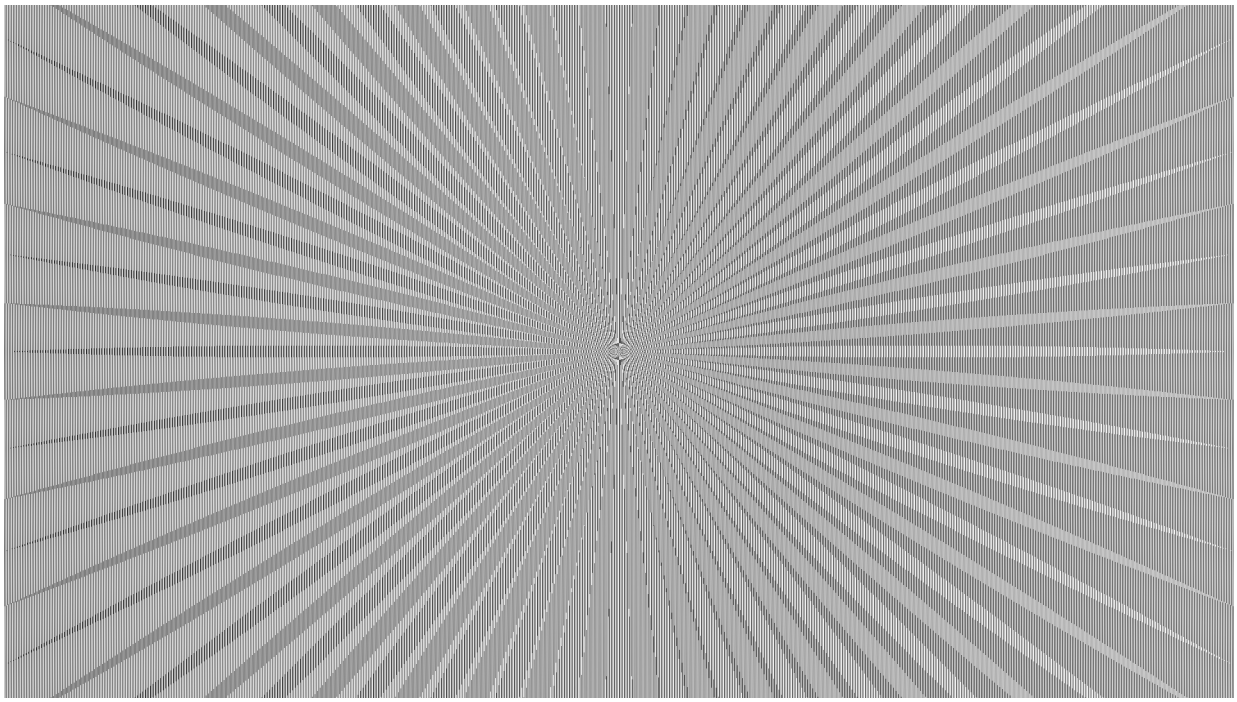

Figure 5.4: $l = 20$ fork phase pattern.

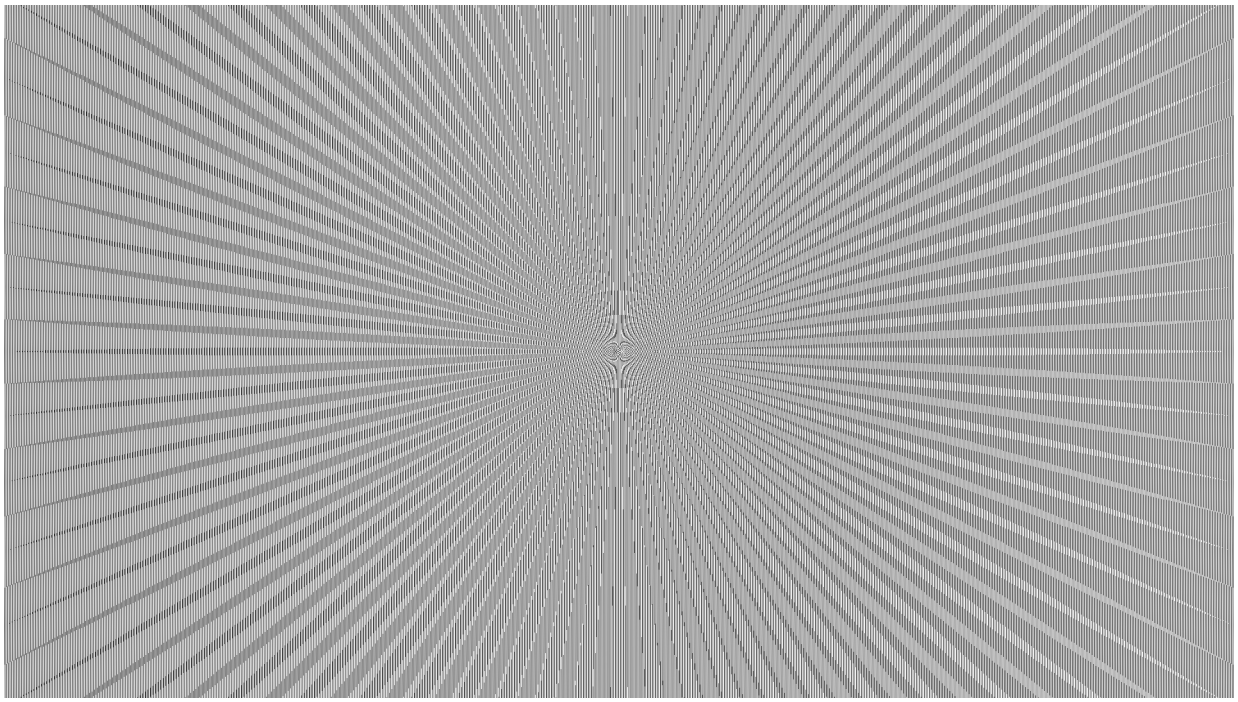

Figure 5.5: $l = 30$ fork phase pattern

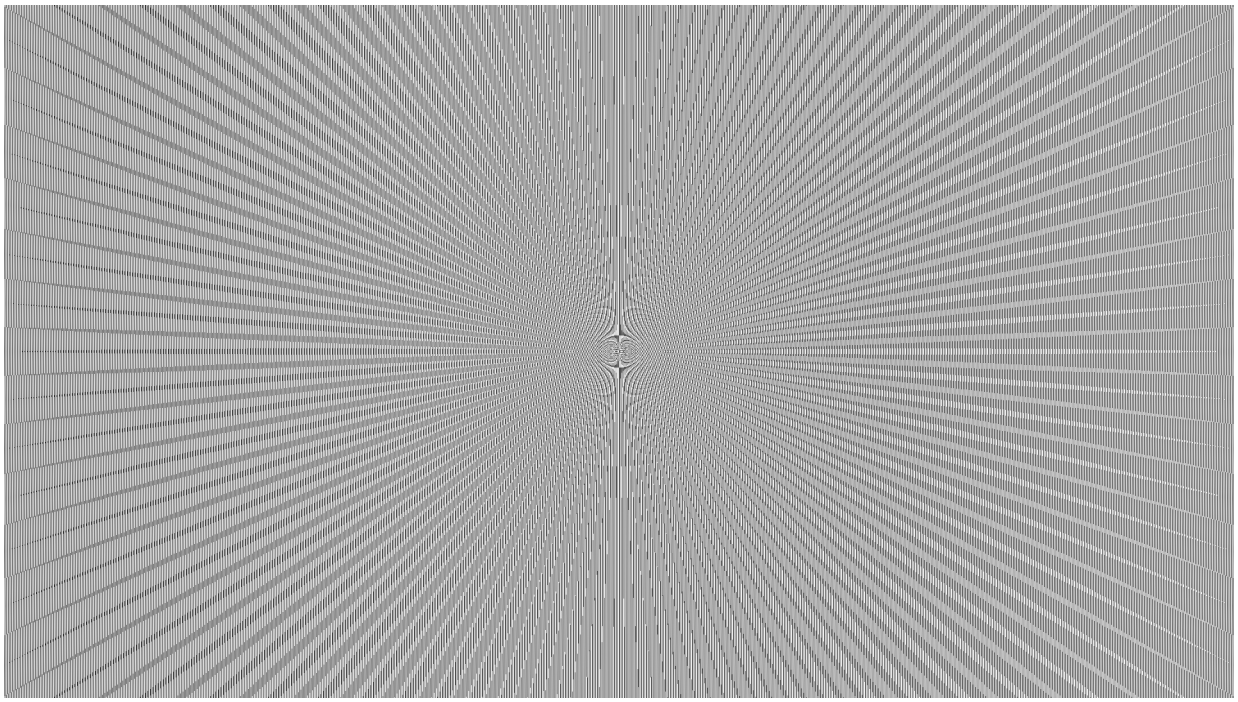

Figure 5.6: $l = 40$ fork phase pattern

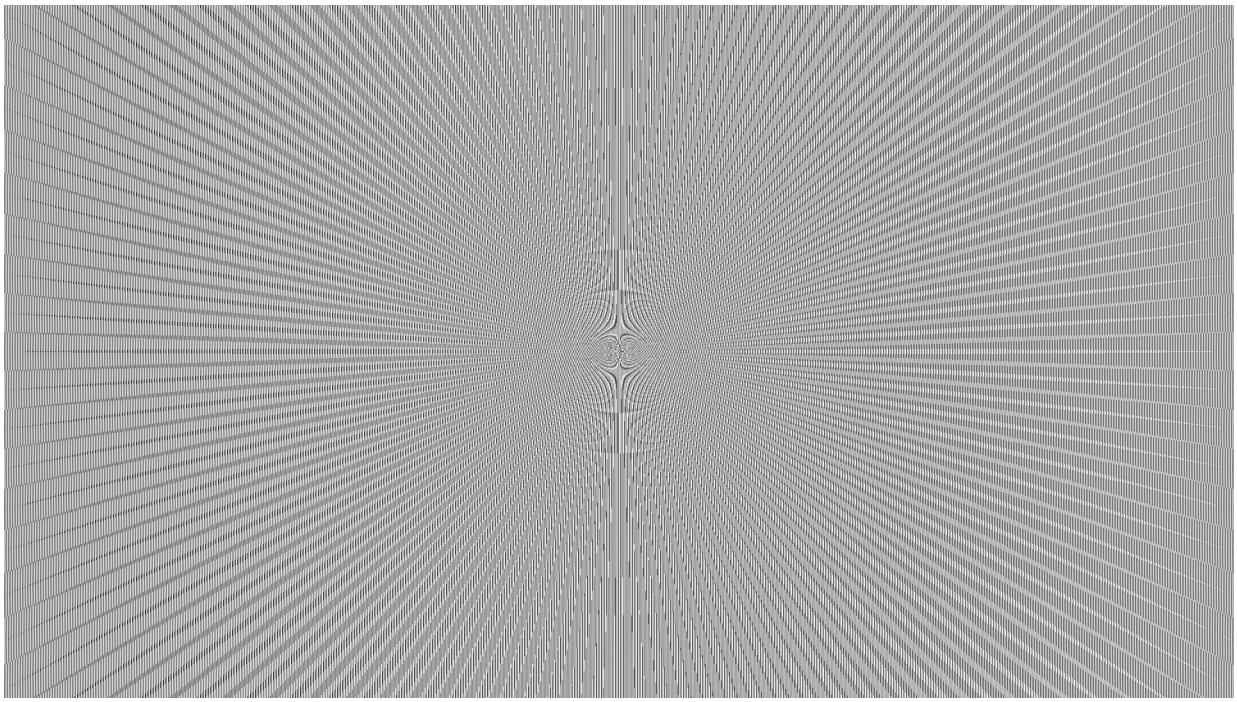

Figure 5.7: $l = 50$ fork phase pattern

Now we are going to see with the infrared camera which is the light pattern that is formed when the beam is reflected in the SLM, this depends directly on the order of the phase pattern that we load. So, we get the light patterns in figures 5.8-5.12.

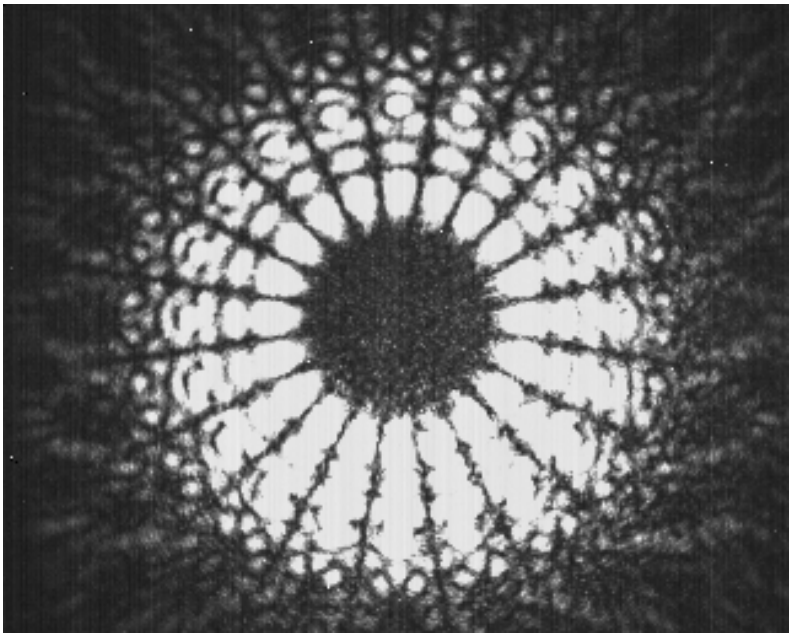

Figure 5.8: OAM of order $l = 10$

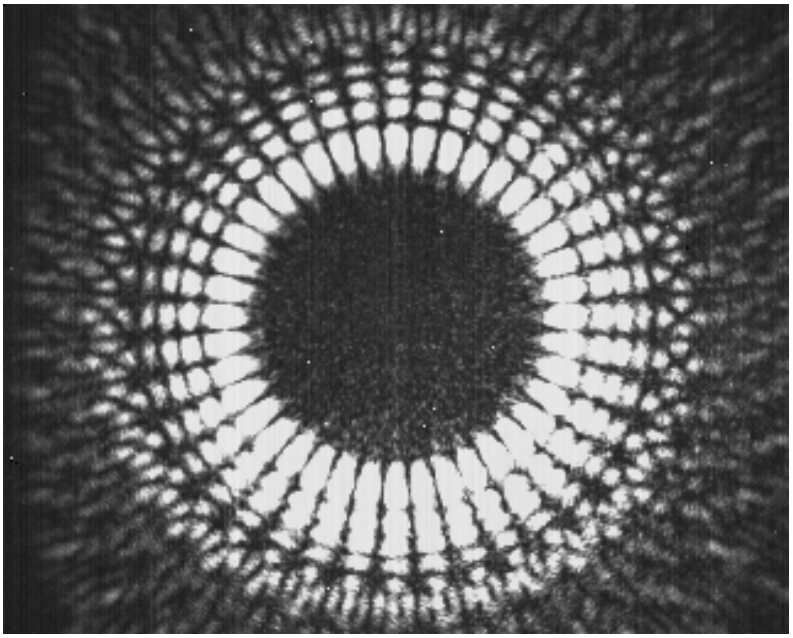

Figure 5.9: OAM of order $l = 20$

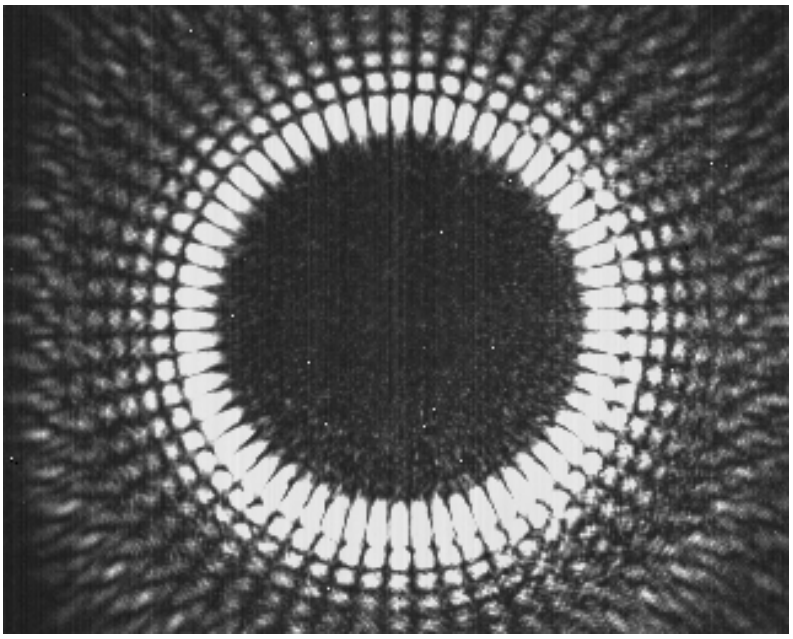

Figure 5.10: OAM of order $l = 30$

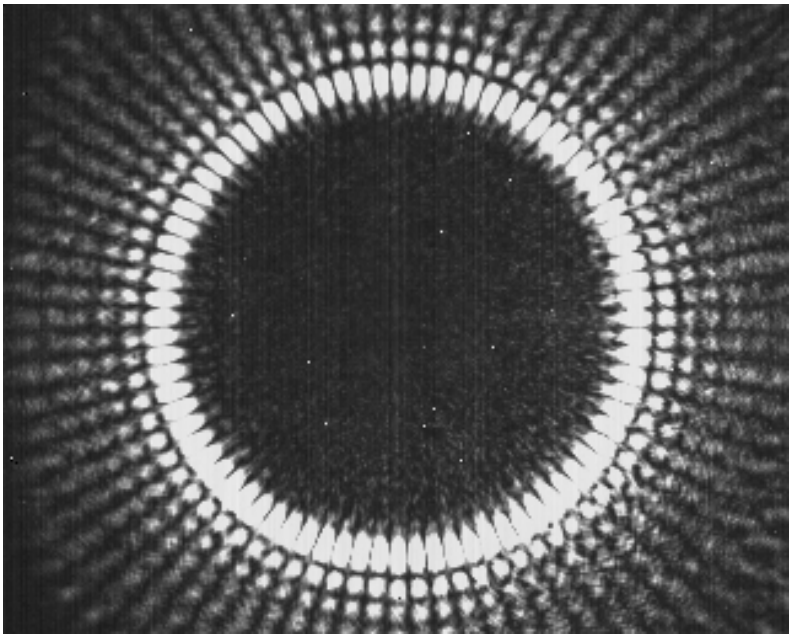

Figure 5.11: OAM of order $l = 40$

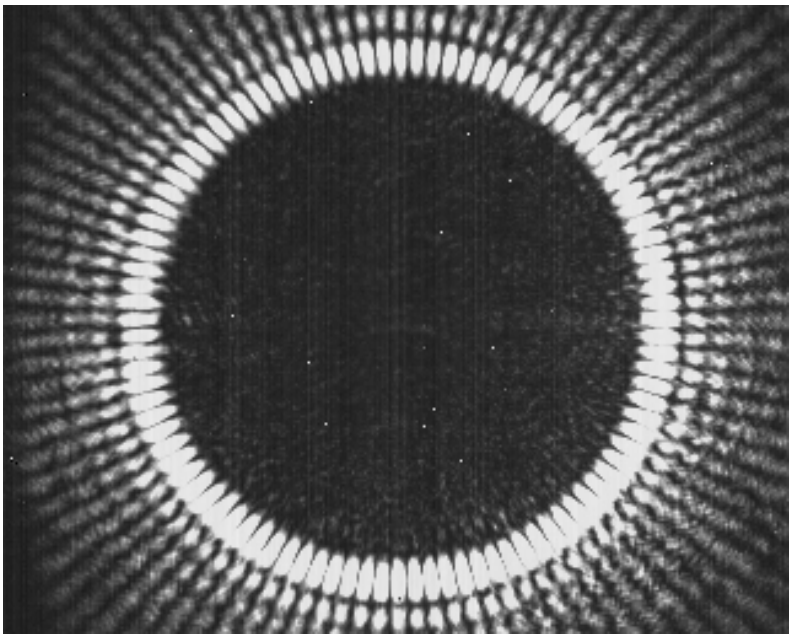

Figure 5.12: OAM of order $l = 50$

We can clearly see how increasing the order of the OAM increases the radio. In the table 5.1 we can see a comparison between the two cases that we are going to analyze, with and without beam expander:

OAM order	OAM radio (no b.e.)	OAM radio (b.e.)
$l = 10$	≈ 0.2 cm	≈ 0.3 cm
$l = 20$	≈ 0.25 cm	≈ 0.4 cm
$l = 30$	≈ 0.35 cm	≈ 0.5 cm
$l = 40$	≈ 0.4 cm	≈ 0.6 cm
$l = 50$	≈ 0.5 cm	≈ 0.7 cm

Table 5.1: Comparison between orders and radios for an OAM

5.2 Characterization of the OAM with P80 E28 surface

We will start the characterization of the setup depending on the rough surface with which the beam will be reflected. It is important to take into account the roughness of the surface, in this first analysis we will use the rougher surface P80 E28 (figure 5.13), and the angle with which it bounces, since this angle produces a frequency shift of scattered light similar to that obtained in the Doppler effect.

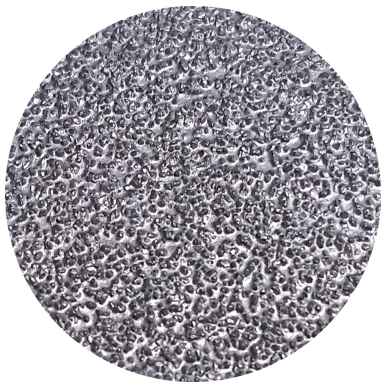

Figure 5.13: P80 E28 surface

5.2.1 Setup with beam expander

For this first phase of the characterization, we will keep the beam expander placed, which will make the ring that makes up the OAM have a considerable radius, as we have seen in the table 5.1. We intend to study whether this greater degree of freedom when we move the disk to the left and right, misaligning it with respect to the axis of rotation, will affect in power terms the peak of modulation that we have to observe. In addition to checking the displacement suffered by the modulation frequency as a function of the speed of rotation of the disk and other analyzes that will be detailed below.

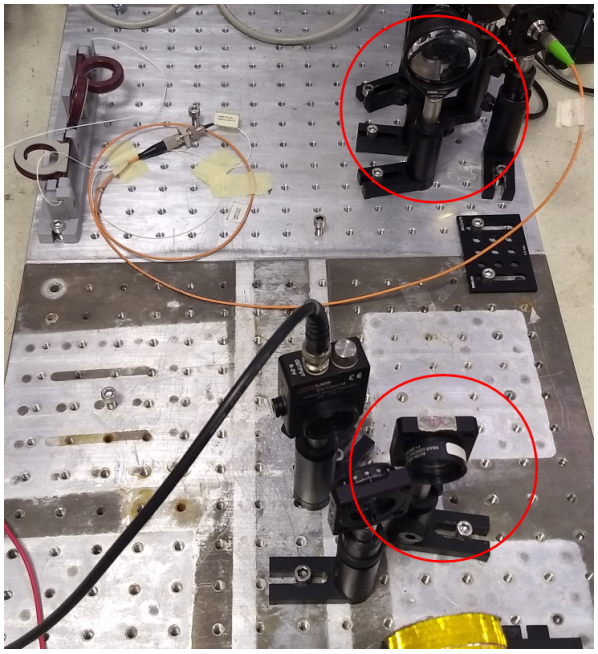

Figure 5.14: Setup with beam expanders

In function of the rotating disk displacement

Therefore, for this first analysis we will displace the surface in rotation to the left and right, misaligning the OAM with respect to the axis of rotation. For this we will use a regulator where the motor is located together with the disk and the rotation surface as we can see in the figure 5.15. The idea is to make jumps of 0.5 mm left and right with respect to the position where the OAM is centered with respect to the axis of rotation to check how this degree of freedom affects when it comes to identifying the modulation that should occur in the spectrum of frequencies observed. For this case, the speed will remain constant at 8.1 V, considering that at this voltage the vibrations do not affect the structure where the assembly is.

On the other hand, we must obtain the modulation frequency for a period of rotation and order of OAM. As we said before, the idea is to characterize the OAM for the orders $l = \pm 10,\ \pm 20,\ \pm 30,\ \pm 40$ and ± 50. During the characterization phase there were certain problems when working with the orders $l = \pm 40$ and ± 50 since the radius was too wide and we did not have margin of movement within the surface. In addition, we realized that the greater the radius, the more distributed the energy it carries, making it much more difficult to appreciate the frequency modulation we are looking for. In the same way, the smaller the radius, the more concentrated the energy is.

Figure 5.15: Regulator for disc displacement

Due to this, from now on, when we go to analyze the behavior regarding a displacement we will only do it for the orders $l = \pm 10,\ \pm 20,\ \pm 30$. Having explained the above considerations, we now calculate the modulation frequencies for each order.

- 1.- We must know the rotation period of our disk for a voltage $V = 8.1\ V$. For this, we adhere a piece of black adhesive tape to the frame of the disc, together with the oscilloscope and a beam we can measure the period. Measuring the period of rotation we obtain $T_{motor} = 45.18\ ms$. Together with the equation $\Omega = 2\pi\frac{1}{T}$, we obtain an angular velocity of $\Omega = 139.07\ rad/s$.

- 2.- Now we can apply the equation $f_{mod} = \Omega|l_1 - l_2|/2\pi$, to obtain the modulation frequency where the power peak generated by the overlap of both OAMs should be found and that manifests itself in this modulation in frequency. For the different OAM orders and angular velocity $\Omega = 139.07\ rad/s$, we obtain the following table:

OAM order	$f_{mod\ theor}$
$l = \pm 10$	442.67 Hz
$l = \pm 20$	885.34 Hz
$l = \pm 30$	1328 Hz

Table 5.2: Frequency modulation depending on OAM order

The table 5.2 indicates the theoretical position of where the frequency modulation is located in the spectrum, being a theoretical value it will help us to know where to start looking but it is possible that it is not exactly in that position.

- 3.- This measurement has been carried out with the OAM centered on the axis of rotation of the disk, whose initial position with the regulator has been 14 mm. Now what you have to do is move the disk in steps of 0.5 mm left and right and see how the peak of the modulation in frequency behaves.

The data collected in the table 5.3 show the displacement that we made on the beam with respect to the axis of rotation for different orders of OAM together with the theoretical modulation frequency and the obtained one of the spectrum, as well as the power that the OAM carries at the time of its measurement.

The figure 5.16 represents the power measurement obtained in the oscilloscope for the frequency modulations located in the spectrum with the help of the theoretical values. We observe the position 0 that refers to the initial position of the regulator at 14 mm. We have represented it in this way so that it is easier to see how much distance we are separating from the center, with -3 mm being the maximum level to the left and 3 mm the maximum level to the right.. We can observe a tendency characterized by the loss of energy when we move away from the axis of rotation, we also see that the maximum power that can be reached is greater the smaller the order of the OAM that we are characterizing. We assume that this is related to what we have said before, that the smaller the order of the OAM, the lower its radius and the more concentrated the energy will be.

	$l = \pm 10$			$l = \pm 20$			$l = \pm 30$		
Displacement	$f_{mod\ theor}$	f_{mod}	OAM Power	$f_{mod\ theor}$	f_{mod}	OAM Power	$f_{mod\ theor}$	f_{mod}	OAM Power
11 mm		445.6 Hz	-55.37 dBm		879 Hz	-52.66 dBm		1329 Hz	-57.31 dBm
11.5 mm		445.5 Hz	-54.31 dBm		885 Hz	-50.87 dBm		1320 Hz	-55.4 dBm
12 mm		445.6 Hz	-51.98 dBm		889.5 Hz	-50.08 dBm		1316 Hz	-56.52 dBm
12.5 mm		450.2 Hz	-55.08 dBm		889.6 Hz	-48.97 dBm		1336 Hz	-54.63 dBm
13 mm		451.7 Hz	-50.47 dBm		887.4 Hz	-47.98 dBm		1333 Hz	-51.82 dBm
13.5 mm		451.7 Hz	-44.92 dBm		887.4 Hz	-44.33 dBm		1333 Hz	-55.64 dBm
14 mm	442.67 Hz	448.6 Hz	-43.72 dBm	885.34 Hz	882 Hz	-50.02 dBm	1328 Hz	1339 Hz	-48.73 dBm
14.5 mm		451.7 Hz	-48.15 dBm		880.5 Hz	-48.16 dBm		1313 Hz	-49.34 dBm
15 mm		451.6 Hz	-53.82 dBm		888.2 Hz	-50.97 dBm		1317 Hz	-53.49 dBm
15.5 mm		450 Hz	-58.01 dBm		892.6 Hz	-52.14 dBm		1327 Hz	-56.66 dBm
16 mm		448.6 Hz	-51.83 dBm		892.8 Hz	-54.65 dBm		1326 Hz	-59.02 dBm
16.5 mm		454.8 Hz	-57.1 dBm		892.6 Hz	-52.08 dBm		1323 Hz	-57.68 dBm
17 mm		450 Hz	-55.23 dBm		894.2 Hz	-57.74 dBm		1323 Hz	-59.48 dBm

Table 5.3: OAM peak power in function of the disc displacement with beam expander (P80 E28 surface)

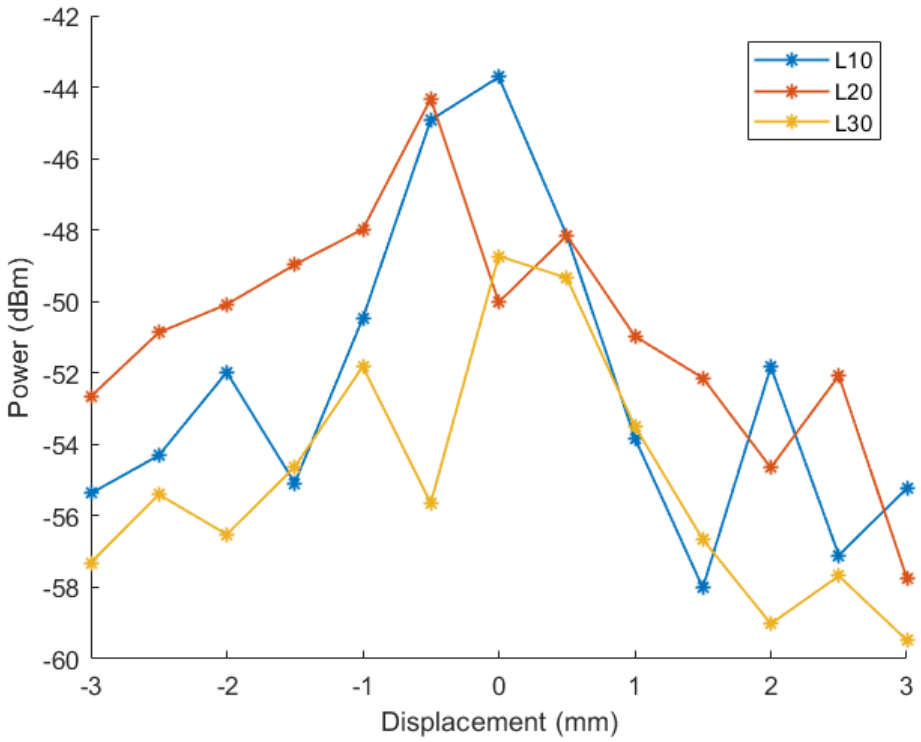

Figure 5.16: OAM power for different displacements with beam expander (P80 E28 surface)

In function of the speed of the disk

Now we are going to characterize the OAM according to the speed of the disk with which the beam impacts. The modulation frequency undergoes a frequency shift when the rotational speed of the receiver change. For this characterization we are going to change the speed of rotation of the surface, increasing the power received by the motor so that we can compare the theoretical results from the equation $f_{mod} = \Omega|l_1 - l_2|/2\pi$ with the obtained in the oscilloscope applying the FFT.

- 1.- As we did before, we must know the period of rotation of our surface. In this case we have four different voltages that are used to perform the characterization being $V = 8.1\ V, 9\ V, 10\ V$ and $11\ V$. We consider evaluating up to $11\ V$ since at this point the vibrations begin to be a problem for the setup. With these voltages, the angular velocities obtained are:

Voltage	Ω
$V = 8.1$ V	$\Omega = 139.07$ rad/s
$V = 9$ V	$\Omega = 160.69$ rad/s
$V = 10$ V	$\Omega = 185.94$ rad/s
$V = 11$ V	$\Omega = 197.02$ rad/s

Table 5.4: Angular speed for different voltages.

- 2.- Now, leaving the beam centered on the axis of rotation, we must find the corresponding modulation frequency for each order of OAM and for each of the angular frequencies. Therefore we have to apply the equation $f_{mod} = \Omega|l_1 - l_2|/2\pi$ to obtain the theoretical position of where the highest power peak is located.
- 3.- We will make a comparison between the theoretical position and where the frequency of modulation is really to see if the model is correct. These same steps will be performed when we want to characterize based on the speed of the disk.

In the tables 5.5-5.8 the theoretical modulation frequencies are represented along with those obtained during the measurements for each of the OAM orders at different voltages.

From the results obtained, in the graph 5.17 we can see the comparison between the theoretical curve of displacement in frequency and that obtained in the measurements. After representing both we can affirm that the measurements taken are very close to the theoretical values, being the difference between them of the order of hertz. It is then verified that the frequency of modulation is closely related to the speed of rotation of the receiver with which we make the beam impact, producing a shift in frequency when the speed varies.

From the graph 5.18 we can observe, as it happened in the previous characterization, that the power reached by the modulation in frequency is greater the smaller the order of OAM that we are analyzing. We also see a slight tendency of the power that decreases when we increase the speed of rotation of the disc, this could be due to the fact that it increases the dispersion during reflection, causing a part of the energy to be dispersed in a greater number of directions, causing the power that affects the photodiode is lower.

$V = 8.1\ V\ (\Omega = 139.07\ rad/s)$									
$l = \pm 10$		$l = \pm 20$		$l = \pm 30$		$l = \pm 40$		$l = \pm 50$	
$f_{mod\ theor}$	f_{mod}	$f_{mod\ theor}$	f_{mod}	$f_{mod\ theor}$	f_{mod}	$f_{mod\ theor}$	f_{mod}	$f_{mod\ theor}$	f_{mod}
442.67 Hz	451.7 Hz	885.34 Hz	898.8 Hz	1328 Hz	1316.8 Hz	1770 Hz	1759.5 Hz	2213 Hz	2200 Hz

Table 5.5: Theoretical frequency modulation and frequency modulation peak for different OAM orders and $V = 8.1\ V$

$V = 9\ V\ (\Omega = 160.69\ rad/s)$									
$l = \pm 10$		$l = \pm 20$		$l = \pm 30$		$l = \pm 40$		$l = \pm 50$	
$f_{mod\ theor}$	f_{mod}	$f_{mod\ theor}$	f_{mod}	$f_{mod\ theor}$	f_{mod}	$f_{mod\ theor}$	f_{mod}	$f_{mod\ theor}$	f_{mod}
511.49 Hz	506.6 Hz	1022.98 Hz	1016 Hz	1534.47 Hz	1533 Hz	2045.96 Hz	2066 Hz	2557.46 Hz	2544 Hz

Table 5.6: Theoretical frequency modulation and frequency modulation peak for different OAM orders and $V = 9\ V$

$V = 10\ V\ (\Omega = 185.94\ rad/s)$									
$l = \pm 10$		$l = \pm 20$		$l = \pm 30$		$l = \pm 40$		$l = \pm 50$	
$f_{mod\ theor}$	f_{mod}	$f_{mod\ theor}$	f_{mod}	$f_{mod\ theor}$	f_{mod}	$f_{mod\ theor}$	f_{mod}	$f_{mod\ theor}$	f_{mod}
591.86 Hz	584.4 Hz	1183.73 Hz	1167.5 Hz	1775.6 Hz	1779 Hz	2367.46 Hz	2359 Hz	2959 Hz	2967.9 Hz

Table 5.7: Theoretical frequency modulation and frequency modulation peak for different OAM orders and $V = 10\ V$

$V = 11\ V\ (\Omega = 197.02\ rad/s)$									
$l = \pm 10$		$l = \pm 20$		$l = \pm 30$		$l = \pm 40$		$l = \pm 50$	
$f_{mod\ theor}$	f_{mod}	$f_{mod\ theor}$	f_{mod}	$f_{mod\ theor}$	f_{mod}	$f_{mod\ theor}$	f_{mod}	$f_{mod\ theor}$	f_{mod}
627.13 Hz	633.2 Hz	1254.26 Hz	1268 Hz	1881.40 Hz	1875.2 Hz	2508.53 Hz	2484.2 Hz	3135.67 Hz	3135.7 Hz

Table 5.8: Theoretical frequency modulation and frequency modulation peak for different OAM orders and $V = 11\ V$

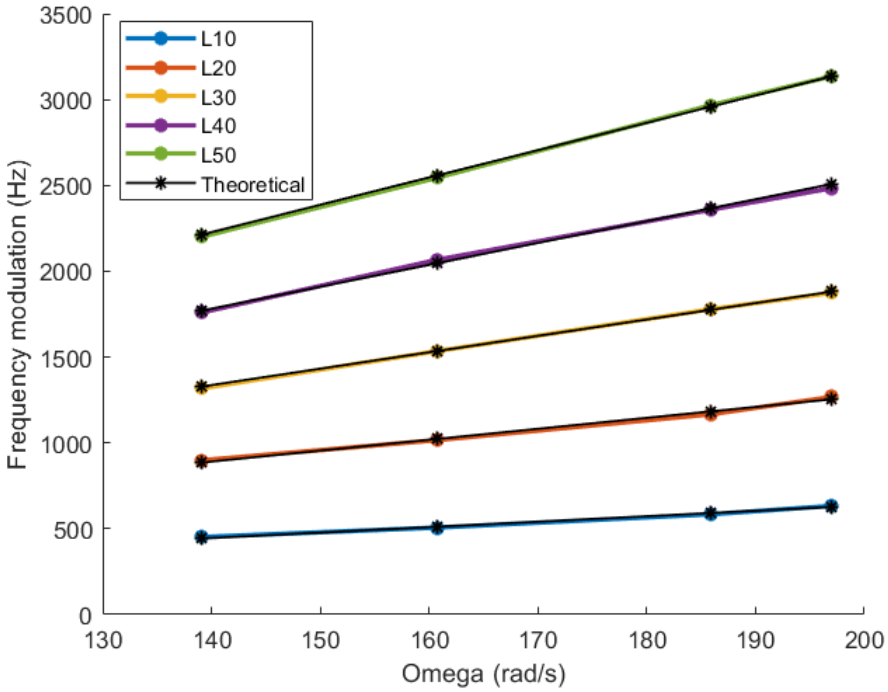

Figure 5.17: Angular velocity in function of frequency modulation with beam expander (P80 E28 surface)

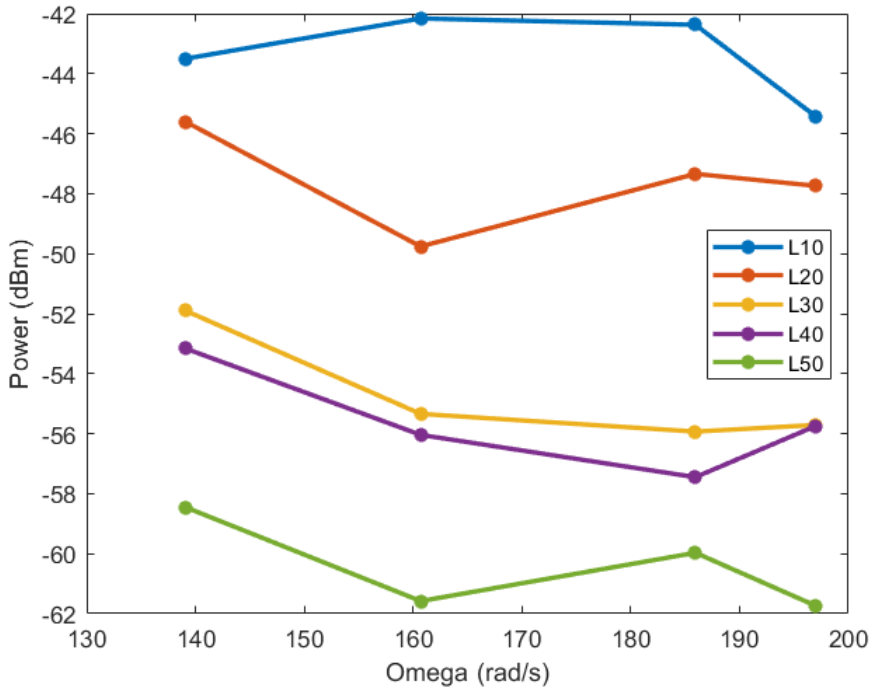

Figure 5.18: Angular velocity in function of OAM power with beam expander (P80 E28 surface)

Signal-to-Noise Ratio for differents OAM

Now let's check the signal-to-noise level for each OAM order. For this we have measured the noise level, located at each modulation frequency for each of the OAM orders that we have. On the other hand, we have made the same measurements, now, injecting the beam with the different OAM orders.

In the tables 5.9-5.13 are represented the noise levels, together with the power peaks belonging to each OAM order and the difference between them that gives us the signal-to-noise level that each order carries OAM.

In the figure 5.19 we observe the spectrum of noise captured by the photodiode, while in the figure 5.20 we see the spectrum when it carries an OAM. The low frequencies are predominant in terms of power with respect to the rest of the spectrum, this is important to take into consideration when we want to identify an order that is within this range of the spectrum.

$l = \pm 10$				
Voltage	Angular velocity	OAM Power	Noise level	SNR
8.1 V	139.07 rad/s	-43.50 dBm	-62.55 dBm	19.05 dB
9 V	160.69 rad/s	-42.16 dBm	-66.56 dBm	24.4 dB
10 V	185.94 rad/s	-42.37 dBm	-65.38 dBm	23.01 dB
11 V	197.02 rad/s	-45.43 dBm	-62.3 dBm	16.87 dB

Table 5.9: SNR for $l = 10$ with beam expander (P80 E28 surface)

$l = \pm 20$				
Voltage	Angular velocity	OAM Power	Noise level	SNR
8.1 V	139.07 rad/s	-45.6 dBm	-67.2 dBm	21.6 dB
9 V	160.69 rad/s	-49.76 dBm	-61.08 dBm	11.32 dB
10 V	185.94 rad/s	-47.34 dBm	-63.49 dBm	16.15 dB
11 V	197.02 rad/s	-47.74 dBm	-67.29 dBm	19.55 dB

Table 5.10: SNR for $l = 20$ with beam expander (P80 E28 surface)

$l = \pm 30$				
Voltage	Angular velocity	OAM Power	Noise level	SNR
8.1 V	139.07 rad/s	-51.9 dBm	-66.02 dBm	14.12 dB
9 V	160.69 rad/s	-55.34 dBm	-64.45 dBm	9.11 dB
10 V	185.94 rad/s	-55.93 dBm	-64.49 dBm	8.56 dB
11 V	197.02 rad/s	-55.71 dBm	-64.49 dBm	8.78 dB

Table 5.11: SNR for $l = 30$ with beam expander (P80 E28 surface)

$l = \pm 40$				
Voltage	Angular velocity	OAM Power	Noise level	SNR
8.1 V	139.07 rad/s	-53.16 dBm	-67.72 dBm	14.56 dB
9 V	160.69 rad/s	-56.04 dBm	-62.94 dBm	6.9 dB
10 V	185.94 rad/s	-57.45 dBm	-64.86 dBm	7.41 dB
11 V	197.02 rad/s	-55.74 dBm	-65.36 dBm	9.62 dB

Table 5.12: SNR for $l = 40$ with beam expander (P80 E28 surface)

$l = \pm 50$				
Voltage	Angular velocity	OAM Power	Noise level	SNR
8.1 V	139.07 rad/s	-58.45 dBm	-64.72 dBm	6.27 dB
9 V	160.69 rad/s	-61.58 dBm	-65.69 dBm	4.11 dB
10 V	185.94 rad/s	-59.97 dBm	-63.35 dBm	3.38 dB
11 V	197.02 rad/s	-61.74 dBm	-62.93 dBm	1.19 dB

Table 5.13: SNR for $l = 50$ with beam expander (P80 E28 surface)

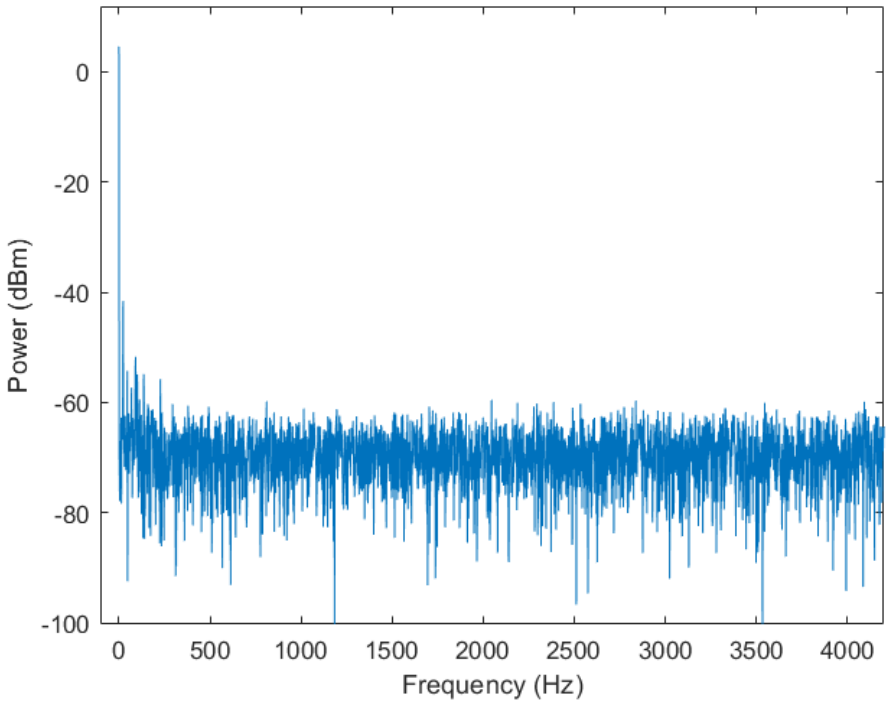

Figure 5.19: Noise level spectrum

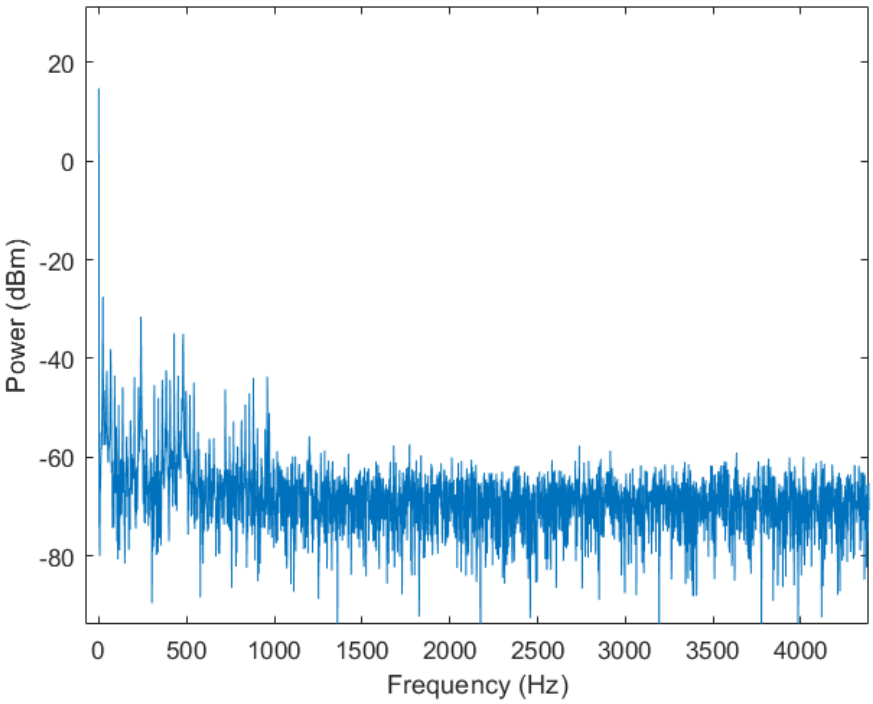

Figure 5.20: Noise level spectrum + OAM power

Representing in a graph this signal-to-noise level we obtain the figure 5.21, we see how the signal-to-noise level is greater the smaller the order is and, in general, it decreases slightly when we increase the speed of rotation of the disk with which we make the beam impact. This occurs mainly for two reasons: The first has already been mentioned before, by increasing the speed of rotation the beams are scattered in more random directions, causing less energy directed to the photodiode. The second one is that the power varies between different acquisitions taken by the oscilloscope, the power fluctuates in each moment of time so that sometimes it will be smaller and in others, higher. This makes it very difficult for us to perform measurements since there are times when there is no power peak belonging to an OAM order when there should be. It is a problem that we have had during the realization of the characterizations, because the photodiode does not always receive the reflection corresponding to the modulation in frequency that must be produced.

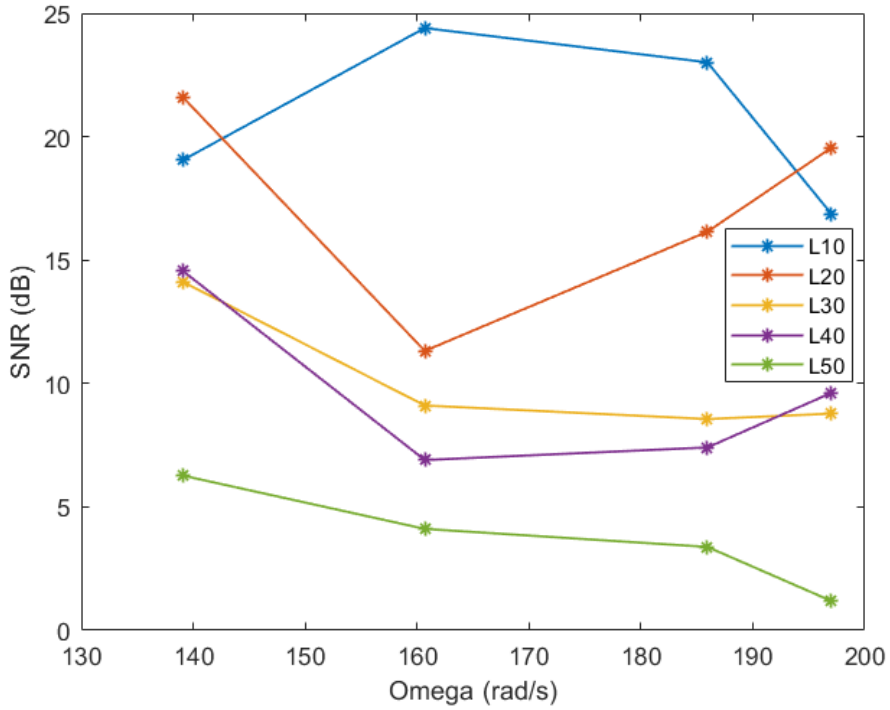

Figure 5.21: SNR with beam expander (P80 E28 surface)

5.2.2 Setup without beam expander

For this characterization we are going to eliminate the beam expander as shown in the figure 5.22, which will make the ring that forms the OAM have a smaller radius than before. We have to repeat the displacement measurements without the beam expanders, in addition to the other analyzes that depend on the speed of rotation of the disk and the OAM orders that we use. Now the radius of the OAM is lower so we have less freedom than the previous case, which forces us to decrease the number of steps we can move left and right to perform the characterization, although we will keep the 0.5 mm.

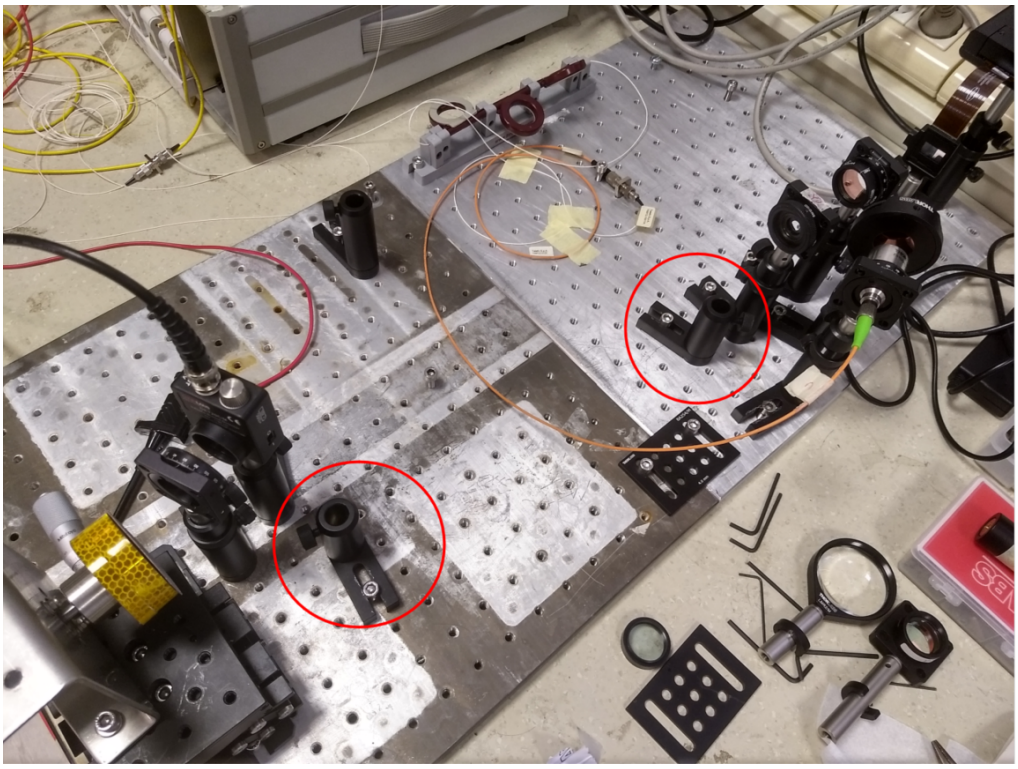

Figure 5.22: Setup without beam expanders

In function of the rotating disk displacement

As we explained in the case of characterization with the beam expander, the idea is to move with the regulator in steps of 0.5 mm left and right with respect to the initial position in which the OAM is centered on the axis of rotation. It will also maintain a constant speed of 8.1 V, where the vibrations do not affect almost anything to the setup.

The same considerations taken into account in the previous characterization with beam expander will continue to be here. We remember that there was a drawback when analyzing the modes $l = \pm 40$ and $l = \pm 50$ for issues such as little margin of movement or redistribution of power, making the analysis very difficult. In order to make a comparison

later the study will be carried out, in the same way as before, for the modes $l = \pm 10$, $l = \pm 20$ and $l = \pm 30$.

Therefore, having remembered the considerations that we must take into account, we analyze the behavior of the OAM with respect to displacement.

- 1.- We calculate the rotation period for a voltage of $V = 8.1\ V$ in the motor. Measuring the turning period we obtain $T_{motor} = 44.6\ ms$. Together with the equation $\Omega = 2\pi\frac{1}{T}$, we get an angular velocity of $\Omega = 140.87\ rad/s$.

- 2.- Now we can apply the equation $f_{mod} = \Omega|l_1 - l_2|/2\pi$, to obtain the modulation frequency where the power peak generated by the superposition of the two OAMs should be found and reflected in this frequency modulation. For different orders and angular velocity $\Omega = 140.87\ rad/s$, we obtain the following table:

OAM order	$f_{mod\ theor}$
$l = \pm 10$	448.40 Hz
$l = \pm 20$	896.80 Hz
$l = \pm 30$	1345.20 Hz

Table 5.14: Frequency modulation depending on OAM order

  The table 5.14 shows us the theoretical position of where the frequency modulation is located in the spectrum, being a theoretical value will help us to know where to start looking.

- 3.- This measurement has been carried out with the OAM centered on the axis of rotation of the disk, whose initial position with the regulator has been 13.5 mm. Now what you have to do is move the disk in steps of 0.5 mm to left and right and see how the peak of the modulation behaves in frequency.

The data collected in the tables 5.15-5.17 show the displacement that we made on the beam with respect to the axis of rotation for different orders of OAM together with the frequency of theoretical modulation and the one obtained from the spectrum, as well as the power that the OAM carries at the moment of its measurement.

$l = \pm 10$			
Displacement	$f_{mod\ theor}$	f_{mod}	OAM Power
12 mm		450.2 Hz	-47.98 dBm
12.5 mm		450.2 Hz	-49.02 dBm
13 mm		447.1 Hz	-38.3 dBm
13.5 mm	448.40 Hz	451.7 Hz	-37.23 dBm
14 mm		451.7 Hz	-33.94 dBm
14.5 mm		442.5 Hz	-46.76 dBm
15 mm		448.5 Hz	-50.79 dBm

Table 5.15: OAM peak power in function of the disc displacement $l = 10$

$l = \pm 20$			
Displacement	$f_{mod\ theor}$	f_{mod}	OAM Power
12 mm		900 Hz	-57.31 dBm
12.5 mm		888 Hz	-54.9 dBm
13 mm		897.2 Hz	-53.71 dBm
13.5 mm	896.80 Hz	889.6 Hz	-52.04 dBm
14 mm		892.6 Hz	-54.46 dBm
14.5 mm		900.3 Hz	-56.39 dBm
15 mm		896 Hz	-57.97 dBm

Table 5.16: OAM peak power in function of the disc displacement $l = 20$

$l = \pm 30$			
Displacement	$f_{mod\ theor}$	f_{mod}	OAM Power
12 mm		1361 Hz	-60.61 dBm
12.5 mm		1347.4 Hz	-59.32 dBm
13 mm		1373.2 Hz	-53.56 dBm
13.5 mm	1345.20 Hz	1345.8 Hz	-55.68 dBm
14 mm		1338.2 Hz	-57.33 dBm
14.5 mm		1350.4 Hz	-58.59 dBm
15 mm		1361 Hz	-60.3 dBm

Table 5.17: OAM peak power in function of the disc displacement $l = 30$

The figure 5.23 represents the power measurement obtained in the oscilloscope for the frequency modulations located in the spectrum with the help of the theoretical values. As we did in the previous characterization with beam expander, we observe the position 0 that makes reference to the initial position of the regulator in 13.5 mm. The fact that the position has changed with respect to the previous one is due to the fact that, between analysis, there are moments in which we change lenses slightly of position, or we lose the alignment in the setup, so we must make small adjustments regarding the position in the that the disk is located to align the assembly.

Now, the distance that we can move the OAM has been reduced since the radius is smaller and it will decentralize much faster with respect to the center of rotation when we move it. The maximum distance we have considered is -1.5 mm for the maximum bound to the left and 1.5 mm As happened before, when the OAM is centered with respect to the axis of rotation is when more energy is transmitted, losing when we move laterally.

In this case we can also observe a tendency characterized by the loss of energy when we move away from the axis of rotation, we also see that the maximum power that can be reached is greater the smaller the order of the OAM that we are characterizing.

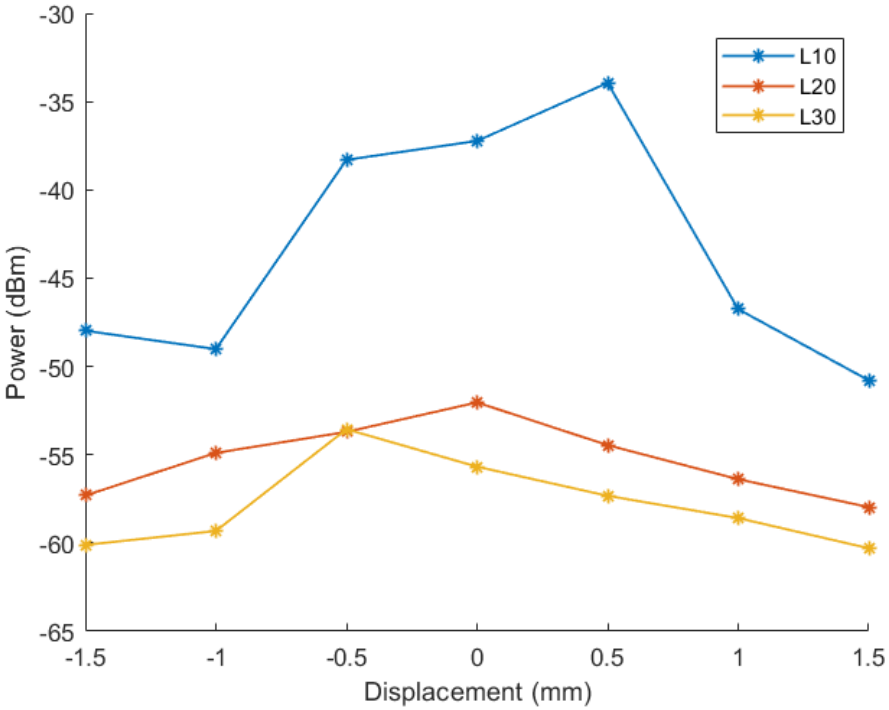

Figure 5.23: OAM power for different displacements without beam expander (P80 E28 surface)

In function of the speed of the disk

Again, we go on to characterize the OAM according to the speed of the disc. We will change the speed of rotation of the surface increasing the power received by the motor so that we can compare the theoretical results from the equation $f_{mod} = \Omega|l_1 - l_2|/2\pi$ with the obtained in the oscilloscope applying the FFT.

- 1.- We calculate the rotation period for the four voltages used to perform the characterization being $V = 8.1\ V, 9\ V, 10\ V$ and $11\ V$. En $V = 11\ V$ we must stop because the vibrations begin to affect the assembly. In the table 5.18 we show the angular velocities obtained from the disk rotation period for each voltage.

Voltage	Ω
$V = 8.1$ V	$\Omega = 140.87$ rad/s
$V = 9$ V	$\Omega = 160.69$ rad/s
$V = 10$ V	$\Omega = 183.02$ rad/s
$V = 11$ V	$\Omega = 197.08$ rad/s

Table 5.18: Angular speed for different voltages.

- 2.- We went on to calculate the theoretical position where we should find the corresponding frequency modulations for each OAM order and for each of the angular frequencies. As before, we apply the equation $f_{mod} = \Omega|l_1 - l_2|/2\pi$ to obtain the position of the peak with the highest power.

- 3.- To finish we make the comparison between the theoretical position and the one obtained in the analysis with other measurements.

In the tables 5.19-5.22 the theoretical modulation frequencies are represented along with those obtained during the measurements for each of the OAM orders at different voltages.

From the results obtained, in the graph 5.24 we can see the comparison between the theoretical curve of displacement in frequency and that obtained in the measurements. As it happened in the characterization with beam expander, the positions where the modulations are found in frequency are very similar to those obtained in a theoretical way, being the margin of error of some hertz. The results obtained are those expected taking into account that the displacement in frequency is linked to the angular velocity of the disk and not to the fact that the radius of the OAM is greater or less due to the beam expanders. Even so, it was of interest to obtain these data to corroborate those obtained in the previous characterization. On the other hand, for the graph 5.25, this time we see that the tendency that existed in the power when we increase the speed of rotation of the disk, is not as influential as before.

$V = 8.1\ V\ (\Omega = 140.87\ rad/s)$									
$l = \pm 10$		$l = \pm 20$		$l = \pm 30$		$l = \pm 40$		$l = \pm 50$	
$f_{mod\ theor}$	f_{mod}	$f_{mod\ theor}$	f_{mod}	$f_{mod\ theor}$	f_{mod}	$f_{mod\ theor}$	f_{mod}	$f_{mod\ theor}$	f_{mod}
448.4 Hz	451.7 Hz	896.8 Hz	897.2 Hz	1345.2 Hz	1350 Hz	1793.61 Hz	1794 Hz	2242 Hz	2246 Hz

Table 5.19: Theoretical frequency modulation and frequency modulation peak for different OAM orders and $V = 8.1\ V$

$V = 9\ V\ (\Omega = 160.69\ rad/s)$									
$l = \pm 10$		$l = \pm 20$		$l = \pm 30$		$l = \pm 40$		$l = \pm 50$	
$f_{mod\ theor}$	f_{mod}	$f_{mod\ theor}$	f_{mod}	$f_{mod\ theor}$	f_{mod}	$f_{mod\ theor}$	f_{mod}	$f_{mod\ theor}$	f_{mod}
511.49 Hz	505.1 Hz	1022.98 Hz	1012 Hz	1534.47 Hz	1535 Hz	2045.96 Hz	2029 Hz	2557 Hz	2563 Hz

Table 5.20: Theoretical frequency modulation and frequency modulation peak for different OAM orders and $V = 9\ V$

$V = 10\ V\ (\Omega = 183.02\ rad/s)$									
$l = \pm 10$		$l = \pm 20$		$l = \pm 30$		$l = \pm 40$		$l = \pm 50$	
$f_{mod\ theor}$	f_{mod}	$f_{mod\ theor}$	f_{mod}	$f_{mod\ theor}$	f_{mod}	$f_{mod\ theor}$	f_{mod}	$f_{mod\ theor}$	f_{mod}
582.57 Hz	579.8 Hz	1165 Hz	1163 Hz	1747.71 Hz	1746 Hz	2330.28 Hz	2332 Hz	2912.85 Hz	2913 Hz

Table 5.21: Theoretical frequency modulation and frequency modulation peak for different OAM orders and $V = 10\ V$

$V = 11\ V\ (\Omega = 197.08\ rad/s)$									
$l = \pm 10$		$l = \pm 20$		$l = \pm 30$		$l = \pm 40$		$l = \pm 50$	
$f_{mod\ theor}$	f_{mod}	$f_{mod\ theor}$	f_{mod}	$f_{mod\ theor}$	f_{mod}	$f_{mod\ theor}$	f_{mod}	$f_{mod\ theor}$	f_{mod}
627.32 Hz	640.9 Hz	1254.65 Hz	1245 Hz	1881.97 Hz	1888 Hz	2509.3 Hz	2504 Hz	3136.62 Hz	3139 Hz

Table 5.22: Theoretical frequency modulation and frequency modulation peak for different OAM orders and $V = 11\ V$

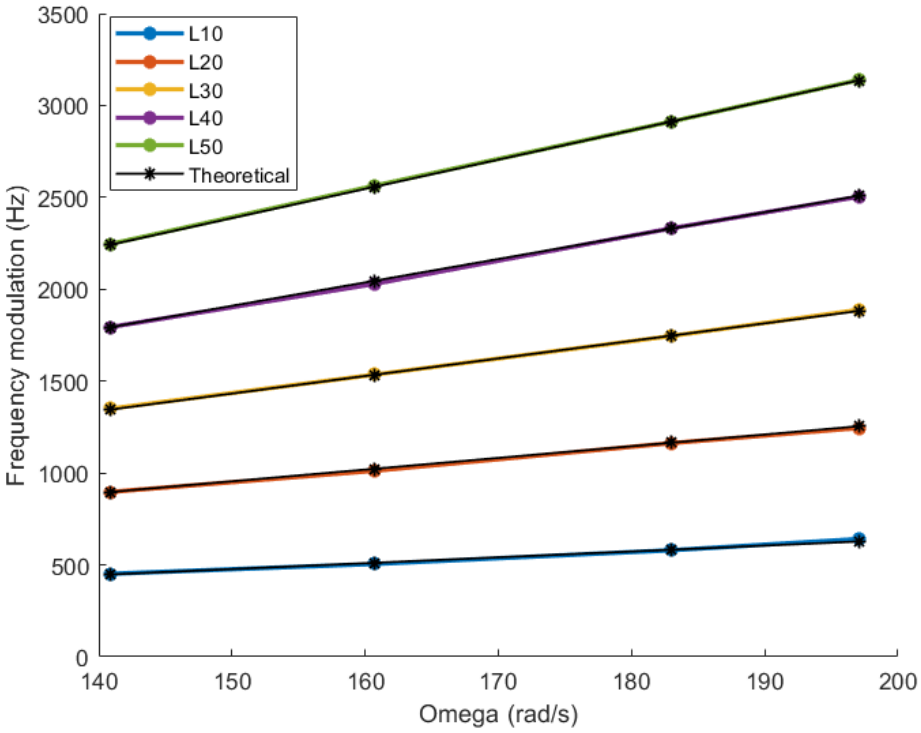

Figure 5.24: Angular velocity in function of frequency modulation without beam expander (P80 E28 surface)

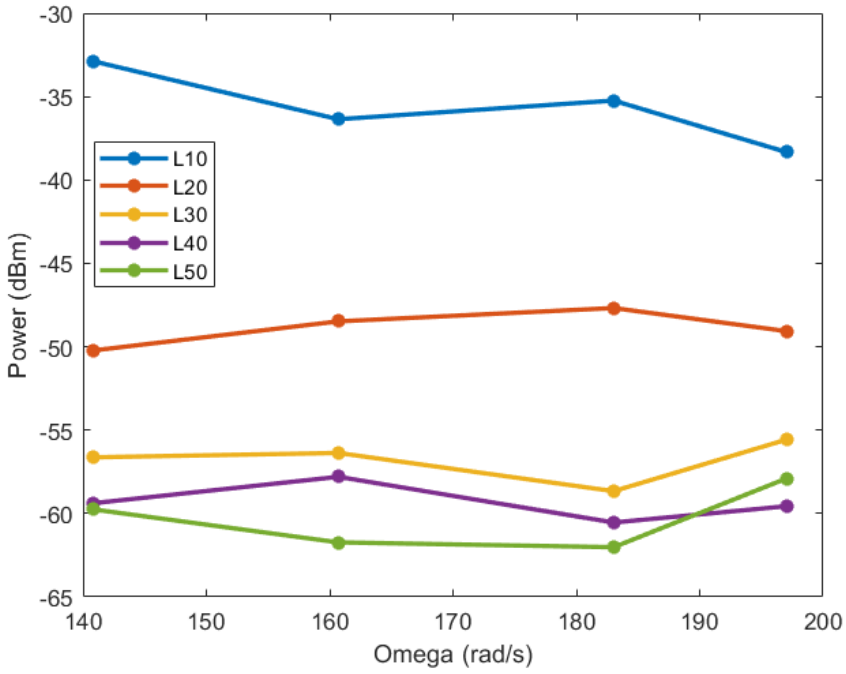

Figure 5.25: Angular velocity in function of OAM power without beam expander (P80 E28 surface)

Signal-to-Noise Ratio for differents OAM

As before, we will check the signal-to-noise level for each OAM. Therefore, we will measure the power level of the noise level and then injecting the beams with the different OAM modes. In the tables 5.23-5.27 are represented the noise levels, together with the peaks of power belonging to each OAM order and the difference between them that gives us the signal-to-noise level of each OAM order . On this occasion and onwards we will not graphically represent the noise levels since it is always maintained at the same power levels.

$l = \pm 10$				
Voltage	Angular velocity	OAM Power	Noise level	SNR
8.1 V	140.87 rad/s	-32.89 dBm	-65.87 dBm	32.98 dB
9 V	160.69 rad/s	-36.86 dBm	-62.18 dBm	25.32 dB
10 V	183.02 rad/s	-35.24 dBm	-60.85 dBm	25.61 dB
11 V	197.08 rad/s	-38.54 dBm	-61.44 dBm	23.1 dB

Table 5.23: SNR for $l = 10$ without beam expander (P80 E28 surface)

$l = \pm 20$				
Voltage	Angular velocity	OAM Power	Noise level	SNR
8.1 V	140.87 rad/s	-50.22 dBm	-61.6 dBm	11.38 dB
9 V	160.69 rad/s	-48.48 dBm	-61.47 dBm	12.99 dB
10 V	183.02 rad/s	-47.68 dBm	-65.43 dBm	17.75 dB
11 V	197.08 rad/s	-49.07 dBm	-67.21 dBm	18.14 dB

Table 5.24: SNR for $l = 20$ without beam expander (P80 E28 surface)

$l = \pm 30$				
Voltage	Angular velocity	OAM Power	Noise level	SNR
8.1 V	140.87 rad/s	-56.63 dBm	-65.3 dBm	8.67 dB
9 V	160.69 rad/s	-56.37 dBm	-66.11 dBm	9.74 dB
10 V	183.02 rad/s	-58.66 dBm	-64.64 dBm	5.98 dB
11 V	197.08 rad/s	-55.56 dBm	-65.67 dBm	10.11 dB

Table 5.25: SNR for $l = 30$ without beam expander (P80 E28 surface)

$l = \pm 40$				
Voltage	Angular velocity	OAM Power	Noise level	SNR
8.1 V	140.87 rad/s	-59.38 dBm	-66.16 dBm	6.78 dB
9 V	160.69 rad/s	-57.8 dBm	-62.17 dBm	4.37 dB
10 V	183.02 rad/s	-60.54 dBm	-62.05 dBm	1.51 dB
11 V	197.08 rad/s	-59.56 dBm	-61.79 dBm	2.23 dB

Table 5.26: SNR for $l = 40$ without beam expander (P80 E28 surface)

$l = \pm 50$				
Voltage	Angular velocity	OAM Power	Noise level	SNR
8.1 V	140.87 rad/s	-59.76 dBm	-66.16 dBm	6.22 dB
9 V	160.69 rad/s	-61.73 dBm	-63.22 dBm	1.49 dB
10 V	183.02 rad/s	-62.02 dBm	-63.4 dBm	1.38 dB
11 V	197.08 rad/s	-57.89 dBm	-62.67 dBm	4.78 dB

Table 5.27: SNR for $l = 50$ without beam expander (P80 E28 surface)

Representing in a graph this difference of power levels we obtain the figure 5.26, in this occasion also, the signal to noise ratio is greater the smaller the order is and, in general, decreases slightly when we increase the speed of rotation of the disk with which we make the beam impact. As we explained earlier, the two main reasons why this happens are the rotation speed and the frequency of acquisition with which the samples are taken.

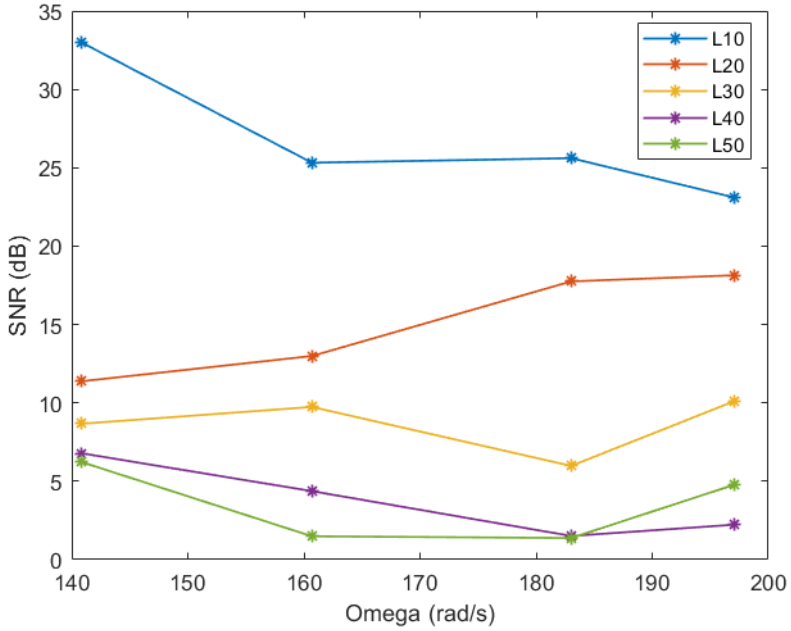

Figure 5.26: SNR without beam expander (P80 E28 surface)

5.3 Characterization of the OAM with P40 E28 surface

This time we are going to change the surface P80 E28, characterized by its roughness, by the P40 E28 (figure 5.27), which has a flatter surface and does not have so many irregularities. We will perform the same analyzes carried out previously to see if there are appreciable differences that could be of interest and that, therefore, would depend directly on the surface of the receiver with which we make the beam collide.

Figure 5.27: P40 E28 surface

5.3.1 Setup with beam expander

For this first phase of the characterization, we keep the beam expander placed, which will make the ring that makes up the OAM have a considerable radius. As before, this analysis aims to study how the displacement of the incident AMO affects when we move it. We must bear in mind that having a larger radius, we have a greater degree of freedom. We will also analyze how the variation in frequency or power affects the variation of other parameters such as the speed of rotation of the disk, the OAM order with which we are working, the misalignment with respect to the axis of rotation and other analyzes that we will expose next.

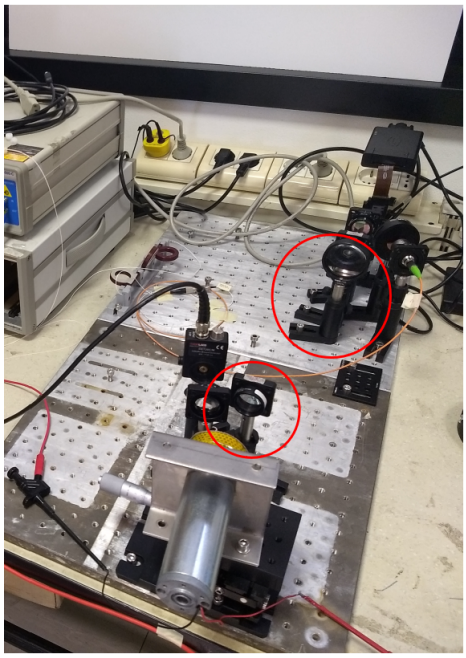

Figure 5.28: Setup with beam expanders

In function of the rotating disk displacement

For this first analysis we will move the surface in rotation to the left and right, misaligning the OAM with respect to the axis of rotation. We will use the regulator where the motor is placed together with the disk and the rotation surface. We will make steps of 0.5 mm left and right with respect to the position where OAM is centered to see how this affects when identifying the modulation that should occur in the observed frequency spectrum. We maintain a constant speed of 8.1 V, keeping the vibration level controlled.

We will characterize the OAM for the first three orders, not for the last two because of the inconveniences explained before. For this particular analysis the power is low for high orders, this added to the misalignment makes it extremely difficult to work with the orders $l = \pm 40$ and ± 50 since the radius is wide and the energy is very distributed .

- 1.- We calculate the rotation period of our disk for a voltage $V = 8.1\ V$ with the help of the oscilloscope. Measuring the period of rotation we obtain $T_{motor} = 44.4\ ms$. Together with the equation $\Omega = 2\pi\frac{1}{T}$, we obtain an angular velocity of $\Omega = 141.51\ rad/s$.

- 2.- We apply the equation $f_{mod} = \Omega|l_1 - l_2|/2\pi$ to obtain the modulation frequency where the power peak generated by the superposition of the two OAMs should be found. For the different orders and angular velocity $\Omega = 141.5\ rad/s$, we obtain the following table:

OAM order	$f_{mod\ theor}$
$l = \pm 10$	450.44 Hz
$l = \pm 20$	900.88 Hz
$l = \pm 30$	1351.32 Hz

Table 5.28: Frequency modulation depending on OAM order

Table 5.28 shows us the theoretical position of where the frequency modulation is located in the spectrum. It will serve as a reference to locate the approximate position of the modulation.

- 3.- This measurement has been carried out with the OAM centered on the axis of rotation of the disk, whose initial position with the regulator has been 15 mm. Now what you have to do is move the disk in steps of 0.5 mm to left and right and see how the peak of the modulation behaves in frequency.

The data collected in the table 5.29 show the displacement that we made on the beam with respect to the axis of rotation for different orders of OAM together with the frequency of theoretical modulation and the obtained one of the spectrum, as well as the power that takes the OAM at the time of its measurement.

The figure 5.29 represents the power measurement obtained in the oscilloscope for the frequency modulations located in the spectrum with the help of the theoretical values. The position 0 that refers to the initial position of the regulator at 15 mm. We have a movement distance of -3 mm to the left and 3 mm to the right. It is clearly observed the tendency of the energy to decrease when moving away from the center of rotation and how the energy is greater the smaller the order we are measuring.

	$l = \pm 10$			$l = \pm 20$			$l = \pm 30$		
Displacement	$f_{mod\ theor}$	f_{mod}	OAM Power	$f_{mod\ theor}$	f_{mod}	OAM Power	$f_{mod\ theor}$	f_{mod}	OAM Power
12 mm		459.4 Hz	-50.48 dBm		894.2 Hz	-58.86 dBm		1362 Hz	-57.97 dBm
12.5 mm		462.3 Hz	-53.97 dBm		900 Hz	-57.04 dBm		1358 Hz	-56.3 dBm
13 mm		451.7 Hz	-50.34 dBm		891 Hz	-56.38 dBm		1350 Hz	-59.49 dBm
13.5 mm		450.1 Hz	-51.31 dBm		886.6 Hz	-55.48 dBm		1342 Hz	-58.28 dBm
14 mm		453.2 Hz	-50.42 dBm		915.5 Hz	-54.24 dBm		1350 Hz	-54.9 dBm
14.5 mm		457.8 Hz	-41.92 dBm		880.4 Hz	-47.97 dBm		1355 Hz	-53.97 dBm
15 mm	450.44 Hz	459.3 Hz	-42.98 dBm	900.88 Hz	883.4 Hz	-44.05 dBm	1351.32 Hz	1330 Hz	-51.12 dBm
15.5 mm		459.3 Hz	-41.64 dBm		880.4 Hz	-49.72 dBm		1356 Hz	-52.01 dBm
16 mm		454.7 Hz	-50.77 dBm		885 Hz	-51.96 dBm		1350 Hz	-56.21 dBm
16.5 mm		456.2 Hz	-46.52 dBm		886.6 Hz	-51.8 dBm		1336 Hz	-55.42 dBm
17 mm		451.7 Hz	-51.79 dBm		880.4 Hz	-54.72 dBm		1365 Hz	-57.43 dBm
17.5 mm		442.5 Hz	-52.45 dBm		901.8 Hz	-55.51 dBm		1364 Hz	-57.39 dBm
18 mm		447 Hz	-55.31 dBm		900.4 Hz	-57.37 dBm		1345 Hz	-57.62 dBm

Table 5.29: OAM peak power in function of the disc displacement with beam expander (P40 E28 surface)

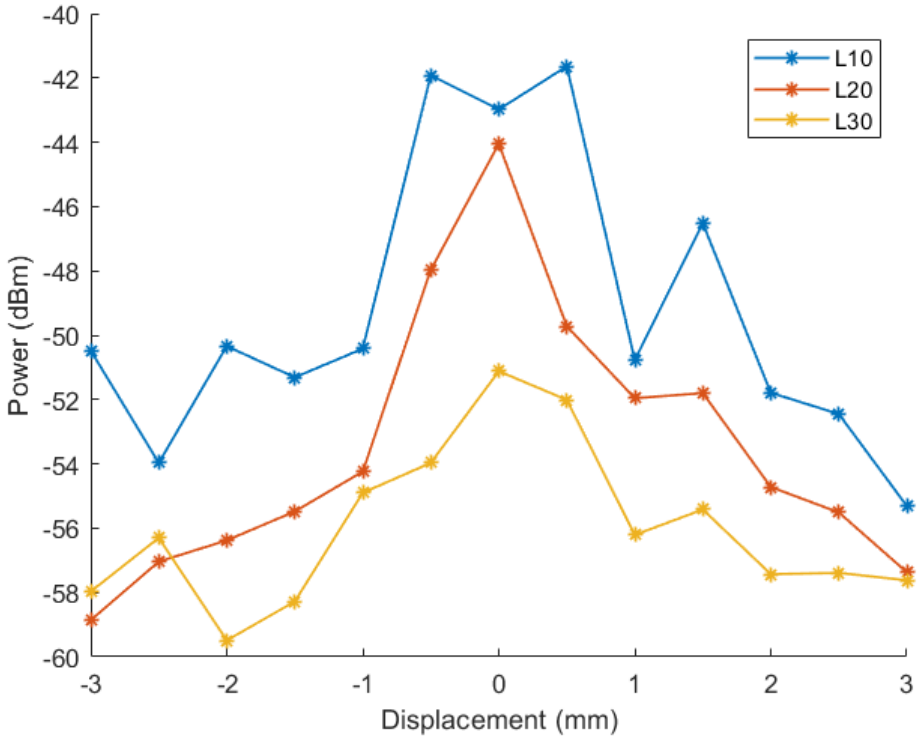

Figure 5.29: OAM power for different displacements with beam expander (P40 E28 surface)

In function of the speed of the disk

We analyze the OAM according to the speed of the disk with which the beam impacts. The modulation frequency undergoes a frequency shift when the rotational speed of the receiver is varied. For this characterization we are going to change the speed of rotation of the surface, increasing the power received by the motor so that we can compare the theoretical results from the equation $f_{mod} = \Omega|l_1 - l_2|/2\pi$ with those obtained in the oscilloscope applying the FFT.

- 1.- We calculate the rotation period of our disk. We perform the analysis for the four different voltages, which are the ones used to perform the characterization being $V = 8.1\ V, 9\ V, 10\ V, 11\ V$. We will not exceed $11\ V$ to avoid an excess of vibrations in the setup that could alter the results obtained. With these voltages, the angular velocities obtained are:

Voltage	Ω
$V = 8.1$ V	$\Omega = 141.51$ rad/s
$V = 9$ V	$\Omega = 161.52$ rad/s
$V = 10$ V	$\Omega = 183.71$ rad/s
$V = 11$ V	$\Omega = 194.52$ rad/s

Table 5.30: Angular speed for different voltages

- 2.- Leaving the beam centered on the axis of rotation, we find the corresponding modulation frequency for each OAM order and for each of the angular frequencies. We apply $f_{mod} = \Omega|l_1 - l_2|/2\pi$ to obtain the theoretical position of where the highest power peak is located.
- 3.- We compare the theoretical position and the original position of the modulation frequency to see if they match and verify that the model is correct.

In the tables 5.31-5.34 he theoretical modulation frequencies are represented along with those obtained during the measurements for each of the OAM orders at different voltages.

From the results obtained, in the graph 5.30 we can see the comparison between the theoretical curve of displacement in frequency and that obtained in the measurements. After representing both we can affirm that the measurements taken are very close to the theoretical values, being the difference between them of the order of hertz. As in the previous characterization, the frequency of modulation is closely related to the speed of rotation of the receiver with which we make the beam impinge, producing a shift in frequency when the speed varies.

From the graph 5.31 we can see that the orders $l = 10$ and $l = 50$ differ from the others notably but the orders $l = 20, /l = 30$ and $l = 40$ they move within a more defined interval between them. Even so, the existence of this tendency to decrease the energy captured by the photodiode continues when we increase the speed of rotation of the disk due to the greater randomness with which the beams are scattered.

$V = 8.1\ V\ (\Omega = 141.51\ rad/s)$									
$l = \pm 10$		$l = \pm 20$		$l = \pm 30$		$l = \pm 40$		$l = \pm 50$	
$f_{mod\ theor}$	f_{mod}	$f_{mod\ theor}$	f_{mod}	$f_{mod\ theor}$	f_{mod}	$f_{mod\ theor}$	f_{mod}	$f_{mod\ theor}$	f_{mod}
450.44 Hz	450.1 Hz	900.88 Hz	901.8 Hz	1351.32 Hz	1350 Hz	1801.76 Hz	1801 Hz	2252.20 Hz	2256 Hz

Table 5.31: Theoretical frequency modulation and frequency modulation peak for different OAM orders and $V = 8.1\ V$

$V = 9\ V\ (\Omega = 161.52\ rad/s)$									
$l = \pm 10$		$l = \pm 20$		$l = \pm 30$		$l = \pm 40$		$l = \pm 50$	
$f_{mod\ theor}$	f_{mod}	$f_{mod\ theor}$	f_{mod}	$f_{mod\ theor}$	f_{mod}	$f_{mod\ theor}$	f_{mod}	$f_{mod\ theor}$	f_{mod}
514.13 Hz	509.7 Hz	1028.26 Hz	1016 Hz	1542.40 Hz	1544.2 Hz	2056.53 Hz	2052 Hz	2570 Hz	2571 Hz

Table 5.32: Theoretical frequency modulation and frequency modulation peak for different OAM orders and $V = 9\ V$

$V = 10\ V\ (\Omega = 183.71\ rad/s)$									
$l = \pm 10$		$l = \pm 20$		$l = \pm 30$		$l = \pm 40$		$l = \pm 50$	
$f_{mod\ theor}$	f_{mod}	$f_{mod\ theor}$	f_{mod}	$f_{mod\ theor}$	f_{mod}	$f_{mod\ theor}$	f_{mod}	$f_{mod\ theor}$	f_{mod}
584.76 Hz	579.8 Hz	1169.53 Hz	1158 Hz	1754.30 Hz	1761 Hz	2339.06 Hz	2328 Hz	2923.83 Hz	2921 Hz

Table 5.33: Theoretical frequency modulation and frequency modulation peak for different OAM orders and $V = 10\ V$

$V = 11\ V\ (\Omega = 194.52\ rad/s)$									
$l = \pm 10$		$l = \pm 20$		$l = \pm 30$		$l = \pm 40$		$l = \pm 50$	
$f_{mod\ theor}$	f_{mod}	$f_{mod\ theor}$	f_{mod}	$f_{mod\ theor}$	f_{mod}	$f_{mod\ theor}$	f_{mod}	$f_{mod\ theor}$	f_{mod}
619.17 Hz	627 Hz	1238.35 Hz	1233 Hz	1857.52 Hz	1851 Hz	2476.70 Hz	2481 Hz	3095.88 Hz	3079 Hz

Table 5.34: Theoretical frequency modulation and frequency modulation peak for different OAM orders and $V = 11\ V$

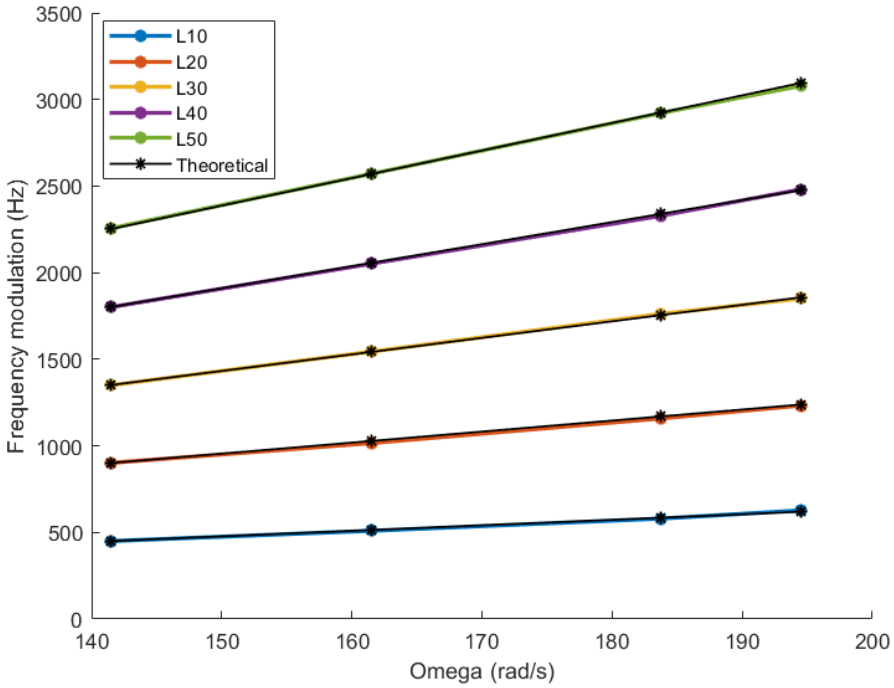

Figure 5.30: Angular velocity in function of frequency modulation with beam expander (P40 E28 surface)

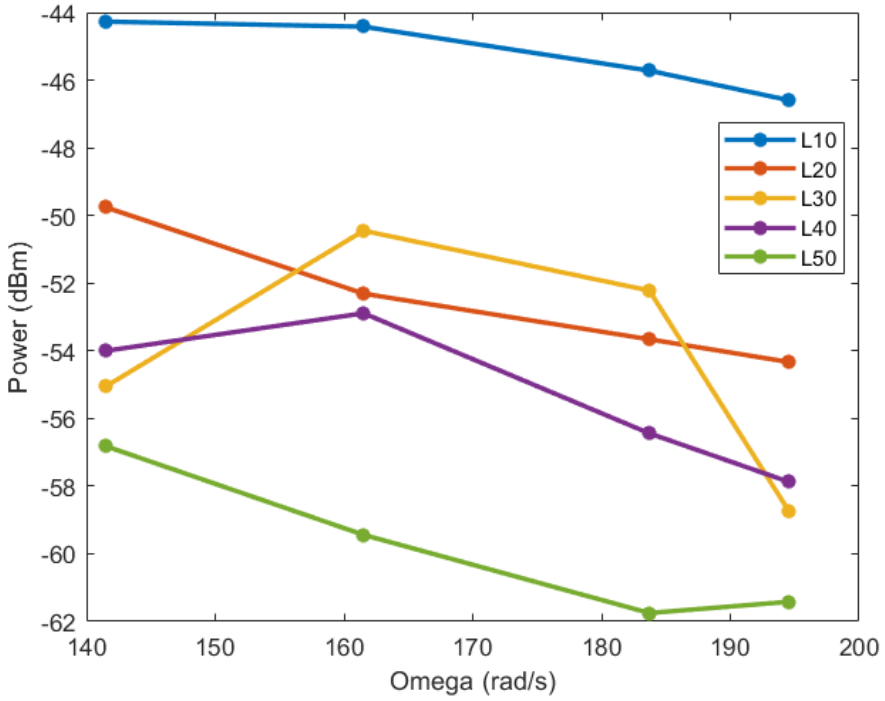

Figure 5.31: Angular velocity in function of OAM power with beam expander (P40 E28 surface)

Signal-to-Noise Ratio for differents OAM

We check the power of the noise level detected by the photodiode and we will make a difference with respect to the power that is added when an OAM is injected so that we can calculate the difference corresponding to the signal to noise ratio.

In the tables 5.35-5.39 are represented the noise levels, together with the peaks of power belonging to each OAM order and the difference between them that gives us the signal-to-noise level of each OAM order .

$l = \pm 10$				
Voltage	Angular velocity	OAM Power	Noise level	SNR
8.1 V	141.51 rad/s	-44.27 dBm	-65.47 dBm	21.2 dB
9 V	161.52 rad/s	-44.42 dBm	-64.23 dBm	19.81 dB
10 V	183.71 rad/s	-45.72 dBm	-66.95 dBm	21.23 dB
11 V	194.52 rad/s	-46.59 dBm	-61.19 dBm	14.60 dB

Table 5.35: SNR for $l = 10$ without beam expander (P40 E28 surface)

$l = \pm 20$				
Voltage	Angular velocity	OAM Power	Noise level	SNR
8.1 V	141.51 rad/s	-49.76 dBm	-64.25 dBm	14.49 dB
9 V	161.52 rad/s	-52.31 dBm	-63.78 dBm	11.47 dB
10 V	183.71 rad/s	-53.66 dBm	-65.73 dBm	12.07 dB
11 V	194.52 rad/s	-54.33 dBm	-66.05 dBm	11.72 dB

Table 5.36: SNR for $l = 20$ without beam expander (P40 E28 surface)

$l = \pm 30$				
Voltage	Angular velocity	OAM Power	Noise level	SNR
8.1 V	141.51 rad/s	-55.05 dBm	-66.21 dBm	11.16 dB
9 V	161.52 rad/s	-50.45 dBm	-67.3 dBm	16.85 dB
10 V	183.71 rad/s	-52.22 dBm	-63.01 dBm	10.79 dB
11 V	194.52 rad/s	-58.72 dBm	-62.68 dBm	3.96 dB

Table 5.37: SNR for $l = 30$ without beam expander (P40 E28 surface)

$l = \pm 40$				
Voltage	Angular velocity	OAM Power	Noise level	SNR
8.1 V	141.51 rad/s	-54 dBm	-65.84 dBm	11.84 dB
9 V	161.52 rad/s	-52.89 dBm	-63.78 dBm	10.89 dB
10 V	183.71 rad/s	-56.44 dBm	-65.42 dBm	8.98 dB
11 V	194.52 rad/s	-57.87 dBm	-65.32 dBm	7.45 dB

Table 5.38: SNR for $l = 40$ without beam expander (P40 E28 surface)

$l = \pm 50$				
Voltage	Angular velocity	OAM Power	Noise level	SNR
8.1 V	141.51 rad/s	-56.82 dBm	-62.32 dBm	5.5 dB
9 V	161.52 rad/s	-59.44 dBm	-62.4 dBm	2.96 dB
10 V	183.71 rad/s	-61.75 dBm	-62.51 dBm	0.76 dB
11 V	194.52 rad/s	-61.42 dBm	-64.97 dBm	3.55 dB

Table 5.39: SNR for $l = 50$ without beam expander (P40 E28 surface)

Representing in a graph this difference of power levels we obtain the figure 5.32, the signal-to-noise level is higher the smaller the order is and, in general, it decreases slightly when we increase the rotation speed of the disk with which we make the beam impact. The two main reasons why this occurs are the speed of rotation and the frequency of acquisition with which the samples are taken.

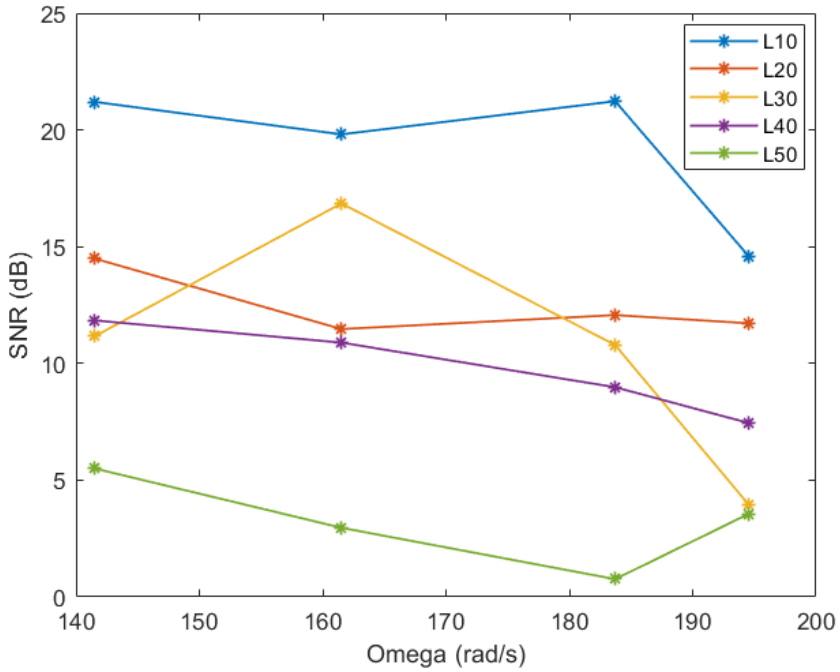

Figure 5.32: SNR with beam expander (P40 E28 surface)

5.3.2 Setup without beam expander

We removed the beam expanders from the laboratory assembly to perform the last characterization (figure 5.33) depending on the new surface. As we have already explained, by eliminating the beam expanders, the ring that forms the OAM has a smaller radius and the energy is more concentrated. When eliminating the beam expanders we are limiting the number of samples that we take in some of the analyzes but it is something we already assume with the previous characterization.

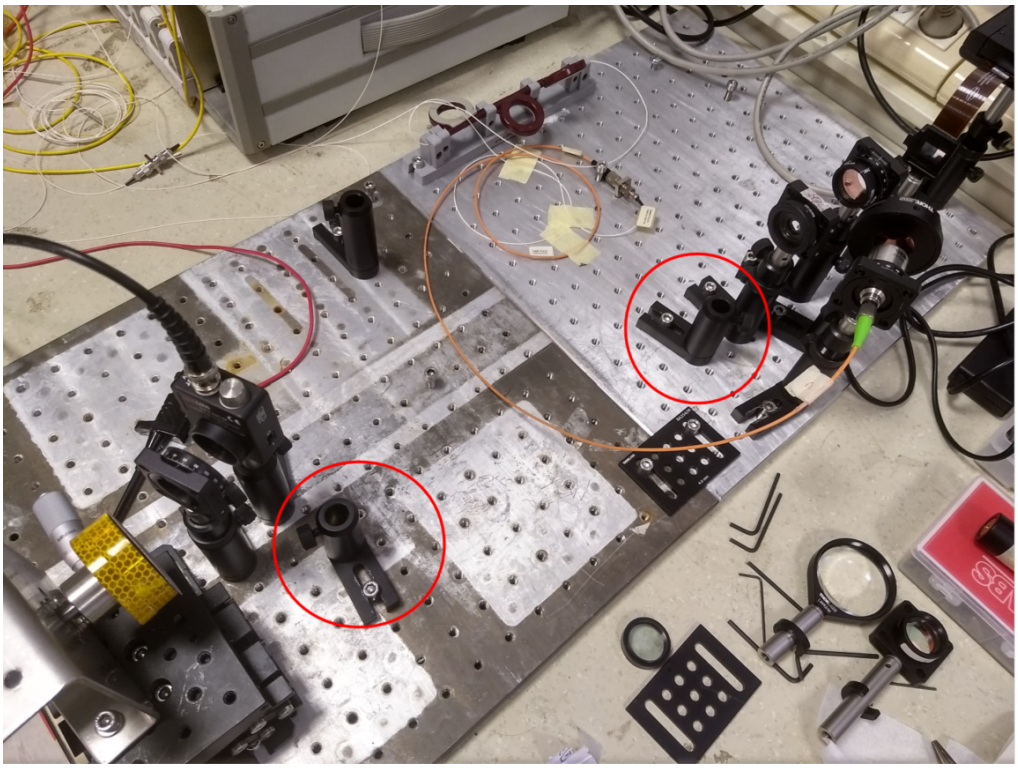

Figure 5.33: Setup without beam expanders

In function of the rotating disk displacement

As we have done, we will make a shift to the left and right with the help of the regulator to misalign the incident beam with respect to the axis of rotation of the disk. Steps of 0.5 mm will be made to study the behavior of the power in front of this new surface and considering that we have removed the beam expanders. The speed of rotation of the disk will keep it constant to perform this analysis. We will characterize the OAM for the first three orders.

- 1.- We calculate the rotation period of our disk for a voltage $V = 8.1\ V$ along with the help of the oscilloscope. Measuring the period of rotation we obtain $T_{motor} =$

44.4 ms. Together with the equation $\Omega = 2\pi\frac{1}{T}$, we obtain an angular velocity of $\Omega = 141.51\ rad/s$.

- 2.- We apply the equation $f_{mod} = \Omega|l_1 - l_2|/2\pi$ to obtain the modulation frequency where the power peak generated by the superposition of the two OAMs should be found. For the different orders and angular velocity $\Omega = 141.5\ rad/s$, we obtain the following table:

OAM order	$f_{mod\ theor}$
$l = \pm 10$	450.44 Hz
$l = \pm 20$	900.88 Hz
$l = \pm 30$	1351.32 Hz

Table 5.40: Frequency modulation depending on OAM order

The table 5.40 indicates the theoretical position of where the frequency modulation is located in the spectrum. It will serve as a reference to locate the approximate position of the modulation.

- 3.- This measurement has been carried out with the OAM centered on the axis of rotation of the disk, whose initial position with the regulator has been 15.5 mm. Now what you have to do is move the disk in steps of 0.5 mm to left and right and see how the peak of the modulation behaves in frequency.

The data collected in the tables 5.41-5.43 show the displacement that we made on the beam with respect to the axis of rotation for different orders of OAM together with the frequency of theoretical modulation and the one obtained from the spectrum, as well as the power that the OAM carries at the moment of its measurement.

$l = \pm 10$			
Displacement	$f_{mod\ theor}$	f_{mod}	OAM Power
14 mm		450 Hz	-45.32 dBm
14.5 mm		447 Hz	-43.18 dBm
15 mm		447 Hz	-42.31 dBm
15.5 mm	450.44 Hz	453.2 Hz	-42.58 dBm
16 mm		451.7 Hz	-45.66 dBm
16.5 mm		444 Hz	-44.76 dBm
17 mm		450 Hz	-48.66 dBm

Table 5.41: OAM peak power in function of the disc displacement $l = 10$

$l = \pm 20$			
Displacement	$f_{mod\ theor}$	f_{mod}	OAM Power
14 mm		903.4 Hz	-53.72 dBm
14.5 mm		904.8 Hz	-52.1 dBm
15 mm		898.8 Hz	-50.35 dBm
15.5 mm	900.88 Hz	898.8 Hz	-51.22 dBm
16 mm		903 Hz	-51.36 dBm
16.5 mm		900 Hz	-50.25 dBm
17 mm		898 Hz	-54.17 dBm

Table 5.42: OAM peak power in function of the disc displacement $l = 20$

$l = \pm 30$			
Displacement	$f_{mod\ theor}$	f_{mod}	OAM Power
14 mm		1341 Hz	-56.98 dBm
14.5 mm		1347 Hz	-58.45 dBm
15 mm		1348.9 Hz	-52.52 dBm
15.5 mm	1351.52 Hz	1359 Hz	-51.65 dBm
16 mm		1359 Hz	-51.72 dBm
16.5 mm		1350.4 Hz	-54.65 dBm
17 mm		1344 Hz	-57.92 dBm

Table 5.43: OAM peak power in function of the disc displacement $l = 30$

The figure 5.34 represents the power measurement obtained in the oscilloscope for the frequency modulations located in the spectrum with the help of the theoretical values. The position 0 refers the initial position of the regulator at 15.5 mm. As we explained, after an analysis we must check the alignment of the assembly so you have to make certain readjustments. Energy is greater for smaller orders, we observe a greater difference between $l = 10$ with the other two modes $l = 20$ and $l = 30$.

The distance that we can move the OAM has been reduced since the radius is smaller and it will decentralize much faster with respect to the center of rotation when we move it. The maximum distance we have considered is -1.5 mm for the maximum bound to the left and 1.5 mm the maximum bound to the right. As happened before, when the OAM is centered with respect to the axis of rotation is when more energy is transmitted, losing when we move laterally.

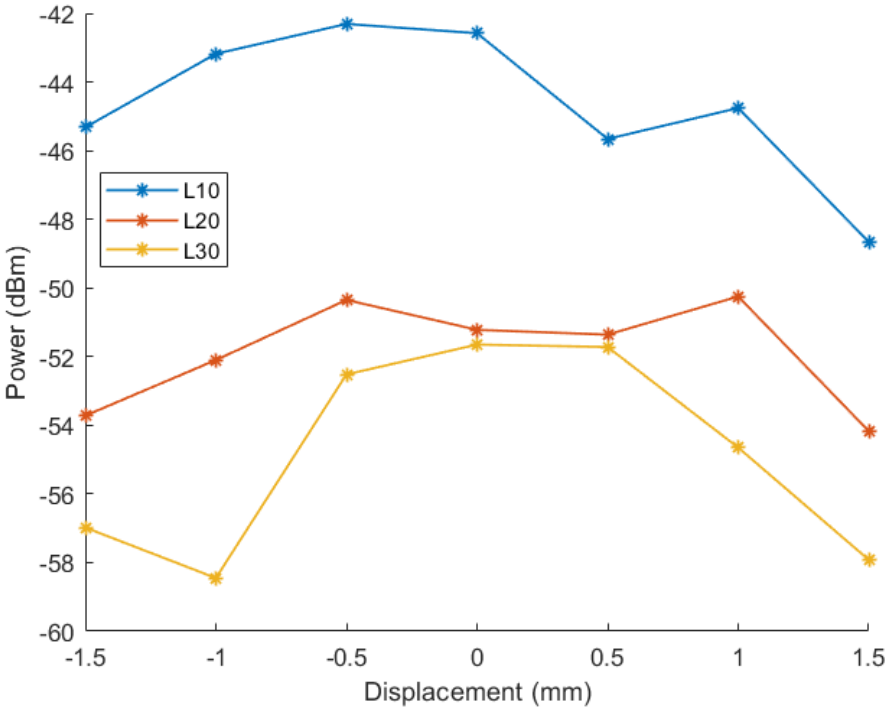

Figure 5.34: OAM power for different displacements without beam expander (P40 E28 surface)

In function of the speed of the disk

We went on to characterize the OAM according to the speed of the disk. We will change the speed of rotation of the surface increasing the power received by the motor so that we can compare the theoretical results from the equation $f_{mod} = \Omega|l_1 - l_2|/2\pi$ with the obtained in the oscilloscope applying the FFT.

- 1.- We calculate the rotation period for the four voltages used to perform the characterization being $V = 8.1\ V, 9\ V, 10\ V$ and $11\ V$. In $V = 11\ V$ we must stop because the vibrations begin to affect the assembly. In table 5.44 we show the angular velocities obtained from the rotation period of the disk for each voltage.

Voltage	Ω
$V = 8.1$ V	$\Omega = 141.51$ rad/s
$V = 9$ V	$\Omega = 161.52$ rad/s
$V = 10$ V	$\Omega = 183.71$ rad/s
$V = 11$ V	$\Omega = 193.32$ rad/s

Table 5.44: Angular speed for different voltages.

- 2.- We calculate the theoretical position where we should find the corresponding frequency modulations for each OAM order and for each of the angular frequencies. As before, we apply the equation $f_{mod} = \Omega|l_1 - l_2|/2\pi$ to obtain the position of the peak with the highest power.

- 3.- To finish, we made the comparison between the theoretical position and that obtained in the analysis with the measurements.

In tables 5.45-5.48 the theoretical modulation frequencies are represented along with those obtained during the measurements for each of the OAM orders at different voltages.

In graph 5.35 we can see the comparison between the theoretical curve of displacement in frequency and that obtained in the measurements. The positions where the modulations are found in frequency are very similar to those obtained theoretically, with the margin of error of the order of hertz. As in the previous analyzes, the results are the expected ones taking into account that the frequency shift is linked to the angular velocity of the disk and not to the fact that the radius of the OAM is greater or lesser.

On the other hand, for the graph 5.36, we see that the tendency that existed in the power to decrease when increasing the speed of rotation on the surface of the disk is not influential compared with some previous results. The power remains more or less constant in all orders, differing from each other by the power that each of them carries.

$V = 8.1\ V\ (\Omega = 140.87\ rad/s)$									
$l = \pm 10$		$l = \pm 20$		$l = \pm 30$		$l = \pm 40$		$l = \pm 50$	
$f_{mod\ theor}$	f_{mod}	$f_{mod\ theor}$	f_{mod}	$f_{mod\ theor}$	f_{mod}	$f_{mod\ theor}$	f_{mod}	$f_{mod\ theor}$	f_{mod}
450.44 Hz	457.8 Hz	900.88 Hz	900.3 Hz	1351.52 Hz	1350 Hz	1801.76 Hz	1810 Hz	2252.20 Hz	2234 Hz

Table 5.45: Theoretical frequency modulation and frequency modulation peak for different OAM orders and $V = 8.1\ V$

$V = 9\ V\ (\Omega = 160.69\ rad/s)$									
$l = \pm 10$		$l = \pm 20$		$l = \pm 30$		$l = \pm 40$		$l = \pm 50$	
$f_{mod\ theor}$	f_{mod}	$f_{mod\ theor}$	f_{mod}	$f_{mod\ theor}$	f_{mod}	$f_{mod\ theor}$	f_{mod}	$f_{mod\ theor}$	f_{mod}
514.13 Hz	511.2 Hz	1028.26 Hz	1016 Hz	1542.20 Hz	1556 Hz	2056.53 Hz	2055 Hz	2570 Hz	2559 Hz

Table 5.46: Theoretical frequency modulation and frequency modulation peak for different OAM orders and $V = 9\ V$

$V = 10\ V\ (\Omega = 183.02\ rad/s)$									
$l = \pm 10$		$l = \pm 20$		$l = \pm 30$		$l = \pm 40$		$l = \pm 50$	
$f_{mod\ theor}$	f_{mod}	$f_{mod\ theor}$	f_{mod}	$f_{mod\ theor}$	f_{mod}	$f_{mod\ theor}$	f_{mod}	$f_{mod\ theor}$	f_{mod}
584.76 Hz	572.2 Hz	1169.53 Hz	1167 Hz	1754.30 Hz	1759 Hz	2339.06 Hz	2324 Hz	2923.83 Hz	2924 Hz

Table 5.47: Theoretical frequency modulation and frequency modulation peak for different OAM orders and $V = 10\ V$

$V = 11\ V\ (\Omega = 197.08\ rad/s)$									
$l = \pm 10$		$l = \pm 20$		$l = \pm 30$		$l = \pm 40$		$l = \pm 50$	
$f_{mod\ theor}$	f_{mod}	$f_{mod\ theor}$	f_{mod}	$f_{mod\ theor}$	f_{mod}	$f_{mod\ theor}$	f_{mod}	$f_{mod\ theor}$	f_{mod}
615.35 Hz	605.8 Hz	1230.71 Hz	1219 Hz	1846.07 Hz	1857 Hz	2461.42 Hz	2463 Hz	3076.08 Hz	3069 Hz

Table 5.48: Theoretical frequency modulation and frequency modulation peak for different OAM orders and $V = 11\ V$

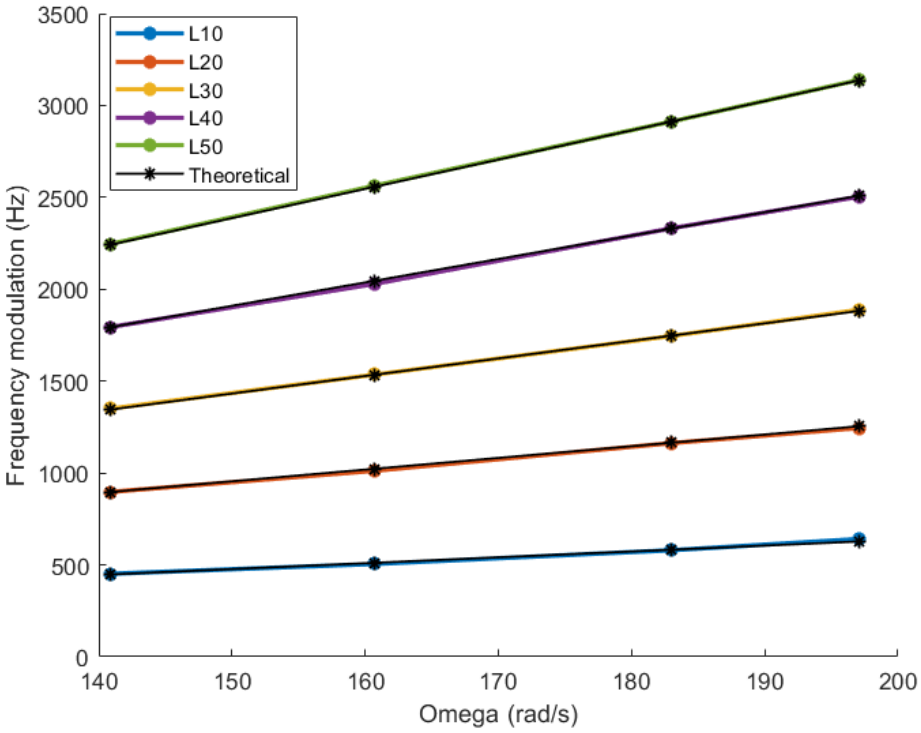

Figure 5.35: Angular velocity in function of frequency modulation without beam expander (P40 E28 surface)

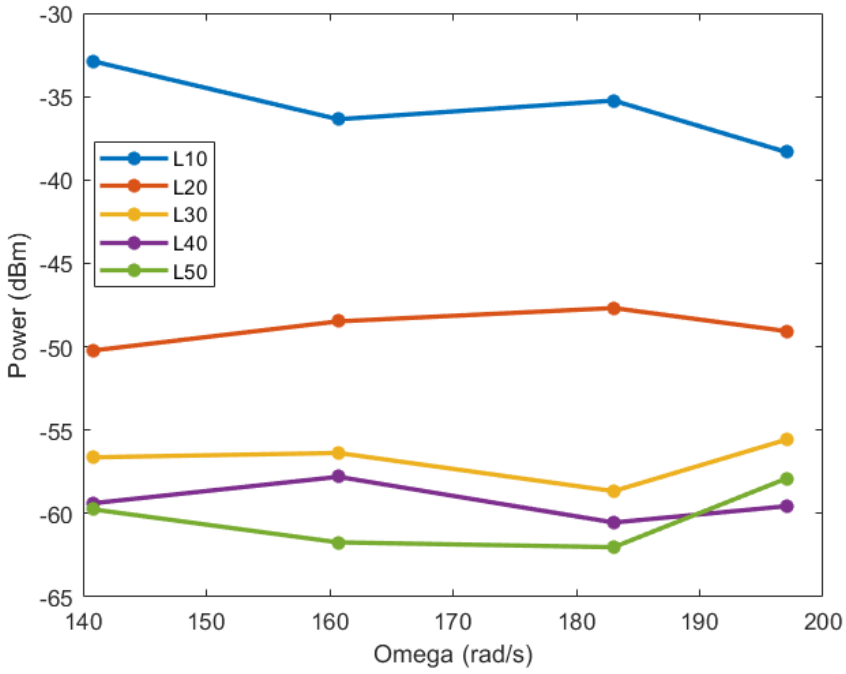

Figure 5.36: Angular velocity in function of OAM power without beam expander (P40 E28 surface)

Signal-to-Noise Ratio for differents OAM

We finish the realization of all the analyzes with the last of them. As in the previous cases, we will measure the noise level detected by the photodiode with and without OAM for each of the orders we have. In the tables 5.49-5.53 are represented the noise levels, together with the peaks of power belonging to each OAM order and the difference between them that gives us the signal-to-noise level of each OAM order .

$l = \pm 10$				
Voltage	Angular velocity	Power	Noise level	SNR
8.1 V	141.51 rad/s	-39.94 dBm	-66.43 dBm	26.49 dB
9 V	161.52 rad/s	-37.31 dBm	-64.23 dBm	26.92 dB
10 V	183.71 rad/s	-41.97 dBm	-65.24 dBm	23.27 dB
11 V	193.32 rad/s	-48.91 dBm	-64.7 dBm	15.79 dB

Table 5.49: SNR for $l = 10$ without beam expander (P40 E28 surface)

$l = \pm 20$				
Voltage	Angular velocity	Power	Noise level	SNR
8.1 V	141.51 rad/s	-52.26 dBm	-65.76 dBm	13.5 dB
9 V	161.52 rad/s	-53.79 dBm	-65.97 dBm	12.18 dB
10 V	183.71 rad/s	-52.91 dBm	-66.11 dBm	13.2 dB
11 V	193.32 rad/s	-49.39 dBm	-66.5 dBm	17.11 dB

Table 5.50: SNR for $l = 20$ without beam expander (P40 E28 surface)

$l = \pm 30$				
Voltage	Angular velocity	Power	Noise level	SNR
8.1 V	141.51 rad/s	-55.59 dBm	-63.49 dBm	7.9 dB
9 V	161.52 rad/s	-51.39 dBm	-63.98 dBm	12.59 dB
10 V	183.71 rad/s	-53.97 dBm	-65.41 dBm	11.44 dB
11 V	193.32 rad/s	-56.25 dBm	-65.11 dBm	8.86 dB

Table 5.51: SNR for $l = 30$ without beam expander (P40 E28 surface)

$l = \pm 40$				
Voltage	Angular velocity	Power	Noise level	SNR
8.1 V	141.51 rad/s	-57.67 dBm	-59.57 dBm	1.9 dB
9 V	161.52 rad/s	-58.8 dBm	-63.3 dBm	4.5 dB
10 V	183.71 rad/s	-59.12 dBm	-64.55 dBm	5.43 dB
11 V	193.32 rad/s	-57.76 dBm	-63.34 dBm	5.58 dB

Table 5.52: SNR for $l = 40$ without beam expander (P40 E28 surface)

$l = \pm 50$				
Voltage	Angular velocity	Power	Noise level	SNR
8.1 V	141.51 rad/s	-58.1 dBm	-62.06 dBm	3.96 dB
9 V	161.52 rad/s	-58.61 dBm	-63.51 dBm	4.9 dB
10 V	183.71 rad/s	-60.56 dBm	-63.81 dBm	3.25 dB
11 V	193.32 rad/s	-58.73 dBm	-66.43 dBm	7.7 dB

Table 5.53: SNR for $l = 50$ without beam expander (P40 E28 surface)

Representing in a graph this difference of power levels we obtain the figure 5.37, the level of signal to noise is greater the smaller the order is and, in general, it decreases slightly when we increase the rotation speed of the disk with which we make the beam impact. The two main reasons why this occurs are the speed of rotation and the frequency of acquisition with which the samples are taken.

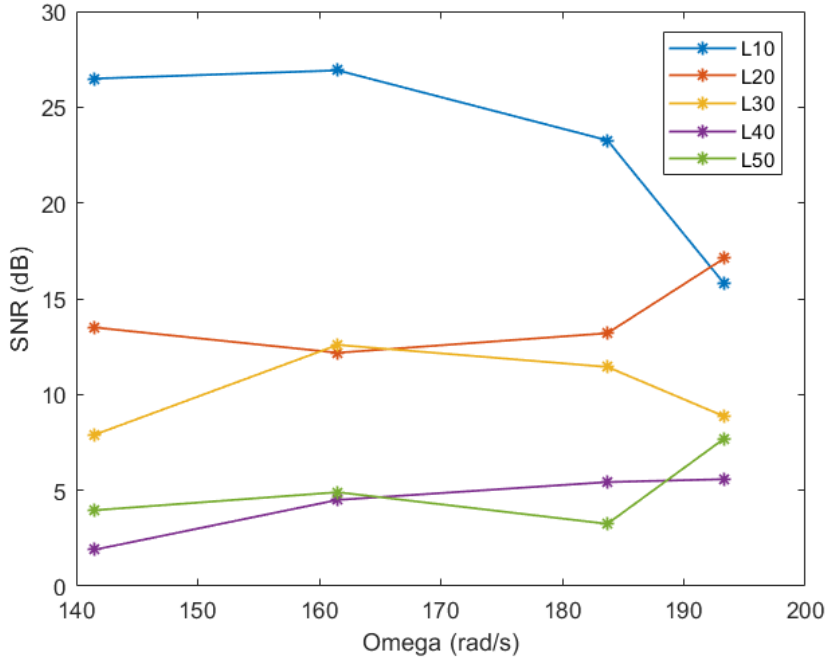

Figure 5.37: SNR without beam expander (P40 E28 surface)

Chapter 6

Comparative results

In this chapter we will make the final comparisons between the results obtained in the previous chapter. We will analyze the common cases trying to find a response to the behavior in each of the analyzes performed.

6.1 OAM power differencies between surfaces

We will start with the power difference between the different cases studied when we move the OAM of position, decentering it with respect to the axis of rotation of the disk. The idea is to make a comparison between the powers obtained for each surface used, together with the use or removal of beam expanders. Therefore, next we will represent a combined graph of the power obtained for each OAM order on each of the two surfaces analyzed with beam expanders.

In the figure 6.1 we observe the power obtained in the photodiode for each order, varying the position with which the OAM affects the rotating surface. We observe clearly a decreasing tendency of the power when we move laterally, being the central position, or very close to it, when we obtain the highest power. We can affirm that a good alignment with respect to the axis of rotation of the receiver to which we make an impact on the beam is crucial to obtain acceptable power results. From the graph we can also see that the highest power ranges have been obtained with the P80 E24 surface, which corresponds to the one with the highest roughness. The differences are not very high, but it is clearly observed that they predominate compared to those obtained from the P40 E28 surface.

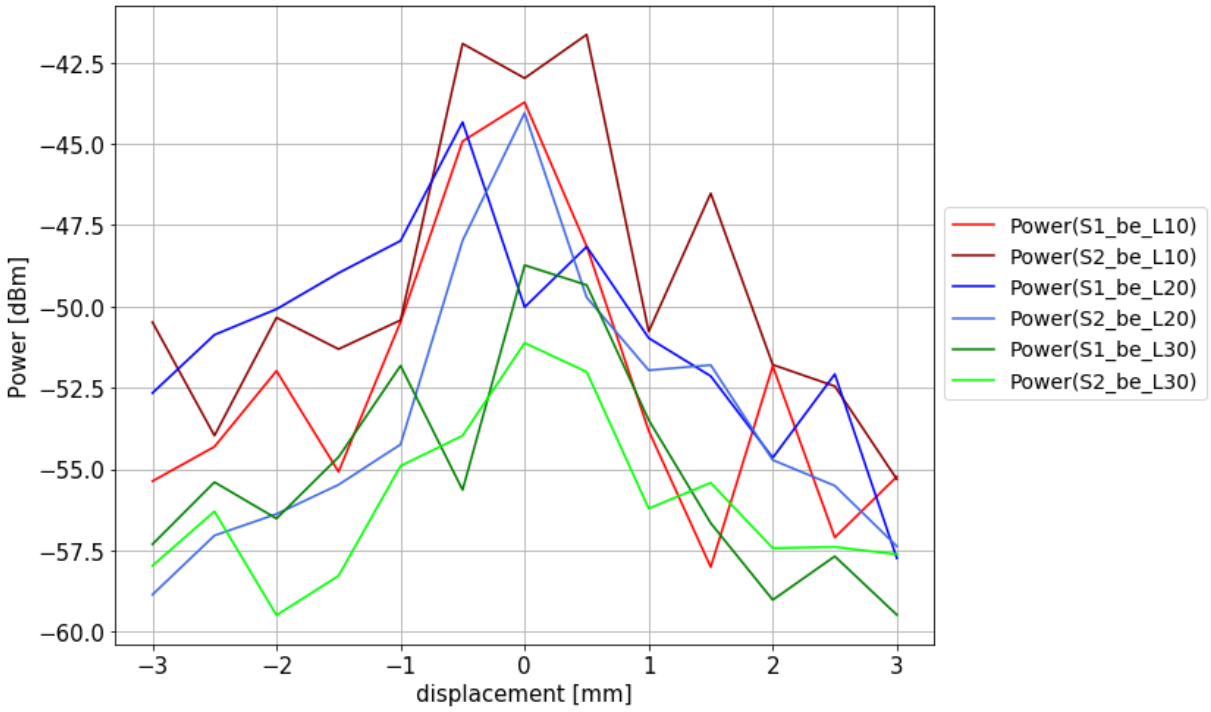

Figure 6.1: OAM power in both surfaces with beam expanders

This difference of power between surfaces we have represented in the figure 6.2. There are larger power differences in the lower orders because they have more power than those in higher orders.

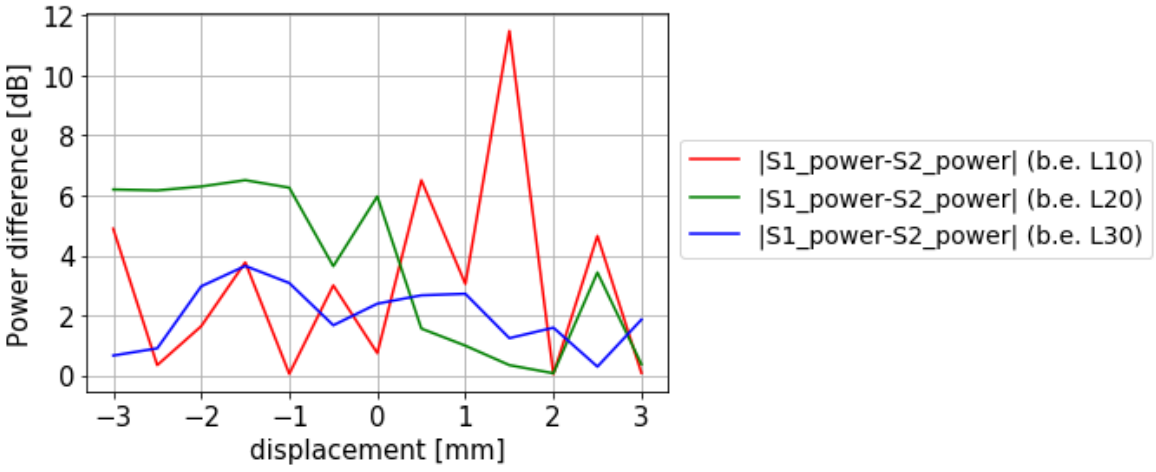

Figure 6.2: Power difference between surfaces with beam expanders

Now we go to the combined representation of the power obtained for each OAM order on the two surfaces, but this time without beam expanders. The figure 6.3 represents

the power measurements collected by the photodiode, this time the number of samples is reduced because the ring that forms the OAM has a smaller radius due to the absence of beam expanders, which impacts in the number of steps we can move the OAM laterally. As we have observed before, the highest powers are given for the lower OAM orders, we can see that the powers reached are greater than in the previous case. This is due to the absence of beam expanders, the ring that forms the OAM has a smaller radius so the power is more concentrated. This time we see that the high power values are not reached due to the rough surface in the case of $l = 10$ but not for orders $l = 20$ and $l = 30$, where the power moves between similar values.

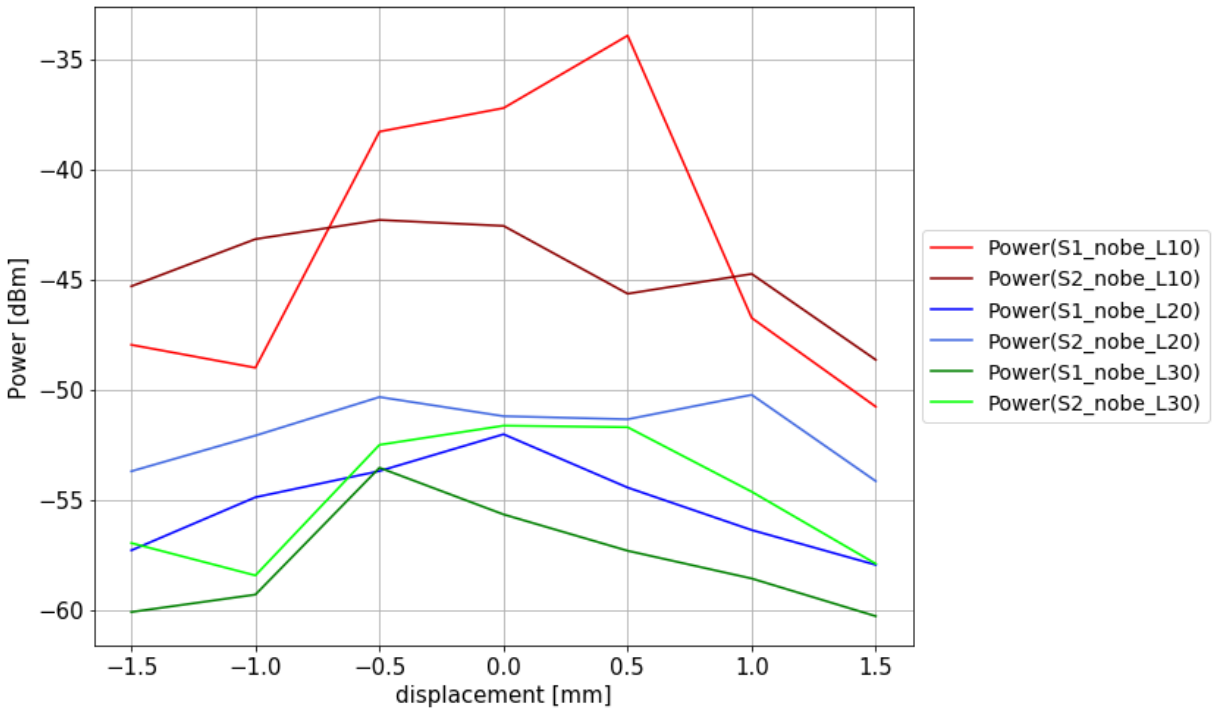

Figure 6.3: OAM power in both surfaces withou beam expanders

The power difference between surfaces is represented in the figure 6.4, the power difference for the order $l = 10$ is more remarkable than in the other two cases where we saw that the power was similar.

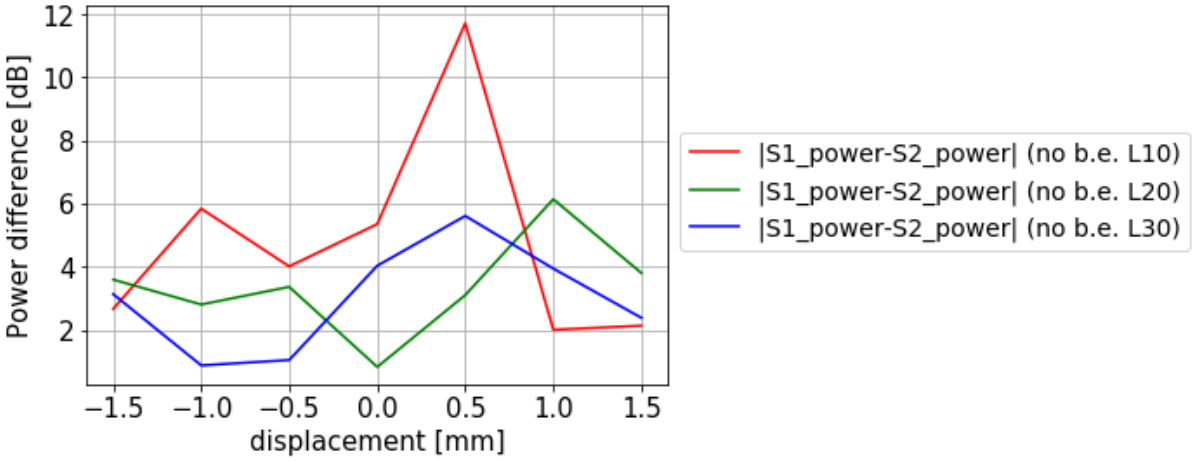

Figure 6.4: Power difference between surfaces withot beam expanders

As a curiosity we wanted to check if the power reduction when moving the rotation surface laterally was linked to a narrowing of the frequency modulation. To do this, we made some measurements of the bandwidth at $-3\ dB$ in the frequency modulations that were produced by varying the position of the disk. We perform this test for the mode $l = 10$ and a constant rotation speed of 8.1 V obtaining the following results:

$l = \pm 10$	
Displacement	$BW_{-3\ dB}$
-1 mm	1 Hz
-0.5 mm	1.3 Hz
0 mm	0.8 Hz
0.5 mm	1 Hz
1 mm	0.9 Hz

Table 6.1: $-3\ dB$ bandwidth

As can be seen in the table 6.1 we can not say that there is any relationship between the lateral displacement of the OAM with the power reduction of the peaks belonging to the modulations in frequency of the spectrum.

6.2 Frequency differencies between surfaces

The frequency of modulation suffers a frequency shift directly proportional to the speed of rotation of the receiver with which we make an impact on the beam. In this comparison, we will analyze if there is a notable difference between the positions where the modulation frequencies are found for the two surfaces we have analyzed.

In the figure 6.5 we observe the positions of the modulation frequencies for each of the surfaces using the beam expanders. At first sight we observe that the trends are practically identical for each of the OAM orders analyzed, we could even predict the trend at higher speeds. Even so, looking a little more at the graph, we can see that there is a small margin between lines that increases when we increase the OAM order with which we work. From the data we have observed that the positions where the modulation frequencies are at higher points are given for the less rough surface at low speeds, corresponding to P40 E28. As the rotation speed increases, the trend reverses, with the P80 E24 surface moving farther away.

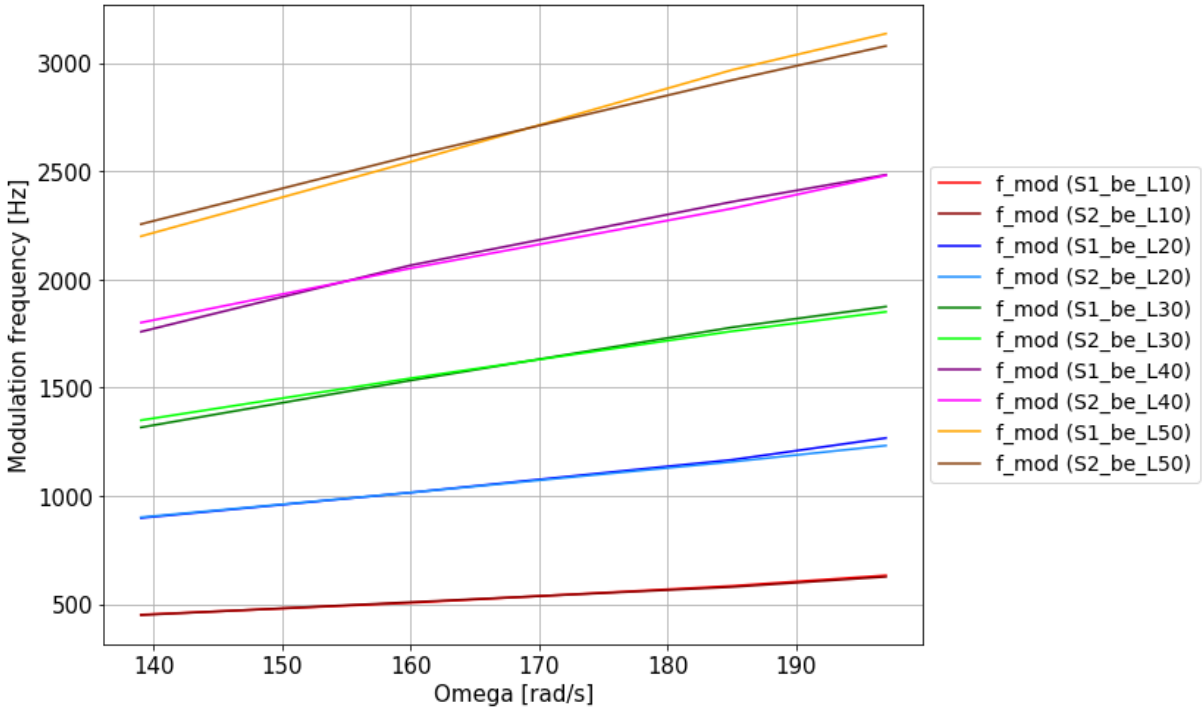

Figure 6.5: Modulation frequency in both surfaces with beam expanders

This difference between the modulation frequencies is compared in the figure 6.6. As we said, the difference in frequency is more noticeable for larger orders. The decreasing line to 160 rad/s corresponds to the frequency difference for the P40 E28 surface, whose influence is high at low speeds and decreases when increasing them. From 160 rad/s is when this difference increases again but in this case due to the surface P80 E24.

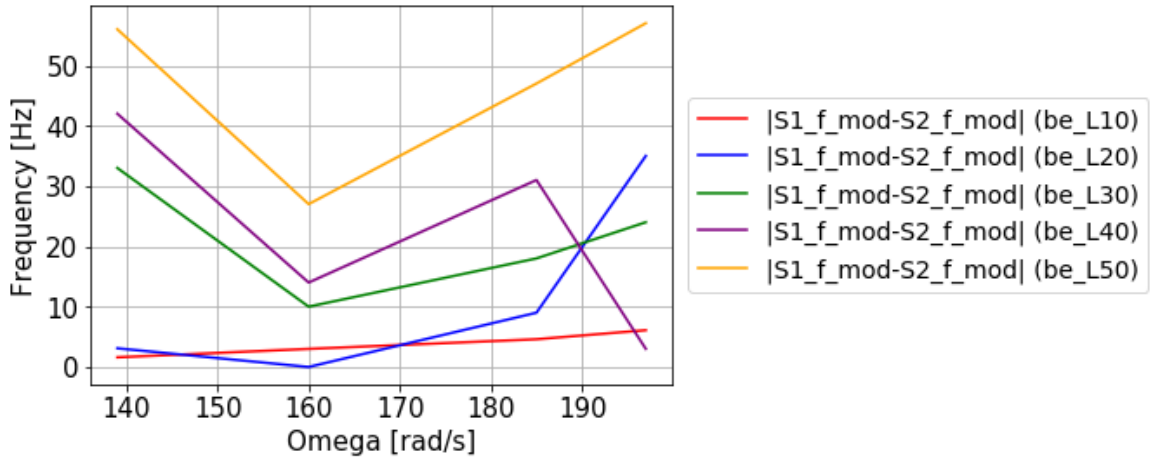

Figure 6.6: Frequency difference between surfaces with beam expanders

Now we turn to the representation of the positions of the modulation frequencies without the use of beam expanders. In the figure 6.7 the trend of the lines is equal to the views for the case with the beam expanders. In this case we can not distinguish notable differences only by observing the graph, except that from speeds higher than 185 rad/s an observable difference between the lines begins to appear. Observing the data, we found that, as in the previous case, the positions occupied by the modulation frequencies at higher points correspond to the rough surface P80 E24. On the other hand at lower speeds the difference is much lower than the previous case.

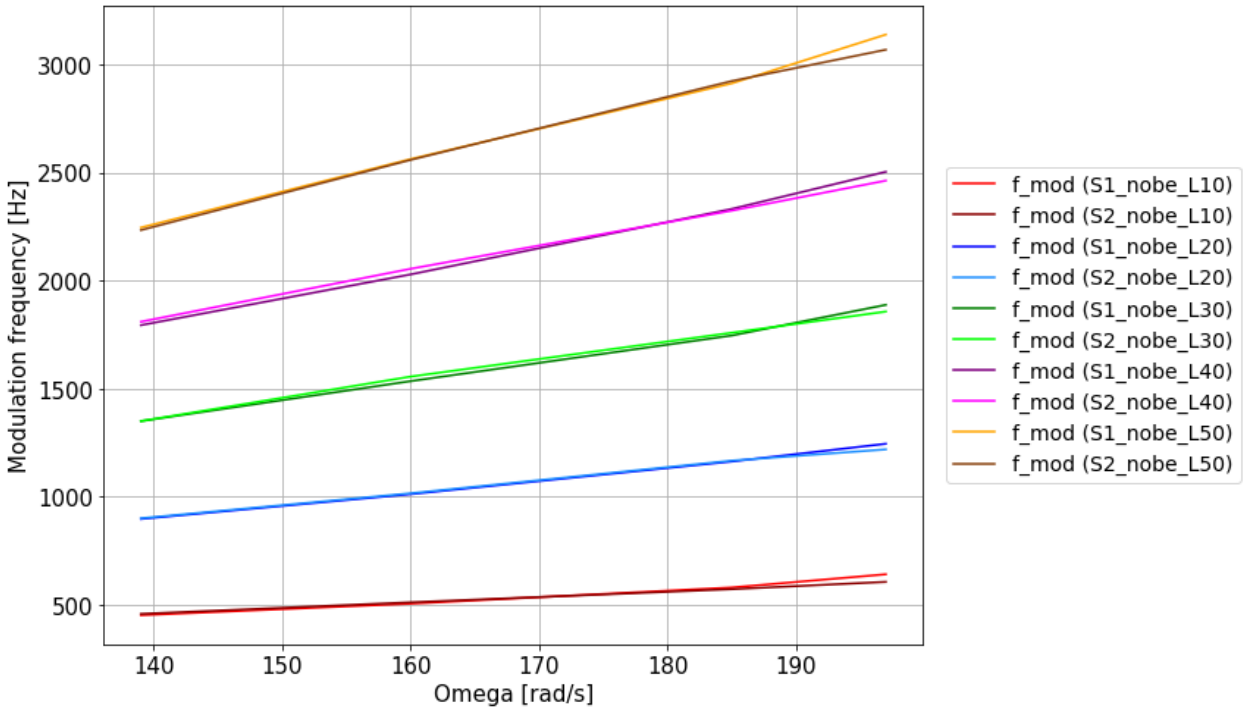

Figure 6.7: Modulation frequency in both surfaces without beam expanders

This difference between frequencies is represented in the graph 6.8. On this occasion, at low speeds, the difference between the modulation frequencies is much lower than in the previous case, with very similar values being maintained in some orders. Even so, the trend when we reach high velocity values triggers the difference between them, being more influential for higher OAM orders.

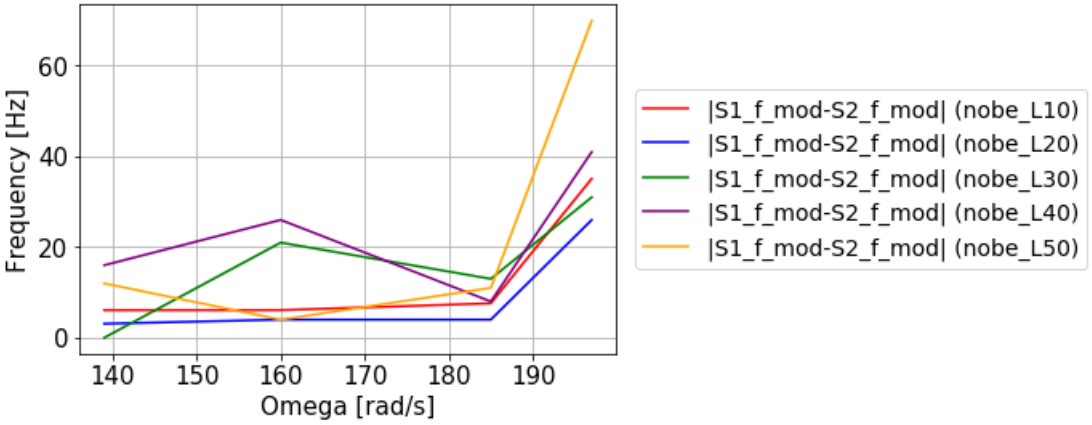

Figure 6.8: Frequency difference between surfaces without beam expanders

6.3 SNR between surfaces

The signal-to-noise ratio (SNR) is calculated as the difference between the noise level of the system and the level of power that reaches our photodiode. We will make a comparison between the SNR obtained for each surface together with the use or removal of the beam expanders.

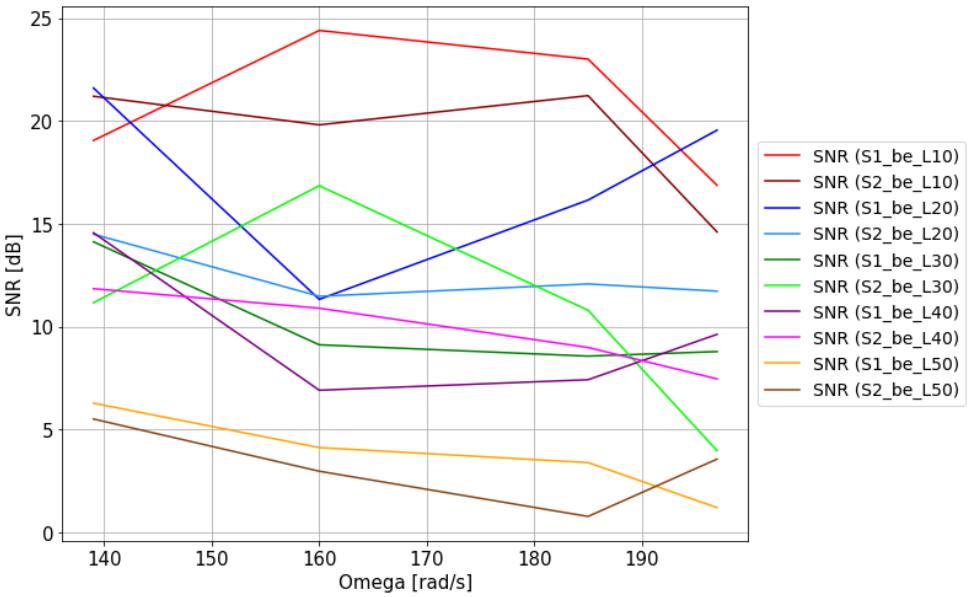

Figure 6.9: SNR in both surfaces with beam expanders

In the figure 6.9 we observe the SNR measured for each OAM order in each of the surfaces for the case in which we use beam expanders. With this graph we can know the power implicit in each OAM order, which we observe does not exceed 25 dB in the best case. As we have already deduced, the lowest order OAMs hold the highest positions and these decrease with the increase in the order of the OAM that we are analyzing. In this case, the fact of using one surface or another does not reflect a clear trend since SNRs sometimes have higher values for the rough surface and in others for those with less roughness. What is observed is a tendency to decrease this SNR by increasing the speed of rotation of the surface.

On the other hand, in the figure 6.10 we see that the powers reached are superior in most cases but also not remarkable and that they are due to the removal of the beam expanders. In this analysis the lower order OAMs still hold the highest positions in terms of SNR but the difference between the values using one surface or another is less distant from each other. In this case, there is also a slight tendency to decrease the SNR by increasing the speed of rotation of the surface.

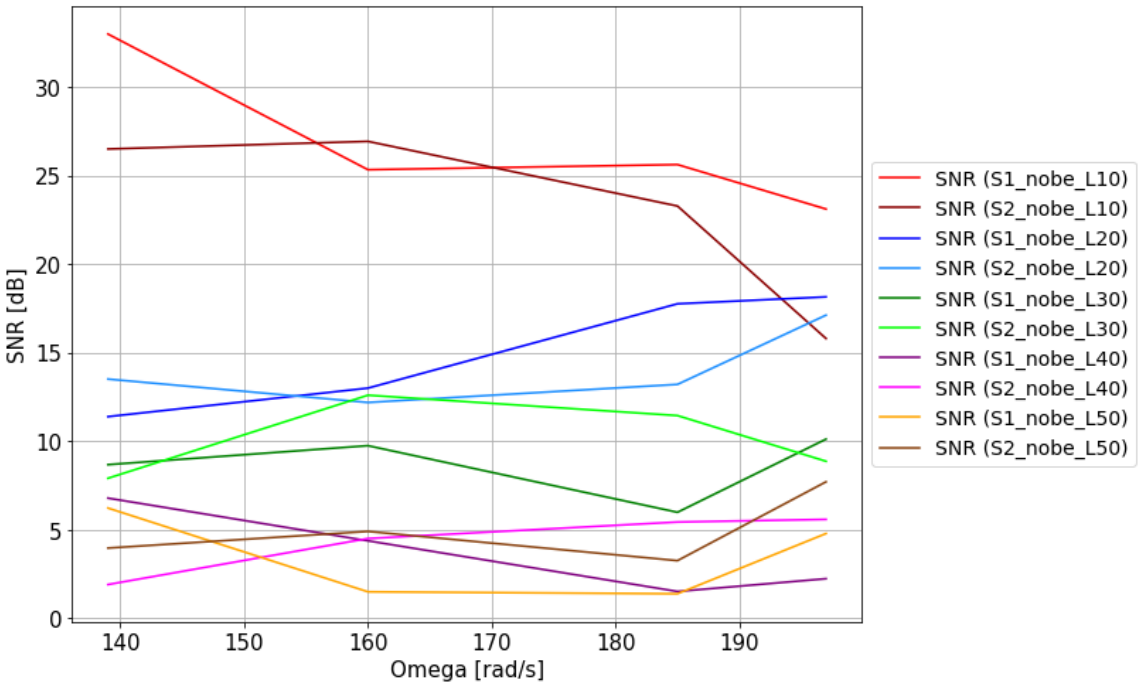

Figure 6.10: SNR in both surfaces without beam expanders

Chapter 7

Conclusions and future lines

The aim of this work has been the implementation and characterization of a LIDAR system to measure the angular speed of a rotating object. Different analyzes of simulations have been carried out to confirm the validation of the experimental results.

In this work, the study of the orbital angular momentum of light has been reported under certain modifiable parameters of a laboratory assembly. During the assembly I was able to verify the difficulties involved in performing laser experiments in free space. There are many external conditions that can alter the results such as vibrations produced by external devices, lighting conditions of the environment, the margin of error existing when aligning the setup or the randomness with which the reflected beams can impact a photoreceiver.

The characterizations carried out have focused on how this OAM behaves in terms of power and frequency when certain elements of the laboratory assembly varied, such as the surface with which the beam was reflected, that is, a supposed receiver in rotation. We also changed the OAM's orders so that the light pattern and size change, as well as the energy it carries. It even occurred to us to use or not certain elements of the setup such as beam expanders. The use of elements such as the spatial light modulator was crucial for the study since it allowed us to superimpose two different OAMs to obtain the desired frequency modulation.

Given this approach, we consider the main objective of this work to establish a base for a more in-depth study of OAM where we can continue studying the properties of this phenomenon, focused in this work on the detection of rotating objectives. Several technical challenges were encountered, some were resolved, others were not. However, new approaches to the project were considered, such as measurements of the flow vorticity with light beams.

In general, I finish this work with satisfaction. This project can be considered a good starting point on the analysis of certain characteristics of the OAM under certain conditions and I hope it can be useful for those who need to know a little more or are interested in the study of light and its applications.

As for future lines, the experiment can be improved to obtain more accurate measurements if the assembly is studied and a solution is made to some of the problems described during the execution of this work. In the absence of time for further experiments, an approach was proposed to use the OAM and perform vorticity measurements on fluids. As we could read in many scientific publications, the results obtained are very interesting when making measurements on the OAM. On the other hand, the fact of being able to detect the angular velocity of an objective with a more efficient system opens many doors to the development of a LIDAR system that could compete and be more efficient in certain circumstances than a radar system.

Bibliography

[1] C. Rosales-Guzmán, N. Hermosa, A. Belmonte, and J. P. Torres, "Experimental detection of transverse particle movement with structured light," *Scientific Reports*, vol. 3, pp. 1–5, 2013.

[2] A. Safaripour, S. Pouya, M. Dantus, A. Ryabtsev, and M. Koochesfahani, "Fluid flow vorticity measurement using laser beams with orbital angular momentum," *Optics Express*, vol. 24, no. 11, p. 11762, 2016.

[3] N. Ahmed, H. Huang, M. J. Willner, M. P. J. Lavery, M. Tur, S. J. Dolinar, M. J. Padgett, D. Rogawski, Y. Ren, Y. Yan, B. I. Erkmen, A. E. Willner, G. Xie, Y. Yue, and K. M. Birnbaum, "100 Tbit/s free-space data link enabled by three-dimensional multiplexing of orbital angular momentum, polarization, and wavelength," *Optics Letters*, vol. 39, no. 2, p. 197, 2014.

[4] A. M. Yao and M. J. Padgett, "Orbital angular momentum: origins, behavior and applications," *Advances in Optics and Photonics*, vol. 3, no. 2, p. 161, 2011.

[5] V. Alwayn, "Optical Network Design and Implementation," *Cisco Press*, 2004.

[6] M. Ibrahim, "Brief History of optical fiber," 2017.

[7] M. Bellis, "The History of Fiber Optics from Bell's Photophone to Corning Researchers," 2018.

[8] S. Vallmitjana, "Transmission of Light By Fibers For Optical Communication," *Contributions to Science*, vol. 7, no. 2, pp. 117–124, 2009.

[9] N. Massa, "Fiber Optic Telecommunication," *Springfield Technical Community College*, pp. 293–347, 2000.

[10] R. Paschotta, "Encyclopedia of Laser Physics and Technology."

[11] J. A. M. Pereda, "Sistemas y Redes Opticas de Comunicaciones," *Editorial Pearson Educacion S.A.,*, 2004.

[12] A. Gumaste and T. Antony, *DWDM Network Design and Engineering Solutions*. Indianapolis, IN 46290 USA: Cisco Press, 2003.

[13] A. Crawls, "HBBCL Free-Space Optical Communications," 2007.

[14] M. Padgett, J. Courtial, and L. Allen, "Light's Orbital Angular Momentum," *Physics Today*, vol. 57, no. May, pp. 35–40, 2004.

[15] J. D. V. Sabino, *Orbital Angular Momentum of photons : a tool to transmit information.* PhD thesis, 2016.

[16] M. Padgett, "Light's Twist," *Proc. R. Soc. A*, vol. 470, p. 20140633, 2014.

[17] A. Madeira, "Study of Photons Orbital Angular Momentum for Optical Communications André Madeira Bastos da Cunha Thesis to obtain the Master of Science Degree in Engineering Physics," no. November, 2015.

[18] L. Marrucci, "The q-plate and its future," *Journal of nanophotonics*, 2018.

[19] M. P. J. Lavery, S. M. Barnett, F. C. Speirits, and M. J. Padgett, "Observation of the rotational Doppler shift of a white-light, orbital-angular-momentum-carrying beam backscattered from a rotating body," *Optica*, vol. 1, no. 1, p. 1, 2014.

[20] M. V. Vasnetsov, V. A. Pas'ko, and M. S. Soskin, "Analysis of orbital angular momentum of a misaligned optical beam," *New Journal of Physics*, vol. 7, 2005.

[21] X. Zhang, H. Zhou, J. Dong, D. Fu, and P. Zhang, "Theoretical analysis and experimental verification on optical rotational Doppler effect," *Optics Express*, vol. 24, no. 9, p. 10050, 2016.

[22] W. Zhai, W. Xu, X. Gao, W. Gu, S. Huang, M. Zhao, and M. Xie, "Measurement of the rotational Doppler frequency shift of a spinning object using a radio frequency orbital angular momentum beam," *Optics Letters*, vol. 41, no. 11, p. 2549, 2016.

Matlab codes

Surface 1. Characterization with beam spander

DisplacementxPower

```
clear all
clc

x = [-3 -2.5 -2 -1.5 -1 -0.5 0 0.5 1 1.5 2 2.5 3];
load('DisplacementxPower.mat');

figure()
hold on
plot(x, DisplacementxPower, 'marker', '*', 'linewidth', 1)
xlabel('Displacement (mm)')
ylabel('Power (dBm)')
legend('L10', 'L20', 'L30')
```

Velocity Motor Measurements OmegaxFmod

```
clear all
clc

Omega = [139.07 160.69 185.94 197.02];
load('VxF.mat');

figure()

hold on
plot(Omega, VxF, 'marker', '*', 'linewidth', 2)
xlabel('Omega (rad/s)')
ylabel('Frequency modulation (Hz)')
legend('L10', 'L20', 'L30', 'L40', 'L50')

%Compare to the theoretical one
```

```
load('VxF_Theorical');
plot(Omega, VxF_Theorical, 'black', 'marker', '*', 'linewidth', 1);
legend('L10', 'L20', 'L30', 'L40', 'L50', 'Theoretical')
hold off
```

Velocity Motor Measurements OmegaxPower

```
clear all
clc

x = [139.07, 160.69, 185.94, 197.02];
load('VxP.mat');

figure()
plot(x, VxP, 'marker', '*', 'linewidth', 2)
xlabel('Omega (rad/s)')
ylabel('Power (dBm)')
legend('L10','L20','L30','L40', 'L50')
```

SNR

```
clear all
clc

x = [139.07, 160.69, 185.94, 197.02];
load('Power_difference');

figure()
plot(x, Power_difference, 'marker', '*', 'linewidth', 1)
xlabel('Omega (rad/s)')
ylabel('SNR (dB)')
legend('L10','L20','L30','L40','L50')
```

Surface 1. Characterization without beam spander

DisplacementxPower

```
clear all
```

```
clc

x = [-1.5 -1 -0.5 0 0.5 1 1.5];
load('DisplacementxPower.mat');

figure()
hold on
plot(x, DisplacementxPower, 'marker', '*', 'linewidth', 1)
xlabel('Displacement (mm)')
ylabel('Power (dBm)')
legend('L10', 'L20', 'L30')
```

Velocity Motor Measurements VoltagexFmodulation

```
clear all
clc

x = [8.1 9 10 11];
load('VxF.mat');

figure()
hold on
plot(x, VxF, 'marker', '*', 'linewidth', 2)
xlabel('Voltage (V)')
ylabel('Frequency modulation (Hz)')

%Compare to the theoretical one

load('VxF_Theorical');
plot(x, VxF_Theorical, 'black', 'marker', '*', 'linewidth', 1);
legend('L10', 'L20', 'L30', 'L40', 'L50')
hold off
```

Velocity Motor Measurements VoltagexPower

```
clear all
clc

x = [8.1 9 10 11];
load('VxP.mat');
```

```
figure()
plot(x, VxP, 'marker', '*', 'linewidth', 2)
xlabel('Voltage (V)')
ylabel('Power (dBm)')
legend('L10','L20','L30','L40','L50')
```

SNR

```
clear all
clc

x = [8.1 9 10 11];
load('VxP.mat');
load('Power_difference');

figure()

plot(x, VxP, 'marker', '*', 'linewidth', 1)
xlabel('Omega (rad/s)')
ylabel('SNR (dB)')
legend('L10','L20','L30','L40','L50')

figure()
plot(x, Power_difference, 'marker', '*', 'linewidth', 1)
xlabel('Omega (rad/s)')
ylabel('SNR (dB)')
legend('L10','L20','L30','L40','L50')
```

Surface 2. Characterization with beam spander

DisplacementxPower

```
clear all
clc

x = [-3 -2.5 -2 -1.5 -1 -0.5 0 0.5 1 1.5 2 2.5 3];
load('DisplacementxPower.mat');

figure()
hold on
plot(x, DisplacementxPower, 'marker', '*', 'linewidth', 1)
```

```
xlabel('Displacement (mm)')
ylabel('Power (dBm)')
legend('L10', 'L20', 'L30')
```

Velocity Motor Measurements VoltagexOmega

```
clear all
clc

Omega = [141.51 161.52 183.71 194.52];
load('VxF.mat');

figure()

hold on
plot(Omega, VxF, 'marker', '*', 'linewidth', 2)
xlabel('Omega (rad/s)')
ylabel('Frequency modulation (Hz)')
legend('L10', 'L20', 'L30', 'L40', 'L50')

%Compare to the theoretical one

load('VxF_Theorical');
plot(Omega, VxF_Theorical, 'black', 'marker', '*', 'linewidth', 1);
legend('L10', 'L20', 'L30', 'L40', 'L50', 'Theoretical')
hold off
```

Velocity Motor Measurements OmegaxPower

```
clear all
clc

x = [141.51 161.52 183.71 194.52];
load('VxP.mat');

figure()
plot(x, VxP, 'marker', '*', 'linewidth', 2)
xlabel('Omega (rad/s)')
ylabel('Power (dBm)')
legend('L10','L20','L30','L40', 'L50')
```

SNR

```
clear all
clc

x = [8.1 9 10 11];
load('VxP.mat');
load('Power_difference');

figure()

plot(x, VxP, 'marker', '*', 'linewidth', 1)
xlabel('Voltage (V)')
ylabel('Power(dBm)')
legend('L10','L20','L30','L40','L50')
title('OAM power with noise level')

figure()
plot(x, Power_difference, 'marker', '*', 'linewidth', 1)
xlabel('Voltage (V)')
ylabel('OAM (dB)')
legend('L10','L20','L30','L40','L50')
title('OAM real scenario')
```

Surface 2. Characterization without beam spander

DisplacementxPower

```
clear all
clc

x = [-1.5 -1 -0.5 0 0.5 1 1.5];
load('DisplacementxPower.mat');

figure()
hold on
plot(x, DisplacementxPower, 'marker', '*', 'linewidth', 1)
xlabel('Displacement (mm)')
ylabel('Power (dBm)')
legend('L10', 'L20', 'L30')
```

Velocity Motor Measurements VoltagexFmodulation

```
clear all
clc

x = [8.1 9 10 11];
load('VxF.mat');

figure()
hold on
plot(x, VxF, 'marker', '*', 'linewidth', 2)
xlabel('Voltage (V)')
ylabel('Frequency modulation (Hz)')

%Compare to the theoretical one

load('VxF_Theorical');
plot(x, VxF_Theorical, 'black', 'marker', '*', 'linewidth', 1);
legend('L10', 'L20', 'L30', 'L40', 'L50')
hold off
```

Velocity Motor Measurements VoltagexOmega

```
clear all
clc

Omega = [141.51 161.52 183.71 193.32];
load('VxF.mat');

figure()

hold on
plot(Omega, VxF, 'marker', '*', 'linewidth', 2)
xlabel('Omega (rad/s)')
ylabel('Frequency modulation (Hz)')
legend('L10', 'L20', 'L30', 'L40', 'L50')

%Compare to the theoretical one

load('VxF_Theorical');
plot(Omega, VxF_Theorical, 'black', 'marker', '*', 'linewidth', 1);
legend('L10', 'L20', 'L30', 'L40', 'L50', 'Theoretical')
hold off
```

SNR

```
clear all
clc

x = [141.51 161.52 183.71 193.32];
load('VxP.mat');
load('Power_difference');

figure()

plot(x, VxP, 'marker', '*', 'linewidth', 1)
xlabel('Voltage (V)')
ylabel('Power(dBm)')
legend('L10','L20','L30','L40','L50')

figure()
plot(x, Power_difference, 'marker', '*', 'linewidth', 1)
xlabel('Omega (rad/s)')
ylabel('SNR (dB)')
legend('L10','L20','L30','L40','L50')
```

Theoretical sift frequency for differents displacements

```
clear all
clc

m = 10;             %OAM order
Phi = [0 pi/4 pi/2 3*pi/4 pi];
v = 0.1;            %m/s
r = 7*10^-3;        %mm (radio)
x = 5*10^-3;

Rho = zeros(5);
d0 = zeros(5);
fmod = zeros(5);

for i = 1:5
Rho(i) = sqrt(((r*cos(Phi(i))-x)^2) + (r*sin(Phi(i)))^2);

d0(i) = sin(Phi(i))*Rho(i);

fmod(i) = (m*d0(i)*v)/(2*pi*(Rho(i))^2);
```

```
end

figure()
plot(Phi, fmod, 'marker', '*', 'linewidth', 1)
xlabel('Displacement (m)')
ylabel('Frequency modulation (Hz)')

%%

clear all
clc

m = 10;                                 %OAM order
Phi = [0 pi/4 pi/2 3*pi/4 pi];
v = 0.1;                                %m/s
r = 7*10^-3;                            %mm (radio)
x = [0 1*10^-3 2*10^-3 3*10^-3 4*10^-3 5*10^-3 6*10^-3 7*10^-3 8*10^-3];

Rho = zeros(5);
d0 = zeros(5);
fmod = zeros(5);

C = {'k','b','r','g','y',[.5 .6 .7],[.8 .2 .6]};     %Color Array
```

Python codes

OAM power differencies between surfaces

```
import pandas as pd
import matplotlib.pyplot as plt

df = pd.read_csv("Displacement_measurements.csv")

plt.figure(figsize=(10,8))

#Fila y columna a graficar
plt.plot(df['displacement'], df['Power(S1_be_L10)'], color='red',
label='Power(S1_be_L10)')
plt.plot(df['displacement'], df['Power(S2_be_L10)'], color='darkred',
label='Power(S2_be_L10)')

plt.plot(df['displacement'], df['Power(S1_be_L20)'], color='blue',
label='Power(S1_be_L20)')
plt.plot(df['displacement'], df['Power(S2_be_L20)'], color='royalblue',
label='Power(S2_be_L20)')

plt.plot(df['displacement'], df['Power(S1_be_L30)'], color='green', label='Power(S1_be
plt.plot(df['displacement'], df['Power(S2_be_L30)'], color='lime', label='Power(S2_be_


#Colocamos una rejilla de fondo
plt.grid(True)

#Escribimos la leyenda
plt.legend(loc='upper left', fontsize=14, bbox_to_anchor=(1, 0.7))

#Colocamos título y nombre a los ejes
plt.xlabel('displacement [mm]', fontsize=15)
plt.ylabel('Power [dBm]', fontsize=15)
plt.tick_params(labelsize=15)
```

```
#Imprimimos la gráfica en un formato de archivo a elegir
plt.savefig('displacement_1.png', bbox_inches='tight')

#Mostramos la gráfica por terminal
plt.show()


#-------------------------------------------------------------------------

import pandas as pd
import matplotlib.pyplot as plt

df = pd.read_csv("Displacement_measurements.csv")

d1 = abs(df['Power(S1_be_L10)'] - df['Power(S2_be_L10)'])
d2 = abs(df['Power(S1_be_L20)'] - df['Power(S2_be_L20)'])
d3 = abs(df['Power(S1_be_L30)'] - df['Power(S2_be_L30)'])

plt.figure()

#Fila y columna a graficar
plt.plot(df['displacement'], d1, color='red',
label='|S1_power-S2_power| (b.e. L10)')
plt.plot(df['displacement'], d2, color='green',
label='|S1_power-S2_power| (b.e. L20)')
plt.plot(df['displacement'], d3, color='blue',
label='|S1_power-S2_power| (b.e. L30)')

#Colocamos una rejilla de fondo
plt.grid(True)

#Escribimos la leyenda
plt.legend(loc='upper left', fontsize=14, bbox_to_anchor=(1, 0.7))

#Colocamos título y nombre a los ejes
plt.xlabel('displacement [mm]', fontsize=15)
plt.ylabel('Power difference [dB]', fontsize=15)
plt.tick_params(labelsize=15)

#Imprimimos la gráfica en un formato de archivo a elegir
plt.savefig('displacement_2.png', bbox_inches='tight')

#Mostramos la gráfica por terminal
plt.show()
```

```
#-------------------------------------------------------------------------

import pandas as pd
import matplotlib.pyplot as plt

df = pd.read_csv("Displacement_measurements.csv")

plt.figure(figsize=(10,8))

#Fila y columna a graficar
plt.plot(df['displacement'], df['Power(S1_nobe_L10)'], color='red',
label='Power(S1_nobe_L10)')
plt.plot(df['displacement'], df['Power(S2_nobe_L10)'], color='darkred',
label='Power(S2_nobe_L10)')

plt.plot(df['displacement'], df['Power(S1_nobe_L20)'], color='blue',
label='Power(S1_nobe_L20)')
plt.plot(df['displacement'], df['Power(S2_nobe_L20)'], color='royalblue',
label='Power(S2_nobe_L20)')

plt.plot(df['displacement'], df['Power(S1_nobe_L30)'], color='green',
label='Power(S1_nobe_L30)')
plt.plot(df['displacement'], df['Power(S2_nobe_L30)'], color='lime',
label='Power(S2_nobe_L30)')


#Colocamos una rejilla de fondo
plt.grid(True)

#Escribimos la leyenda
plt.legend(loc='center right', fontsize=14, bbox_to_anchor=(1.375, 0.5))

#Colocamos título y nombre a los ejes
plt.xlabel('displacement [mm]', fontsize=15)
plt.ylabel('Power [dBm]', fontsize=15)
plt.tick_params(labelsize=15)

#Imprimimos la gráfica en un formato de archivo a elegir
plt.savefig('displacement_3.png', bbox_inches='tight')

#Mostramos la gráfica por terminal
plt.show()
```

```
#-------------------------------------------------------------------------

import pandas as pd
import matplotlib.pyplot as plt

df = pd.read_csv("Displacement_measurements.csv")

d1 = abs(df['Power(S1_nobe_L10)'] - df['Power(S2_nobe_L10)'])
d2 = abs(df['Power(S1_nobe_L20)'] - df['Power(S2_nobe_L20)'])
d3 = abs(df['Power(S1_nobe_L30)'] - df['Power(S2_nobe_L30)'])


plt.figure()

#Fila y columna a graficar
plt.plot(df['displacement'], d1, color='red',
label='|S1_power-S2_power| (no b.e. L10)')
plt.plot(df['displacement'], d2, color='green',
label='|S1_power-S2_power| (no b.e. L20)')
plt.plot(df['displacement'], d3, color='blue',
label='|S1_power-S2_power| (no b.e. L30)')

#Colocamos una rejilla de fondo
plt.grid(True)

#Escribimos la leyenda
plt.legend(loc='upper left', fontsize=14, bbox_to_anchor=(1, 0.7))

#Colocamos título y nombre a los ejes
plt.xlabel('displacement [mm]', fontsize=15)
plt.ylabel('Power difference [dB]', fontsize=15)
plt.tick_params(labelsize=15)

#Imprimimos la gráfica en un formato de archivo a elegir
plt.savefig('displacement_4.png', bbox_inches='tight')

#Mostramos la gráfica por terminal
plt.show()
```

Frequency differencies between surfaces

```
import pandas as pd
```

```
import matplotlib.pyplot as plt

df = pd.read_csv("Speed_measurements.csv")


plt.figure(figsize=(10,8))

plt.plot(df['omega'], df['f_mod_S1_be_L10'], color='red',
label='f_mod (S1_be_L10)')
plt.plot(df['omega'], df['f_mod_S2_be_L10'], color='darkred',
label='f_mod (S2_be_L10)')

plt.plot(df['omega'], df['f_mod_S1_be_L20'], color='blue',
label='f_mod (S1_be_L20)')
plt.plot(df['omega'], df['f_mod_S2_be_L20'], color='dodgerblue',
label='f_mod (S2_be_L20)')

plt.plot(df['omega'], df['f_mod_S1_be_L30'], color='green',
label='f_mod (S1_be_L30)')
plt.plot(df['omega'], df['f_mod_S2_be_L30'], color='lime',
label='f_mod (S2_be_L30)')

plt.plot(df['omega'], df['f_mod_S1_be_L40'], color='purple',
label='f_mod (S1_be_L40)')
plt.plot(df['omega'], df['f_mod_S2_be_L40'], color='fuchsia',
label='f_mod (S2_be_L40)')

plt.plot(df['omega'], df['f_mod_S1_be_L50'], color='orange',
label='f_mod (S1_be_L50)')
plt.plot(df['omega'], df['f_mod_S2_be_L50'], color='saddlebrown',
label='f_mod (S2_be_L50)')


#Colocamos una rejilla de fondo
plt.grid(True)

#Escribimos la leyenda
plt.legend(loc='center right', fontsize=14, bbox_to_anchor=(1.35, 0.5))

#Colocamos título y nombre a los ejes
plt.xlabel('Omega [rad/s]', fontsize=15)
plt.ylabel('Modulation frequency [Hz]', fontsize=15)
plt.tick_params(labelsize=15)

#Imprimimos la gráfica en un formato de archivo a elegir
```

```
plt.savefig('Speed_1.png', bbox_inches='tight')

#Mostramos la gráfica por terminal
plt.show()

#-------------------------------------------------------------------------------

import pandas as pd
import matplotlib.pyplot as plt

df = pd.read_csv("Speed_measurements.csv")

s1 = abs(df['f_mod_S1_be_L10'] - df['f_mod_S2_be_L10'])
s2 = abs(df['f_mod_S1_be_L20'] - df['f_mod_S2_be_L20'])
s3 = abs(df['f_mod_S1_be_L30'] - df['f_mod_S2_be_L30'])
s4 = abs(df['f_mod_S1_be_L40'] - df['f_mod_S2_be_L40'])
s5 = abs(df['f_mod_S1_be_L50'] - df['f_mod_S2_be_L50'])

plt.figure()

plt.plot(df['omega'], s1, color='red',
label='|S1_f_mod-S2_f_mod| (be_L10)')
plt.plot(df['omega'], s2, color='blue',
label='|S1_f_mod-S2_f_mod| (be_L20)')
plt.plot(df['omega'], s3, color='green',
label='|S1_f_mod-S2_f_mod| (be_L30)')
plt.plot(df['omega'], s4, color='purple',
label='|S1_f_mod-S2_f_mod| (be_L40)')
plt.plot(df['omega'], s5, color='orange',
label='|S1_f_mod-S2_f_mod| (be_L50)')

#Colocamos una rejilla de fondo
plt.grid(True)

#Escribimos la leyenda
plt.legend(loc='center right', fontsize=14, bbox_to_anchor=(1.84, 0.5))

#Colocamos título y nombre a los ejes
plt.xlabel('Omega [rad/s]', fontsize=15)
plt.ylabel('Frequency [Hz]', fontsize=15)
plt.tick_params(labelsize=15)

#Imprimimos la gráfica en un formato de archivo a elegir
plt.savefig('Speed_2.png', bbox_inches='tight')
```

```
#Mostramos la gráfica por terminal
plt.show()


#-------------------------------------------------------------------------------

import pandas as pd
import matplotlib.pyplot as plt

df = pd.read_csv("Speed_measurements.csv")


plt.figure(figsize=(10,8))

plt.plot(df['omega'], df['f_mod_S1_nobe_L10'], color='red',
label='f_mod (S1_nobe_L10)')
plt.plot(df['omega'], df['f_mod_S2_nobe_L10'], color='darkred',
label='f_mod (S2_nobe_L10)')

plt.plot(df['omega'], df['f_mod_S1_nobe_L20'], color='blue',
label='f_mod (S1_nobe_L20)')
plt.plot(df['omega'], df['f_mod_S2_nobe_L20'], color='dodgerblue',
label='f_mod (S2_nobe_L20)')

plt.plot(df['omega'], df['f_mod_S1_nobe_L30'], color='green',
label='f_mod (S1_nobe_L30)')
plt.plot(df['omega'], df['f_mod_S2_nobe_L30'], color='lime',
label='f_mod (S2_nobe_L30)')

plt.plot(df['omega'], df['f_mod_S1_nobe_L40'], color='purple',
label='f_mod (S1_nobe_L40)')
plt.plot(df['omega'], df['f_mod_S2_nobe_L40'], color='fuchsia',
label='f_mod (S2_nobe_L40)')

plt.plot(df['omega'], df['f_mod_S1_nobe_L50'], color='orange',
label='f_mod (S1_nobe_L50)')
plt.plot(df['omega'], df['f_mod_S2_nobe_L50'], color='saddlebrown',
label='f_mod (S2_nobe_L50)')


#Colocamos una rejilla de fondo
plt.grid(True)

#Escribimos la leyenda
plt.legend(loc='center right', fontsize=14, bbox_to_anchor=(1.4, 0.5))
```

```
#Colocamos título y nombre a los ejes
plt.xlabel('Omega [rad/s]', fontsize=15)
plt.ylabel('Modulation frequency [Hz]', fontsize=15)
plt.tick_params(labelsize=15)

#Imprimimos la gráfica en un formato de archivo a elegir
plt.savefig('Speed_3.png', bbox_inches='tight')

#Mostramos la gráfica por terminal
plt.show()

#-------------------------------------------------------------------------------

import pandas as pd
import matplotlib.pyplot as plt

df = pd.read_csv("Speed_measurements.csv")

s1 = abs(df['f_mod_S1_nobe_L10'] - df['f_mod_S2_nobe_L10'])
s2 = abs(df['f_mod_S1_nobe_L20'] - df['f_mod_S2_nobe_L20'])
s3 = abs(df['f_mod_S1_nobe_L30'] - df['f_mod_S2_nobe_L30'])
s4 = abs(df['f_mod_S1_nobe_L40'] - df['f_mod_S2_nobe_L40'])
s5 = abs(df['f_mod_S1_nobe_L50'] - df['f_mod_S2_nobe_L50'])

plt.figure()

plt.plot(df['omega'], s1, color='red',
label='|S1_f_mod-S2_f_mod| (nobe_L10)')
plt.plot(df['omega'], s2, color='blue',
label='|S1_f_mod-S2_f_mod| (nobe_L20)')
plt.plot(df['omega'], s3, color='green',
label='|S1_f_mod-S2_f_mod| (nobe_L30)')
plt.plot(df['omega'], s4, color='purple',
label='|S1_f_mod-S2_f_mod| (nobe_L40)')
plt.plot(df['omega'], s5, color='orange',
label='|S1_f_mod-S2_f_mod| (nobe_L50)')

#Colocamos una rejilla de fondo
plt.grid(True)

#Escribimos la leyenda
plt.legend(loc='center right', fontsize=14, bbox_to_anchor=(1.90, 0.5))

#Colocamos título y nombre a los ejes
```

```
plt.xlabel('Omega [rad/s]', fontsize=15)
plt.ylabel('Frequency [Hz]', fontsize=15)
plt.tick_params(labelsize=15)

#Imprimimos la gráfica en un formato de archivo a elegir
plt.savefig('Speed_4.png', bbox_inches='tight')

#Mostramos la gráfica por terminal
plt.show()
```

SNR between surfaces

```
import pandas as pd
import matplotlib.pyplot as plt

df = pd.read_csv("SNR_measurements.csv")

plt.figure(figsize=(10,8))

plt.plot(df['omega'], df['Power(S1_be_L10)'], color='red',
label='SNR (S1_be_L10)')
plt.plot(df['omega'], df['Power(S2_be_L10)'], color='darkred',
label='SNR (S2_be_L10)')

plt.plot(df['omega'], df['Power(S1_be_L20)'], color='blue',
label='SNR (S1_be_L20)')
plt.plot(df['omega'], df['Power(S2_be_L20)'], color='dodgerblue',
label='SNR (S2_be_L20)')

plt.plot(df['omega'], df['Power(S1_be_L30)'], color='green',
label='SNR (S1_be_L30)')
plt.plot(df['omega'], df['Power(S2_be_L30)'], color='lime',
label='SNR (S2_be_L30)')

plt.plot(df['omega'], df['Power(S1_be_L40)'], color='purple',
label='SNR (S1_be_L40)')
plt.plot(df['omega'], df['Power(S2_be_L40)'], color='fuchsia',
label='SNR (S2_be_L40)')

plt.plot(df['omega'], df['Power(S1_be_L50)'], color='orange',
label='SNR (S1_be_L50)')
plt.plot(df['omega'], df['Power(S2_be_L50)'], color='saddlebrown',
label='SNR (S2_be_L50)')
```

```
#Colocamos una rejilla de fondo
plt.grid(True)

#Escribimos la leyenda
plt.legend(loc='center right', fontsize=14, bbox_to_anchor=(1.33, 0.5))

#Colocamos título y nombre a los ejes
plt.xlabel('Omega [rad/s]', fontsize=15)
plt.ylabel('SNR [dB]', fontsize=15)
plt.tick_params(labelsize=15)

#Imprimimos la gráfica en un formato de archivo a elegir
plt.savefig('SNR_1.png', bbox_inches='tight')

#Mostramos la gráfica por terminal
plt.show()

#-------------------------------------------------------------------------

import pandas as pd
import matplotlib.pyplot as plt

df = pd.read_csv("SNR_measurements.csv")

plt.figure(figsize=(10,8))

plt.plot(df['omega'], df['Power(S1_nobe_L10)'], color='red',
label='SNR (S1_nobe_L10)')
plt.plot(df['omega'], df['Power(S2_nobe_L10)'], color='darkred',
label='SNR (S2_nobe_L10)')

plt.plot(df['omega'], df['Power(S1_nobe_L20)'], color='blue',
label='SNR (S1_nobe_L20)')
plt.plot(df['omega'], df['Power(S2_nobe_L20)'], color='dodgerblue',
label='SNR (S2_nobe_L20)')

plt.plot(df['omega'], df['Power(S1_nobe_L30)'], color='green',
label='SNR (S1_nobe_L30)')
plt.plot(df['omega'], df['Power(S2_nobe_L30)'], color='lime',
label='SNR (S2_nobe_L30)')

plt.plot(df['omega'], df['Power(S1_nobe_L40)'], color='purple',
label='SNR (S1_nobe_L40)')
plt.plot(df['omega'], df['Power(S2_nobe_L40)'], color='fuchsia',
```

```
label='SNR (S2_nobe_L40)')

plt.plot(df['omega'], df['Power(S1_nobe_L50)'], color='orange',
label='SNR (S1_nobe_L50)')
plt.plot(df['omega'], df['Power(S2_nobe_L50)'], color='saddlebrown',
label='SNR (S2_nobe_L50)')

#Colocamos una rejilla de fondo
plt.grid(True)

#Escribimos la leyenda
plt.legend(loc='center right', fontsize=14, bbox_to_anchor=(1.36, 0.5))

#Colocamos título y nombre a los ejes
plt.xlabel('Omega [rad/s]', fontsize=15)
plt.ylabel('SNR [dB]', fontsize=15)
plt.tick_params(labelsize=15)

#Imprimimos la gráfica en un formato de archivo a elegir
plt.savefig('SNR_2.png', bbox_inches='tight')

#Mostramos la gráfica por terminal
plt.show()

#-------------------------------------------------------------------------------

import pandas as pd
import matplotlib.pyplot as plt

df = pd.read_csv("SNR_measurements.csv")

s1 = abs(df['Power(S1_nobe_L10)'] - df['Power(S2_nobe_L10)'])
s2 = abs(df['Power(S1_nobe_L20)'] - df['Power(S2_nobe_L20)'])
s3 = abs(df['Power(S1_nobe_L30)'] - df['Power(S2_nobe_L30)'])
s4 = abs(df['Power(S1_nobe_L40)'] - df['Power(S2_nobe_L40)'])
s5 = abs(df['Power(S1_nobe_L50)'] - df['Power(S2_nobe_L50)'])

plt.figure()

plt.plot(df['omega'], s1, color='red',
label='|S1_nobe_L10-S2_nobe_L10|')
plt.plot(df['omega'], s2, color='blue',
label='|S1_nobe_L20-S2_nobe_L20|')
plt.plot(df['omega'], s3, color='green',
label='|S1_nobe_L30-S2_nobe_L30|')
```

```
plt.plot(df['omega'], s4, color='purple',
label='|S1_nobe_L40-S2_nobe_L40|')
plt.plot(df['omega'], s5, color='orange',
label='|S1_nobe_L50-S2_nobe_L50|')

#Colocamos una rejilla de fondo
plt.grid(True)

#Escribimos la leyenda
plt.legend(loc='center right', fontsize=14, bbox_to_anchor=(1.90, 0.5))

#Colocamos título y nombre a los ejes
plt.xlabel('Omega [rad/s]', fontsize=15)
plt.ylabel('SNR [dB]', fontsize=15)
plt.tick_params(labelsize=15)

#Imprimimos la gráfica en un formato de archivo a elegir
plt.savefig('SNR_3.png', bbox_inches='tight')

#Mostramos la gráfica por terminal
plt.show()
```

Appendix

INSTITUTE OF COMMUNICATION, INFORMATION AND PERCEPTION TECHNOLOGIES

Scuola Superiore Sant'Anna

Assessment report

The student Pablo Lucas has carried out experimental activity on the implementation and characterisation of LIDAR system to measure the angular speed of a rotating object. Besides, a simulative analysis has been carried out in order to confirm the validity of the experimental results. The activity started on March 7th 2018 and will last up to July 26th 2018.
The student demonstrated to be able to work independently, learning quickly how to operate with the laboratory instruments. He showed interest in the topic subject of the research, operating with critical approach and interacting with the laboratory personnel and myself on the experiments outcomes.
The obtained results are valuable and can be exploited as a good basis to further develop the activity.

The overall final score is 30/30.

The activity carried out by the student Pablo Lucas corresponds to 12 CFU.

Pisa, 16/07/2018

Signature

Prof. Antonella Bogoni

TeCIP
Institute of Communication,
Information and Perception Technologies
Scuola Superiore Sant'Anna

Via G. Moruzzi, 1 - 56124 Pisa, Italy
tel. +39 050 54.92.189-191
tecip@sssup.it